

## ABSTRACT

LEON, LIDER STEVEN. Parameter Subset Selection and Subspace Analysis Techniques Applied to a Polydomain Ferroelectric Material Phase-Field Energy Model. (Under the direction of Dr. Ralph Smith).

In this dissertation, we illustrate parameter subset selection and subspace techniques applied to a quantum-informed Ginzburg-Landau-Devonshire theory-based phase-field energy model for mono- and polydomain ferroelectric lead titanate structures. This model may be used for characterizing multi-domain structure evolution and accounting for hysteresis and domain wall interactions, which is necessary for model-based material design.

We consider phenomenological parameters that govern attributes of the Landau polarization energy, electrostrictive energy, and gradient energy behavior. In the case of single domain structures, the model is informed by synthetic data provided by density functional theory (DFT) simulations of material electron densities. We use frequentist statistical analysis techniques to demonstrate high correlation among model parameters, which is a function of the underlying electronic structure. For the polydomain structures, we investigate free energy profiles across  $180^\circ$  and  $90^\circ$  twinned domain walls separating oppositely- and perpendicularly-oriented polarization at the grain level. We obtain information in this case from first-principles investigations in the literature.

We address four fundamental questions pertaining to the parameters in the model: (1) are higher-order Landau energy parameters identifiable or influential in the sense that they uniquely contribute to energy responses, (2) how much does strong parameter correlation influence sensitivity analysis results in phase-field models, (3) which electrostrictive coefficients are influential to the polydomain energy response, and (4) which gradient energy parameters are most critical in the  $90^\circ$  domain wall energy? The answers to these questions are important for determining which noninfluential parameters may be fixed at nominal values in subsequent Bayesian inference, uncertainty propagation, and model-based design.

To answer the first two questions, we employ a variance-based methodology for conducting global sensitivity analysis of models with highly correlated parameters and verify our results by comparing Bayesian model calibration for various parameter sets, to conclude that all parameters are influential. In general, the results indicate a significant contribution from higher-order Landau polarization energy terms, due to parameter correlation. To answer questions (3) and (4), we employ recently developed gradient-based active subspace methods, which rely upon the property that model responses vary prominently in only a few directions dictated by linear combinations of the model parameters. We identify all electrostrictive coefficients as influential in the energy response, highlighting the high-order coupling and electromechanical interactions in the polydomain system. Additionally, we determine only one influential gradient energy parameter in the  $90^\circ$  domain wall

energy response. This further supports the dependence of the polydomain energy system on the Landau energy parameters and electrostrictive coefficients. We conclude that the noninfluential gradient energy parameters may be fixed at nominal values in future Bayesian inference investigations. This analysis also provides insight into how parameter subset selection and subspace analysis techniques can be applied to other material system models.

© Copyright 2018 by Lider Steven Leon

All Rights Reserved

Parameter Subset Selection and Subspace Analysis Techniques Applied to a  
Polydomain Ferroelectric Material Phase-Field Energy Model

by  
Lider Steven Leon

A dissertation submitted to the Graduate Faculty of  
North Carolina State University  
in partial fulfillment of the  
requirements for the Degree of  
Doctor of Philosophy

Applied Mathematics

Raleigh, North Carolina

2018

APPROVED BY:

---

Dr. Elizabeth Dickey

---

Dr. Pierre Gremaud

---

Dr. Mansoor Haider

---

Dr. Ralph Smith  
Chair of Advisory Committee

## **DEDICATION**

To Ms. Rocca, my guidance counselor who helped me find the opportunities that allowed me to obtain a college education.

## **BIOGRAPHY**

Lider was born in Pereira, Colombia, a small city located on the foothills of the Andes mountains. He lived in Colombia until he was 8 years old, when he moved to the United States with his family. It was during this time that Lider's passion for working with numbers flourished. He spent his elementary and high school years in Dover, NJ and Roxbury, NJ, and attended college in Montclair State University, majoring in applied mathematics. During his undergraduate training years, Lider was introduced to applied mathematics research, participating in a REU at NC State University.

## ACKNOWLEDGEMENTS

First and foremost, I would like to thank my advisor, Dr. Ralph C. Smith for his help and support during this very strenuous process. Thank you for believing in me from day one and for your unconditional kindness and dedication to my personal and professional success. Thank you also for your patience, your advice, your guidance, your expertise, your resources, and last but not least, for your friendship. To my other committee members, Dr. Elizabeth Dickey, Dr. Pierre Gremaud and Dr. Mansoor Haider, thank you for your instruction, time and expertise devoted to my preliminary exam, PhD defense and thesis dissertation.

Additionally, I would like to thank Dr. William Oates and Dr. Paul Miles for their most valuable feedback into my research, and for providing the models and DFT data, that became essential parts of my research. I would also like to thank my undergraduate research advisor Dr. Eric Forgoston for introducing me to the wonderful world of applied mathematics research, and for the investigations that helped lay the foundations for my professional career.

I owe a big part of this achievement to Mr. Bob Howitt for taking me as one of the Project 2050 scholars in the WKBJ Foundation. I am truly grateful for your support and belief in me ever since we met back in 2008. Thank you for your friendship, kindness and all those fantastic talks we've had over the years.

Thank you to my dear parents for instilling in me from a young age the value of getting an education, as well as for their love, encouragement and support at every stage of my life. Thank you for the core values and teachings that have shaped me into the person I am today. None of this would have ever come true if it wasn't for you. To my brother, thank you for the great times spent together, and for being the awesome brother you are.

I'd also like to extend my gratitude to my parents-in-law for their love and encouragement throughout my graduate career. You are always there for me and I thank you from the bottom of my heart.

Finally, thank you to my fantastic wife and soul mate. Words can't begin to describe how instrumental you've been in helping me achieve this milestone. Without you by my side, crying, laughing, listening and loving me in good and bad times, none of this would have ever been possible. Thank you my dearest love.

This research is based upon work supported by the National Science Foundation under Grant No. DGE-1633587. It is additionally supported in part by the NSF Grant CMMI-1306290 Collaborative Research CDS&E.

## TABLE OF CONTENTS

<b>LIST OF TABLES</b> .....	<b>vii</b>
<b>LIST OF FIGURES</b> .....	<b>ix</b>
<b>Chapter 1 INTRODUCTION</b> .....	<b>1</b>
1.1 Identifiable and Influential Parameters .....	4
1.2 Local and Global Sensitivity .....	5
1.3 Active Subspace Methods .....	6
<b>Chapter 2 FERROELECTRIC MATERIALS</b> .....	<b>8</b>
2.1 Monodomain Structures .....	11
2.2 Polydomain Structures .....	11
2.3 Ferroelectric Phase-Field Model .....	13
2.4 Density Functional Theory Calculations .....	17
<b>Chapter 3 PARAMETER SUBSET SELECTION and UNCERTAINTY QUANTIFICATION</b> ...	<b>19</b>
3.1 Global Sensitivity Analysis for Uncorrelated Inputs .....	21
3.1.1 Morris Screening .....	21
3.1.2 Variance-Based Sensitivity Analysis .....	22
3.2 Global Sensitivity Analysis for Correlated Inputs .....	26
3.2.1 Variance-Based Sensitivity Analysis .....	28
3.2.2 Linearly Parameterized Problems .....	30
3.2.3 Numerical Basis Functions Expansion .....	32
3.3 Subset Selection using the Singular Value Decomposition .....	34
3.3.1 SVD Subset Selection for Linearly Parameterized Models .....	35
3.3.2 Fisher Information Matrix Analysis .....	35
3.3.3 Random Sampling of the Sensitivity Matrix .....	37
3.4 Active Subspace Selection .....	38
3.4.1 Normalized Gradient Evaluations .....	38
3.4.2 Active Subspace Construction .....	41
3.4.3 Finding the Dimension of the Active Subspace .....	43
3.4.4 Activity Scores .....	44
3.5 Bayesian Inference .....	46
3.5.1 Markov Chain Monte Carlo (MCMC) .....	46
3.5.2 Delayed Rejection Adaptive Metropolis (DRAM) .....	47
3.5.3 Model Calibration .....	47
3.6 Uncertainty Propagation .....	48
3.6.1 Sampling .....	48
3.6.2 Energy Statistics .....	49
<b>Chapter 4 MONODOMAIN ENERGY ANALYSIS</b> .....	<b>50</b>
4.1 Monodomain Continuum Model .....	52
4.2 Global Sensitivity Analysis .....	55



4.2.1	Sensitivity Analysis for Uncorrelated Parameters . . . . .	56
4.3	Bayesian Statistical Analysis . . . . .	59
4.4	Sensitivity Analysis for Correlated Parameters . . . . .	62
4.5	Analysis Using the Fisher Information Matrix . . . . .	66
<b>Chapter 5</b>	<b>POLYDOMAIN ENERGY MODELS . . . . .</b>	<b>71</b>
5.1	Stored Energy Relations . . . . .	72
5.2	Monodomain Energy Regions . . . . .	74
5.3	Total Domain Wall Energies . . . . .	75
5.4	Parameters and Distributions . . . . .	76
<b>Chapter 6</b>	<b>180° POLYDOMAIN STRUCTURE ANALYSIS . . . . .</b>	<b>77</b>
6.1	180° Domain Wall Energy Model . . . . .	77
6.1.1	Model Solution Procedure . . . . .	79
6.1.2	Implementation . . . . .	81
6.2	Bayesian Inference . . . . .	82
6.3	Parameter Subset Selection . . . . .	83
6.4	Active Subspace Construction . . . . .	84
6.5	Uncertainty Propagation . . . . .	87
<b>Chapter 7</b>	<b>90° POLYDOMAIN STRUCTURE ANALYSIS . . . . .</b>	<b>91</b>
7.1	90° Domain Wall Energy . . . . .	91
7.1.1	Model Solution Procedure . . . . .	95
7.1.2	Implementation . . . . .	96
7.2	Parameter Subset Selection . . . . .	97
7.3	Bayesian Inference . . . . .	100
7.4	Active Subspace Construction . . . . .	101
7.5	Uncertainty Propagation . . . . .	103
<b>Chapter 8</b>	<b>CONCLUSIONS . . . . .</b>	<b>108</b>
	<b>BIBLIOGRAPHY . . . . .</b>	<b>111</b>
	<b>APPENDIX . . . . .</b>	<b>116</b>
Appendix A	Delayed Rejection Adaptive Metropolis Algorithm . . . . .	117

## LIST OF TABLES

Table 4.1	Elastic coefficients obtained from [24]. . . . .	51
Table 4.2	Nominal values for the polarization parameters $\theta_p$ and the stress component parameters $\theta_\sigma$ , defined in (4.9) and (4.10), respectively. The nominal values were obtained from a least-squares optimization of the outputs (4.12). . . . .	54
Table 4.3	Sobol' sensitivity indices $S_i$ , $S_{T_i}$ , Morris screening measures $\mu_i^*$ , $\sigma_i^*$ and Pearson correlation coefficients $\rho_{all}$ , $\rho_{inf}$ for the Landau energy phenomenological parameters $\theta_p$ (4.9). Note that $\rho_{inf}$ indicates Pearson correlation coefficients when only presumed influential parameters are sampled while all others are fixed. The shaded cells correspond to significant indices, measures and coefficients. . . . .	59
Table 4.4	Sensitivity indices for total contributions $S_{r_n}$ constructed using the component functions $f_{r_n}$ for the Landau energy parameters $\theta_p$ . The A's and N's represent sensitivity indices derived from the analytical and numerical determination of the component functions, respectively. The indices correspond to the order specified by $\theta_p = [\alpha_1, \alpha_{11}, \alpha_{12}, \alpha_{111}, \alpha_{112}]$ . The shaded cells designate significant indices. . . . .	67
Table 4.5	Sensitivity indices for total contributions $S_{r_n}$ constructed using the component functions $f_{r_n}$ for the normal stress parameters $\theta_{\sigma_{ns}}$ . The indices correspond to the order specified by $\theta_{\sigma_{ns}} = [q_{11}, q_{12}, \sigma_{11}^R, \sigma_{22}^R, \sigma_{33}^R]$ . The shaded cells correspond to significant indices. . . . .	68
Table 4.6	Sensitivity indices for total contributions $S_{r_n}$ constructed using the component functions $f_{r_n}$ for the shear stress parameters $\theta_{\sigma_s}$ . The indices correspond to the order specified by $\theta_{\sigma_s} = [q_{44}, \sigma_{23}^R]$ . . . . .	68
Table 4.7	Results from Algorithm 3.3.2, to determine unidentifiable parameters in $\theta_p$ (4.9) for the polarization energy $u_p$ (4.3). . . . .	69
Table 4.8	Results from Algorithm 3.2 to determine unidentifiable parameters in $\theta_\sigma$ (4.10) for the normal and shear stress components $\sigma_{ns}$ and $\sigma_s$ (4.8). . . . .	70
Table 6.1	List of parameters used in solution and evaluation of the domain wall energy (6.5), along with corresponding units. The parameters $\theta_{180}^{MD}$ are appropriately scaled from Table 4.2 to reflect the new unit system employed here. . . . .	81
Table 6.2	Units of measurement used in the 180° domain wall model for energy, length, charge, and voltage . . . . .	82
Table 6.3	Results from Algorithm 3.3.2 with the global sensitivity matrix (3.44) to determine noninfluential parameters in $\theta_{180}$ (6.6) for the 180° domain wall energy $E_{180^\circ}$ (6.5). . . . .	84
Table 6.4	Mean relative errors (MRE) for response surfaces considering 1-, 2-, and 3-dimensional active subspaces for the mode response $E_{180^\circ}$ . . . . .	85
Table 6.5	Energy test statistic and critical values for $\alpha = 0.05$ , $\alpha = 0.10$ with respect to normally distributed $\theta_{180}$ (normal) and sampled from the chains in the single domain (MD) analysis of [33]. . . . .	90

Table 7.1	Nominal values for parameters $\theta_{90}$ with respect to the domain wall model energy model $E_{90^\circ}(\theta_{90})$ . . . . .	97
Table 7.2	Results from Algorithm 3.3.2 with the global sensitivity matrix (3.44) to determine noninfluential parameters in $\theta_{90}$ (7.19) for the $90^\circ$ domain wall energy $E_{90^\circ}$ (7.18). . . . .	99
Table 7.3	Mean relative errors (MRE) for response surfaces considering 1-, 2-, 3-, and 4-dimensional active subspaces for the model response $E_{90^\circ}$ . . . . .	102
Table 7.4	Energy test statistic and critical values for $\alpha = 0.05$ , $\alpha = 0.10$ , when sampling the Landau and electrostrictive parameters from a normal distribution (normal) and directly from the monodomain chains (MD) [33]. . . . .	107

## LIST OF FIGURES

Figure 1.1	Schematic of the steps in uncertainty quantification, most associated with this dissertation. This is a partial diagram of the complete schematic given in [51]. . . . .	3
Figure 1.2	Illustration of $y = f(\theta)$ for (a) identifiable, (b) unidentifiable, and (c) noninfluential parameters $\theta$ . Plotted after [27]. . . . .	4
Figure 1.3	Illustration of (a) a highly influential parameter $\theta_1$ and (b) minimally influential parameter $\theta_2$ . (c) Minimally influential parameter $\theta_3$ having large local derivative values. Plotted after [27]. . . . .	5
Figure 2.1	(a) Dependence of the Curie temperature $T_C$ on the molar fraction $x$ of $\text{PbZrO}_3$ , and morphotropic phase boundary separating rhombohedral from tetragonal structures. (b) Dependence of the piezoelectric coupling coefficient on the molar fraction $x$ . Plotted after [22]. . . . .	9
Figure 2.2	Schematic of ferroelectric material grains depicting $180^\circ$ and $90^\circ$ domains and domain walls. Polarization is randomly oriented in the grains. Plotted after [52]. . . . .	10
Figure 2.3	Atomic structure unit cell of lead titanate ( $\text{PbTiO}_3$ ), with polarization oriented in the $x_3$ direction. (a) Cubic form of $\text{PbTiO}_3$ in the paraelectric phase $T > T_C$ . (b) Tetragonal structure of $\text{PbTiO}_3$ , along with spontaneous polarization $P_0$ in the $x_3$ direction. (c) $\text{PbTiO}_3$ internal energy as a function of the Ti position in the paraelectric phase $T > T_C$ , and (d) in the ferroelectric phase $T < T_C$ . . . . .	12
Figure 2.4	Hysteretic field-polarization relation produced by ferroelectric switching mechanisms, when applied electric fields are larger than $E_C$ in magnitude. The remanence polarization $P_R$ occurs when the applied electric field is zero, where the linear and reversible direct and converse piezoelectric effects are applicable. . . . .	13
Figure 2.5	(a) Ferroelectric phase for $\text{PbTiO}_3$ , with polarization oriented in the $x_3$ direction. (b) Single domain structure for $\text{PbTiO}_3$ . . . . .	14
Figure 2.6	(a) $180^\circ$ and (b) $90^\circ$ polydomain structures of polarization orientation. Domains are separated by corresponding domain walls or boundaries. We depict a new coordinate system for the $90^\circ$ polydomain structure. As detailed in Section 2.2, this new $45^\circ$ -rotated coordinate system is denoted by $(s, r, x_3)$ , with the domain wall positioned at $s = 0$ . . . . .	14
Figure 2.7	Polarization states at which DFT energy and stresses were calculated in the computational study of [33]. . . . .	18
Figure 4.1	Input polarization values of $P_2$ and $P_3$ obtained from the DFT analysis implemented in [33], and employed in the Landau polarization energy (4.3). . . . .	53
Figure 4.2	Scatterplots, Pearson correlations $\rho$ given by (3.7), means, and two standard deviation intervals for the polarization parameters $\theta_p$ and response $Y_p$ given (4.13). . . . .	57

Figure 4.3	Pearson correlations of sampled (a) $\alpha_1$ , (b) $\alpha_{11}$ against each of 500 realizations of $Y_p$ (4.13), with all other parameters in $\theta_p$ also sampled and only $\alpha_1$ , $\alpha_{11}$ sampled. Pearson correlation coefficients $\rho$ for each parameter are also presented. The labels (—) and (- - -) denote the means and two standard deviations for the cases where all parameters $\theta_p$ are sampled to obtain the responses shown by (o), and only parameters $\alpha_1$ , $\alpha_{11}$ are sampled to obtain the responses shown by (+). . . . .	58
Figure 4.4	Chain of accepted sampled Landau energy parameter values with respect to DFT simulations in [33], obtained using $1 \times 10^4$ iterations. . . . .	60
Figure 4.5	Pairwise correlation among the Landau energy parameters (4.9). Strong correlation observed between the lower- and higher-order parameters. . . . .	61
Figure 4.6	Posterior densities obtained via Bayesian calibration of $Y_p(\theta_p)$ in when (i) sampling all the parameters, (ii) sampling $\alpha_1, \alpha_{11}, \alpha_{111}$ with $\alpha_{12}, \alpha_{112}$ fixed, and (iii) sampling $\alpha_1, \alpha_{11}$ with $\alpha_{111}, \alpha_{12}, \alpha_{112}$ fixed. . . . .	62
Figure 4.7	(a) First, (b) second, (c) third, (d) fourth and (e) fifth-order component functions constructed using the analytical method (- -) and the numerical method (—) for $\theta_p$ in (4.13) with $m = 4$ subintervals for the Cubic B spline basis functions. . . . .	64
Figure 4.8	(a) First, (b) second, (c) third, (d) fourth and (e) fifth order component functions constructed using the analytical method (- -) and numerical method (—) for $\theta_{\sigma_{ns}}$ in (4.14) with $m = 4$ subintervals. . . . .	65
Figure 4.9	First-order component functions constructed using the analytical method (- -) and numerical method (—) for $\theta_{\sigma_s}$ in (4.15) with $m = 4$ subintervals. . . . .	65
Figure 4.10	Comparison of analytical and numerical methods obtain (a) first-order and (b) total sensitivity indices for (4.13). . . . .	67
Figure 4.11	Comparison of analytical and numerical methods to obtain (a) first-order and (b) total sensitivity indices for (4.14). . . . .	69
Figure 4.12	Comparison of analytical and numerical methods to obtain (a) first-order and (b) total sensitivity indices for (4.15). . . . .	69
Figure 6.1	Comparison of analytic, finite difference and MATLAB bvp4c .m solver for solution $180^\circ$ domain wall energy system. From top left to bottom right, $180^\circ$ domain wall energy density solution, polarization $P_3$ in the $x_1$ direction, strain $\varepsilon_{11}$ in the $x_1$ direction, and polarization gradient in the $x_1$ direction as we cross the $180^\circ$ domain wall. . . . .	82
Figure 6.2	(a) Chain of accepted values and (b) kernel density estimation (kde) for the parameter $g_{44}$ obtained from the Bayesian uncertainty analysis with respect to $E_{180^\circ}$ . . . . .	83
Figure 6.3	Singular values obtained from the active subspace determination for $E_{180^\circ}$ assuming uniform (3.47) and normal (3.49) distributions for parameters $\theta_{180^\circ}$ . The shading indicates two standard deviations from the sample mean. . . . .	85
Figure 6.4	Response surfaces for $E_{180^\circ}$ constructed based on a (a) one-dimensional and (b) two-dimensional active subspace. . . . .	86

Figure 6.5	Activity scores for the model response $E_{180^\circ}$ assuming uniform (3.47) and normal (3.49) parameter distributions, and a (a) one-dimensional and (b) two-dimensional active subspace. . . . .	86
Figure 6.6	Uncertainty propagation of the (a) $\theta_{180}$ model inputs and (b) $\theta_{180}^{sens}$ influential inputs on the energy density $u_{180}(x_1) - u_0$ . . . . .	88
Figure 6.7	(a) Peak residuals obtained for the different credible intervals (CI) peaks of Figure 6.6(a) subtracted by the peaks of Figure 6.6(b). (b) 50% CI peak residuals obtained from the 50% CI peaks of Figure 6.6(a) subtracted by the peaks of Figure 6.6(b). . . . .	88
Figure 6.8	(a) Histogram and (b) probability density of the $180^\circ$ domain wall energy $u_{180}(0) - u_0$ distributions with respect to the case where the uncertainties of all parameters $\theta_{180}$ are propagated, as compared with the case where only the uncertainties of parameters $\theta_{180}^{sens}$ are propagated. In (c) and (d) parameters were sampled directly from the chains in the monodomain analysis of Section 4.3 and [33], and the uncertainty analysis of Section 6.2. . . . .	89
Figure 6.9	Energy test statistic replicates for the analysis of the $u_{180}(0) - u_0$ distribution considering a (a) normal distribution and (b) direct sampling from the monodomain chains of [33] for the Landau and electrostrictive parameters in $\theta_{180}$ . . . . .	90
Figure 7.1	Comparison of finite difference <code>fsolve.m</code> and <code>bvp4c.m</code> MATLAB solvers for solution of the $90^\circ$ domain wall energy system. From top left to bottom right, $90^\circ$ domain wall energy density solution, polarization $P_s$ in the $s$ direction, polarization $P_r$ in the $s$ direction, and polarization gradients $P_{s,s}$ and $P_{r,s}$ in the $s$ direction as we cross the $90^\circ$ domain wall. . . . .	98
Figure 7.2	(a) Chain and (b) kernel density estimation for the parameter $g_{11}$ , obtained from the implementation of the DRAM algorithm [18]. . . . .	100
Figure 7.3	Singular values obtained from the active subspace determination for $E_{90^\circ}$ assuming normal (3.49) and uniform (3.47) distributions for parameters $\theta_{90}$ . The shaded area around the singular values corresponds to two standard deviations. . . . .	101
Figure 7.4	Response surface for $E_{90^\circ}$ constructed based on a (a) one-dimensional and (b) two-dimensional active subspace. . . . .	102
Figure 7.5	Activity scores for the model response $E_{90^\circ}$ assuming normal (3.49) and uniform (3.47) parameter distributions, and a (a) one-dimensional and (b) two-dimensional active subspace. The errorbars indicate two standard deviations from the mean. . . . .	103
Figure 7.6	Uncertainty propagation of the (a) $\theta_{90}$ model inputs and (b) $\theta_{90}^{sens}$ influential inputs on the energy density $u_{90}(s) - u_0$ , assuming a normal distribution for the parameters. In (c) and (d) we sample directly from the monodomain chains in [33] for the Landau and electrostrictive parameters. . . . .	105
Figure 7.7	Peak residuals obtained for the different credible intervals (CI) peaks of Figure 7.6. . . . .	105

Figure 7.8	(a) Histogram and (b) probability density of the $90^\circ$ domain wall energy $u_{90}(0) - u_0$ distributions with respect to the case where the uncertainties of all parameters $\theta_{90}$ are propagated against the case where only the uncertainties of parameters $\theta_{90}^{sens}$ are propagated. In (c) and (d) we sampled directly from the chains obtained in the monodomain analysis reproduced in Chapter 4 and obtained from [33]. . . . .	106
Figure 7.9	Energy test statistic replicates for the statistical analysis of the $u_{90}(0) - u_0$ distribution, with $\theta_{90}$ (a) normally distributed and (b) having Landau energy and electrostrictive parameters sampled from the monodomain chains in [33].	107

## CHAPTER

# 1

# INTRODUCTION

*“If we knew what it was we were doing, it would not be called research, would it?”*

- Albert Einstein

Sensitivity analysis and uncertainty quantification play pivotal roles for scientists and engineers using models to predict physical phenomena with quantified uncertainties. Specifically, sensitivity analysis or parameter subspace analysis comprises a critical first step to isolate subsets or subspaces of parameters that are identifiable in the sense that they are uniquely determined by data as influential on measured responses. Noninfluential or nonidentifiable parameters are fixed at nominal values before subsequent Bayesian inference to quantify input uncertainties and uncertainty propagation to compute intervals for quantities of interest.

The sensitivity analysis and uncertainty quantification framework can be naturally applied to Landau-Ginzburg phase-field energy models used to characterize phase transitions and domain structure evolution in ferroelectric materials. As detailed in Chapter 2, mechanisms such as ferroelectric hysteresis, may be quantified via Landau-Ginzburg theory, providing relations employed in homogenized energy models, to be used for model-based control and material design [50, 52]. A commonly encountered challenge is the estimation of unknown Landau-Ginzburg parameters [5, 32, 56]. Parameter assumptions are, in some cases, made to alleviate the difficulties in obtaining uncertain parameter estimates and solutions to free energy systems [5]. Density functional theory (DFT) simulations can be used to generate atomic-level data to inform continuum energy rela-



tions, as detailed in [33]. However, using quantum calculations to inform a macroscopic continuum domain introduces uncertainty into the model that may have significantly different parameter uncertainties [27]. The techniques described in Chapter 3 are focused on addressing and quantifying this uncertainty.

Specifically, the energy model we consider in this dissertation is composed of classical energy functionals for the mechanical energy, Landau polarization energy, electrostrictive energy and gradient energy. The attributes of these functionals are governed by unknown phenomenological parameters that must be estimated prior to their employment in model-based material design. For example, the sixth-order Landau polarization energy

$$\begin{aligned} u_P(\mathbf{P}) = & \alpha_1(P_1^2 + P_2^2 + P_3^2) + \alpha_{11}(P_1^2 + P_2^2 + P_3^2)^2 + \alpha_{12}(P_1^2 P_2^2 + P_1^2 P_3^2 + P_2^2 P_3^2) \\ & + \alpha_{111}(P_1^6 + P_2^6 + P_3^6) + \alpha_{112}[P_1^4(P_2^2 + P_3^2) + P_2^4(P_1^2 + P_3^2) + P_3^4(P_1^2 + P_2^2)] \\ & + \alpha_{123}P_1^2 P_2^2 P_3^2 \end{aligned} \quad (1.1)$$

is governed by the phenomenological parameters  $\theta_P = [\alpha_1, \alpha_{11}, \alpha_{12}, \alpha_{111}, \alpha_{112}, \alpha_{123}]$ , specifying the non-convex energy potential as a function of the polarization  $\mathbf{P} = [P_1, P_2, P_3]$ .

To facilitate the employment of phase-field models in material design, we focus on two major issues pertaining to these parameters. First, we determine which of the parameters are identifiable or influential in the sense that they uniquely contribute to energy responses. Secondly, we determine the actual parameter values that dictate specific material behavior and the associated uncertainties in these values. Both of these issues are addressed in Chapter 4 for single domain energy responses, and in Chapters 6-7 for polydomain energy responses.

For the Landau polarization relation (1.1), we employ sensitivity analysis to determine whether the sixth-order model is necessary to approximate quantum calculations or whether a fourth-order model will suffice. In classical global sensitivity analysis methods, parameters are assumed to be uniformly and independently distributed in the absence of *a priori* knowledge of the underlying parameter distribution. This assumption is made to avoid introducing unintentional biases. However, we show that Landau parameters are strongly correlated and determine how the correlation influences sensitivity analysis results.

Domain walls have long been evidenced to produce attractive properties of ferroelectric materials, such as high piezoelectric and dielectric constants [5, 32, 57]. The parameters most associated with electromechanical effects of polarization and strain in the Landau-Ginzburg energy are the coefficients  $q_{11}$ ,  $q_{12}$  and  $q_{44}$  governing the electrostrictive energy

$$\begin{aligned} u_C = & -q_{11}(\varepsilon_{11}P_1^2 + \varepsilon_{22}P_2^2 + \varepsilon_{33}P_3^2) \\ & -q_{12}[\varepsilon_{11}(P_2^2 + P_3^2) + \varepsilon_{22}(P_1^2 + P_3^2) + \varepsilon_{33}(P_1^2 + P_2^2)] \\ & -q_{44}(\varepsilon_{12}P_1P_2 + \varepsilon_{13}P_1P_3 + \varepsilon_{23}P_2P_3). \end{aligned} \quad (1.2)$$

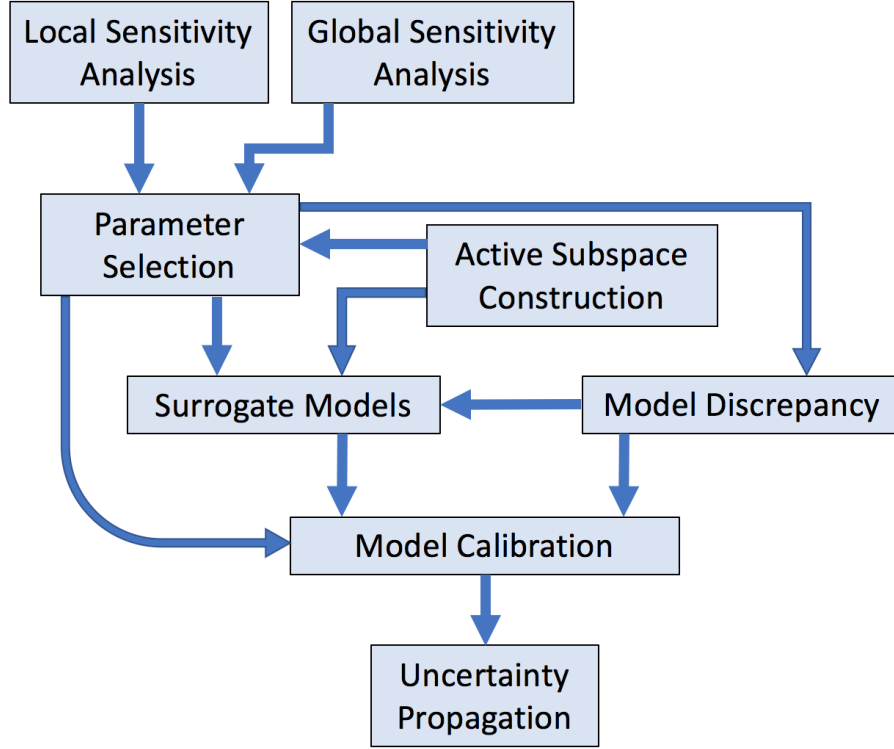


**Figure 1.1** Schematic of the steps in uncertainty quantification, most associated with this dissertation. This is a partial diagram of the complete schematic given in [51].

When transitioning through the  $180^\circ$  and  $90^\circ$  domain walls, polarization and strain evolution are further dependent on high-order coupling between the electrostrictive coefficients and the Landau energy parameters in (1.2), as well on polarization gradient exchange parameters as detailed in Chapters 2, 5, 6 and 7. Consequently, we determine which parameters are noninfluential with respect to the polydomain energy response, to be fixed for subsequent Bayesian inference and uncertainty propagation. We provide a more detailed introduction to ferroelectric materials and phase-field energy models in Chapter 2.

We illustrate in Figure 1.1 the steps in the uncertainty quantification framework, which are most associated with this dissertation. In Section 1.2, we provide an introduction to local and global sensitivity analysis used for parameter subset selection. This is followed by active subspace methods, which we introduce in Section 1.3. Before addressing local and global sensitivity, in the next section we define identifiable and influential parameter spaces and introduce terminology, which we use throughout this dissertation.

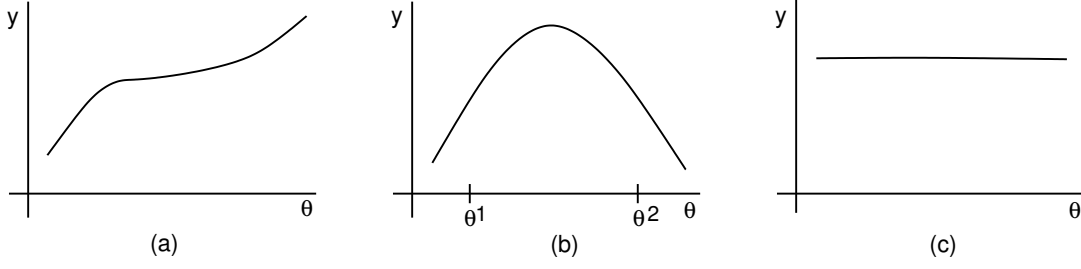


**Figure 1.2** Illustration of  $y = f(\theta)$  for (a) identifiable, (b) unidentifiable, and (c) noninfluential parameters  $\theta$ . Plotted after [27].

## 1.1 Identifiable and Influential Parameters

We first define identifiable and influential parameters. We will use this terminology throughout this dissertation to describe parameters that do not significantly influence model responses.

Consider the general input-output relation

$$Y = f(\Theta),$$

where  $\Theta = [\Theta_1, \dots, \Theta_p]$  are random variables representing inputs, or parameters, and  $\theta = [\theta_1, \dots, \theta_p]$  are realizations of those random variables. Here  $Y$  and  $y$  are also corresponding random variables and realizations for the responses. For example, in the polarization energy (1.1),  $\Theta = \Theta_p$  are the phenomenological parameters,  $f$  denotes the sixth-order relation, and  $y = u_p(\mathbf{P})$  denotes the energy for a specified polarization value.

The concept of identifiability is defined as follows. Parameters  $\theta = [\theta_1, \dots, \theta_p]$  are identifiable at  $\theta^*$  if  $f(\theta) = f(\theta^*)$  implies that  $\theta = \theta^*$  for realizations  $\theta$  in an admissible parameter space  $\mathbb{Q}$ . We denote  $I(\theta)$  as the identifiable subspace. The parameters  $\theta$  are identifiable with respect to this space, if it holds for all  $\theta^* \in I(\theta)$ . The unidentifiable subspace  $NI(\theta)$  is the orthogonal complement of  $I(\theta)$ , with respect to the Euclidean inner product. Unidentifiable parameters must be fixed at nominal values for model calibration using outputs  $y$ , whereas the identifiable parameters may be uniquely determined from observations. We illustrate an example of identifiable and unidentifiable parameters in Figure 1.2(a) and (b), respectively.

In the same context, we define parameters  $\theta$  to be noninfluential on the space  $\mathcal{N}\mathcal{I}(\theta)$  if  $|f(\theta) - f(\theta^*)| < \varepsilon$  for all  $\theta$  and  $\theta^* \in \mathcal{N}\mathcal{I}(\theta)$ . Likewise,  $\mathcal{I}(\theta)$  is the influential parameter space and orthogonal complement of  $\mathcal{N}\mathcal{I}(\theta)$ , in the admissible parameter space  $\mathbb{Q}$ . Similar to unidentifiable parameters, noninfluential parameters can be fixed for subsequent model calibration and uncertainty propagation. We illustrate an example of a noninfluential parameter in Figure 1.2(c).

When considered over the admissible parameter space, a parameter  $\theta_1$  is more influential than

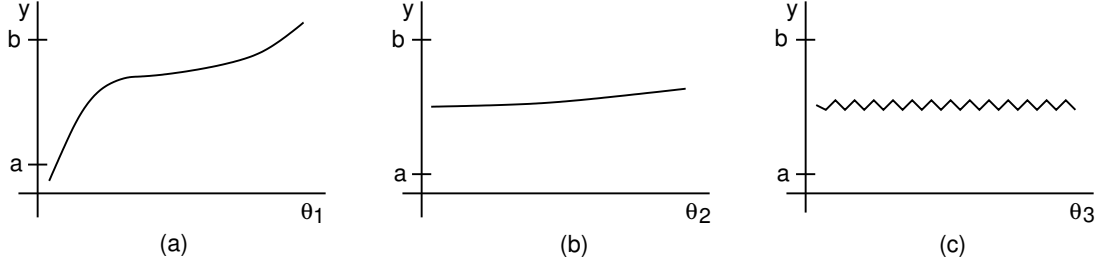


**Figure 1.3** Illustration of (a) a highly influential parameter  $\theta_1$  and (b) minimally influential parameter  $\theta_2$ . (c) Minimally influential parameter  $\theta_3$  having large local derivative values. Plotted after [27].

$\theta_2$  if perturbations in  $\theta_1$  produce greater variability in  $y$  than perturbations in  $\theta_2$ . We illustrate highly and minimally influential parameters in Figure 1.3(a) and (b).

## 1.2 Local and Global Sensitivity

Through the use of parameter subset selection techniques, such as local and global sensitivity analysis, we determine which parameters are most influential in a model. We can then use this information to fix those parameters, which do not significantly influence the model, in the sense that their perturbations are only minimally reflected in the model response.

Local sensitivity analysis concerns the change in a model output or response with respect to local changes in nominal parameter values. A measure of local sensitivity is obtained by evaluating the partial derivatives

$$\frac{\partial f}{\partial \theta}(\theta^*). \quad (1.3)$$

The limitations in using local sensitivity analysis to determine a parameter subset suitable for uncertainty quantification are that we do not broadly account for uncertainties and parameter interactions across the entire parameter space. For example, as illustrated in Figure 1.3(c), the parameter  $\theta_3$  is noninfluential when considered throughout the admissible parameter space, but has large derivatives locally at certain nominal values. Morris screening (defined in Section 3.1) partially addresses this issue by statistically averaging derivative approximations at multiple nominal values [35].

This motivates global sensitivity analysis, in the sense that the uncertainties in the model response are more broadly apportioned to the uncertainties in the model inputs. Rather than studying the sensitivity of the model  $y = f(\theta)$ , to local perturbations about  $\theta^*$ , we consider associated distributions for the parameters  $\theta$ . Additionally, global sensitivity analysis considers sensitivities due to different combinations of parameter samples rather than traditional one-factor-at-a-time local sensitivity analysis methods.

In Chapter 3, we introduce several global sensitivity analysis methods used in our investigation. This includes variance-based global sensitivity analysis, based on [46, 53], as well as the approximated gradient-based methods of [35]. We compare and contrast the methods and provide an alternative approach for performing variance-based global sensitivity analysis when model parameters are strongly correlated. This method, based on the theory of [29], is motivated by cases where the assumption of independently and uniformly distributed parameters is violated and hence can yield incorrect sensitivity results.

### 1.3 Active Subspace Methods

In some cases, influential or identifiable parameter spaces can include linear combinations of parameters. In such scenarios, it is useful to consider directions in the admissible parameter space, not aligned with particular coordinate axes, corresponding to individual parameter values. Here we often discover that the function may vary most dominantly, with respect to directions dictated by linear combinations of the parameter values, as detailed in [8]. Typically this includes a small number of directions, and one can project onto this low-dimensional space by employing a linear transformation. This provides us with the capability to use linear algebra properties to determine an influential subspace. As this subspace contains the most influential or “active” directions in the admissible parameter space, we refer to it as the *active subspace*. The active subspace is additionally less susceptible to unknown distributions, facilitating analysis where parameter densities are not known *a priori*.

The active subspace is determined by the construction of a gradient, or approximate gradient, matrix  $\mathbf{G}$ , containing evaluations of the function gradient with respect to random parameter values, and its corresponding singular value decomposition  $\mathbf{G} = \mathbf{W}\Sigma\mathbf{V}^T$ , as proposed in [1, 8, 44]. Alternatively, a QR decomposition may also be used. The projection of the original input parameters  $\theta$  onto the active subspace is obtained by the relation

$$\mathbf{y} = \mathbf{W}_1^T \theta.$$

Here,  $\mathbf{y}$  are the active variables and  $\mathbf{W}_1$  represents the first  $m$  singular vectors, where  $m$  is the dimension of the active subspace. The orthogonal projection  $\mathbf{z} = \mathbf{W}_2^T \theta$  represents the inactive subspace projection, where perturbations in these directions are reflected minimally in the original model response. We provide more details about the construction and dimension selection of the active subspace in Chapter 3.

As illustrated in Figure 1.1, active subspace methods may be used to reduce input dimensions and to develop surrogate models. In the latter, upon the projection of the original input parameters onto the active subspace, one can construct a response surface which approximates the original

model response, as a function of the active variables. This greatly reduces the computational cost, since in many cases, the response surface is constructed from a simple regression analysis, and is a function of only a few active variables.

One can also exploit information from the SVD  $\mathbf{G} = \mathbf{W}^T \Sigma \mathbf{V}^T$ , to construct global sensitivity metrics

$$a_i = \sum_j^m \lambda_j w_{i,j}^2, \quad i = 1, \dots, p$$

Here,  $p$  is the number of model parameters,  $\lambda_j$  denotes the  $j^{th}$  eigenvalue and  $w_{i,j}$  is the  $ij$ -entry of  $\mathbf{W}$  [9]. These metrics are termed *activity scores*, as they rank the “activity” of each of the model parameters in terms of their relative influence on the output. In this dissertation, we use active subspaces to construct activity scores and compare and contrast results with parameter subset selection techniques based on other gradient-based methods. We include the theoretical background for active subspaces in Chapter 3, and illustrate the application of this method in Chapters 6-7.

## CHAPTER

# 2

# FERROELECTRIC MATERIALS

Ferroelectric materials are characterized by the presence of spontaneous polarization in the absence of electric fields, at temperatures below the Curie point  $T_c$ . The materials exhibit tetragonal, orthorhombic or rhombohedral phases at these temperatures, where the orientation of polarization is determined by the coordinates of atoms in the unit cell. Additionally, this polarization orientation can be reversed by the application of an electric field or mechanical stress.

Ferroelectric materials are closely related to pyroelectric and piezoelectric materials. Pyroelectric materials develop a voltage due to an increase or decrease in temperature, and the polarization changes as a result. Many piezoelectric materials serve as actuators and sensors in the sense that they develop mechanical forces due to an applied electric field, and conversely develop a voltage due to an applied external force. In particular, they are characterized by the ability to produce a change in polarization when subjected to mechanical stress. This is termed the direct piezoelectric effect. Alternatively, the material can produce mechanical strain in response to an applied electric field, yielding the converse piezoelectric effect.

Because of the strong electromechanical properties of many ferroelectric materials, they are widely considered and employed as actuators and sensors in engineering applications. Commonly employed and/or studied ferroelectric materials include  $\text{BaTiO}_3$  (barium titanate),  $\text{Pb}(\text{Zr,Ti})\text{O}_3$  (lead zirconate titanate or PZT) and  $\text{Pb}(\text{Mg}_{1/3}\text{Nb}_{2/3})\text{O}_3$ - $\text{PbTiO}_3$  (lead magnesium niobate-lead titanate or PMN-PT). The solid state nature and nanopositioning accuracy make ferroelectric materials ideal for applications such as solid state ferroelectric random access memory (FeRAM) [47]. Additionally,

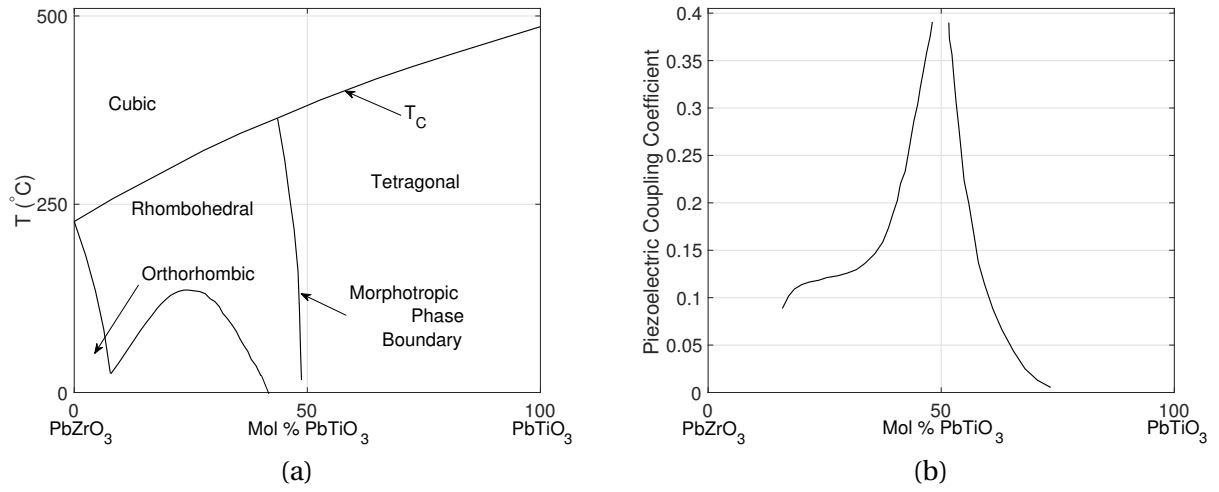


**Figure 2.1** (a) Dependence of the Curie temperature  $T_C$  on the molar fraction  $x$  of  $\text{PbZrO}_3$ , and morphotropic phase boundary separating rhombohedral from tetragonal structures. (b) Dependence of the piezoelectric coupling coefficient on the molar fraction  $x$ . Plotted after [22].

high energy efficiency rates and complementary direct and converse effects, provide excellent properties for the development of energy harvesting circuits [55], flow control transducers [2, 26], ultrasound transducer devices for biomedical imaging [36], and flying and ambulatory microrobots [20, 40, 62, 63].

The material studied, and of main interest in this dissertation, is  $\text{PbTiO}_3$ . This, along with  $\text{PbZrO}_3$  or lead zirconate, is a main component in PZT. These materials are present in PZT as part of the molar fraction  $x$  of Zr in  $\text{PbTi}_{1-x}\text{Zr}_x\text{O}_3$ . The determination of  $x$  is based on the desired optimal electromechanical properties for specific engineering applications. As depicted in the phase diagram of Figure 2.1(a),  $\text{PbZrO}_3$  exhibits a orthorhombic phase at temperatures below the Curie point, whereas  $\text{PbTiO}_3$  exhibits a tetragonal phase. Note that PZT is advantageous for transducer engineering applications due to its strong electromechanical coupling constant near the morphotropic phase boundary, as illustrated in Figure 2.1(a)-(b). Since lead titanate is a critical component in PZT, and density functional theory (DFT) calculations (Section 2.4) are facilitated for  $\text{PbTiO}_3$  as compared with  $\text{PbZrO}_3$  [37], we focus our attention on this material throughout this dissertation.

Because of its excellent transduction capabilities, PZT is largely used in place of other lead-free ferroelectric materials. Compared with the Curie temperature  $T_C = 120^\circ\text{C}$  for  $\text{BaTiO}_3$ , for example, Curie temperatures for PZT range from  $240^\circ\text{C} - 480^\circ\text{C}$ , thus providing higher operating temperatures and therefore more flexibility for different types of engineering applications. Compared with barium titanate, PZT also possesses a stronger piezoelectric response, which makes it a better material for



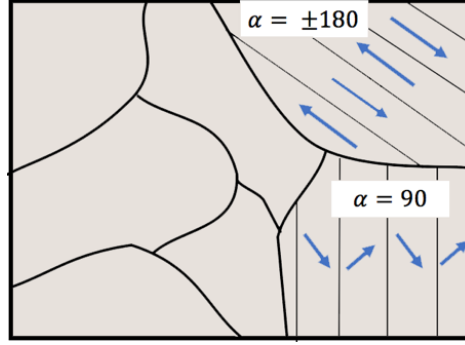


**Figure 2.2** Schematic of ferroelectric material grains depicting 180° and 90° domains and domain walls. Polarization is randomly oriented in the grains. Plotted after [52].

transducer designs.

A disadvantage of PZT is the presence of lead, which is toxic in the environment. As a result, significant effort has focused on developing new materials that can replace lead-based materials [21, 25], while maintaining the high performance required for applications. To develop new materials, it is critical to understand why lead-based ones are so effective. This starts with experimental and computational investigations ranging in scales from the material devices down to the micro-sized grains, nanoscale domains and atomic structure of the materials. A complete-structure evolution investigation thus requires the development of effective and efficient methods for characterizing free energy behavior within material grains. Energy relations across multiple scales can then be incorporated into homogenized energy frameworks, such as the one in [50, 52], to develop model-based control algorithms for bulk materials.

Within micro-sized grains, on scales of  $1\ \mu\text{m}$  -  $100\ \mu\text{m}$ , ferroelectric materials exhibit multidomain structures in which polarization is randomly oriented as defined by the atomic positions in twinned unit cells. These domain structures are separated by ferroelectric domain walls or boundaries, as depicted in Figure 2.2. This twinned domain structure occurs as an energy minimization mechanism as the material is cooled through the Curie temperature, from the paraelectric to ferroelectric phase. As detailed in [5, 32, 57, 59], domain walls contribute significantly to the nonlinearities, hysteresis, and dynamics at all scales in ferroelectric materials. Thus, understanding the properties of the domain walls is critical to the study of the governing physics of the materials. As a result, we study the monodomain energy response away from domain boundaries in Chapter 4, and focus on domain wall energies in Chapters 5 and 6. We provide a short introduction to single- and polydomain structures in Section 2.1 and 2.2, respectively.

## 2.1 Monodomain Structures

In terms of its unit cell, lead titanate exhibits a perovskite structure, with lead atoms occupying the A site and the titanium atom the B site. The material is cubic (paraelectric phase) above the Curie temperature  $T_C$  and it achieves its tetragonal (ferroelectric) phase when cooled below  $T_C$ . The material's internal energy for the paraelectric phase exhibits one unique minimum, whereas it exhibits two minima depending on the position of the Ti atom for its tetragonal phase, thereby determining the polarization orientation. A plot of the material energy profiles, along with the corresponding perovskite crystal structure is given in Figure 2.3. A macroscopic polarization is oriented in the  $x_3$  direction as dictated by the shift in the center Ti atom. When sufficient energy in the form of elastic or electrostatic forces is applied, the ion moves across the unstable equilibrium to the other potential well, thus producing a dipole switch, and a polarization jump at the macroscopic scale. In particular, the dipoles switch may be caused by the application of electric fields larger in magnitude than the coercive field  $E_C$ , denoting the field required to reduce polarization to zero. These switching mechanisms produce hysteresis and saturation nonlinearities, as illustrated in Figure 2.4. This behavior may be characterized by the implementation of the ferroelectric phase-field models discussed in Section 2.3.

When discussing monodomain structures, we refer to twinned unit cells with polarization orientation in the same direction within a single crystal. For a positive polarization  $P_3$  in the  $x_3$  direction, we plot the unit cell along with a single domain in Figure 2.5. In later chapters, we consider polarization rotation from  $x_3$  to  $x_2$ , and determine free energy associated with this domain structure evolution, informed by density functional theory (DFT) calculations as introduced in Section 2.4. Domains with polarization oriented in opposite directions or perpendicular to  $P_3$  are separated by domain walls or boundaries as detailed in the next section.

## 2.2 Polydomain Structures

The cooling of the material leads to the formation of many irregular nanoscale domain structures of polarization orientation. This produces one of the main sources of uncertainty at the micro-sized grain level, where nonlinearities are caused by many polarization-oriented structures. As depicted in Figure 2.2, each grain is composed of  $180^\circ$  and  $90^\circ$  domains in which oppositely- or perpendicularly-oriented polarization is separated by domain walls or boundaries. We illustrate a 2-D example of  $180^\circ$  and  $90^\circ$  polarization domains and domain walls in Figure 2.6. Here, we consider the domain walls to be positioned at  $x_1 = 0$ . In the case of the  $180^\circ$  domains, polarization is constrained to switch from negative to positive spontaneous polarization  $P_0$  in the  $x_3$  direction. For the  $90^\circ$  domains, polarization switches from orientation in the  $x_1$  direction to orientation in the  $x_2$  direction. In the model analysis, we work in a new rotated coordinate system  $(s, r, x_3)$  for convenience, as depicted

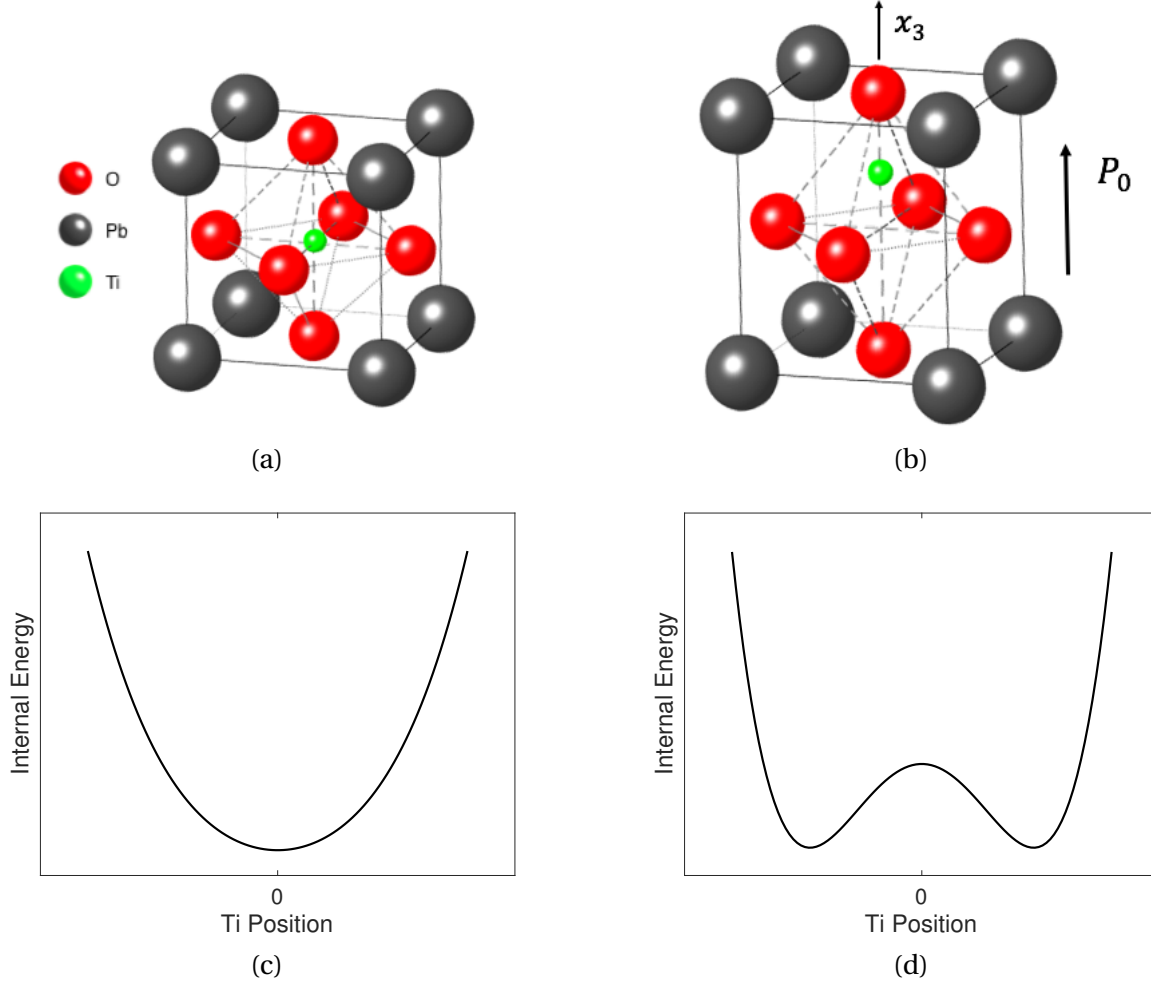


**Figure 2.3** Atomic structure unit cell of lead titanate (PbTiO<sub>3</sub>), with polarization oriented in the  $x_3$  direction. (a) Cubic form of PbTiO<sub>3</sub> in the paraelectric phase  $T > T_C$ . (b) Tetragonal structure of PbTiO<sub>3</sub>, along with spontaneous polarization  $P_0$  in the  $x_3$  direction. (c) PbTiO<sub>3</sub> internal energy as a function of the Ti position in the paraelectric phase  $T > T_C$ , and (d) in the ferroelectric phase  $T < T_C$ .

in Figure 2.6(b), with the domain wall positioned at  $s = 0$ . We present more details in Chapter 6.

We determine energy densities, total energy and corresponding model parameter sensitivities and uncertainties associated with 180° and 90° domain walls. Note that our analysis focuses on Pb-centered 180° domain walls that lie on Pb-O planes, whereas we consider Pb-Ti-O-centered 90° domain walls. As noted in [32], there is no sharp distinction between specific planes used for 90° domain wall centering, whereas domain wall energy results are the same when considering Pb- and Ti-centered 180° domain walls. Domain wall widths are reported to be on the order of the lattice constant  $a$  [32], which implies that transition takes place on the length scale of one unit cell. In

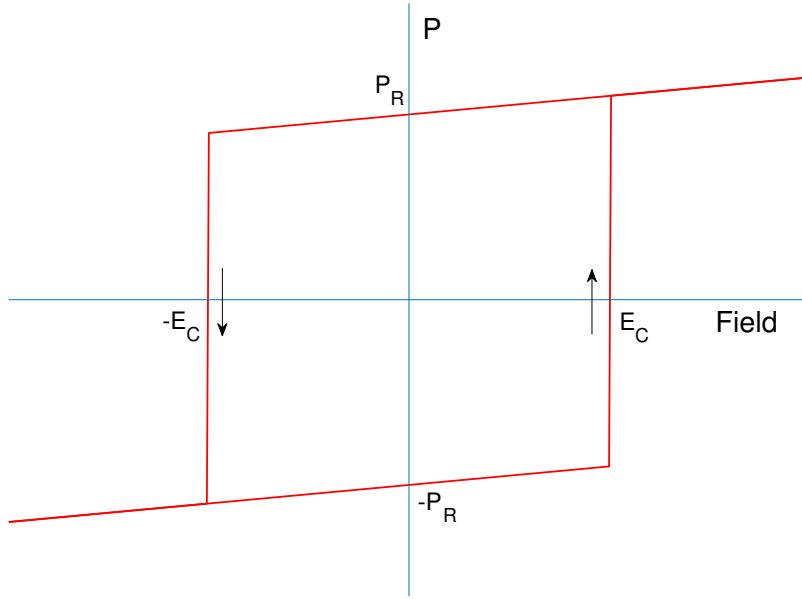


**Figure 2.4** Hysteretic field-polarization relation produced by ferroelectric switching mechanisms, when applied electric fields are larger than  $E_C$  in magnitude. The remanence polarization  $P_R$  occurs when the applied electric field is zero, where the linear and reversible direct and converse piezoelectric effects are applicable.

terms of the total domain wall energy, its values are reported to be  $132 \text{ mJ/m}^2$  and  $50 \text{ mJ/m}^2$ , for the  $180^\circ$  and  $90^\circ$  domain wall structures respectively [56].

### 2.3 Ferroelectric Phase-Field Model

The modeling of domain structure evolution for ferroelectric materials constitutes a significant challenge in materials science. Whereas density functional theory (DFT) simulations are accurate for determining many structure-property relationships in ferroelectric materials [16, 39], they are not feasible for large-scale computations in material design and engineering [48]. Other domain structure evolution methods consider the introduction of phase-field polarization and strain order parameters [6, 17, 31]. In phase-field models, the system structure is generally represented by the order parameters which, in this case, are polarization and strain. The phase-field represents the set of possible values for the order parameters. These methods are more computationally feasible since they approximate free energy in the nanoscale domain regions using coarser grids, with the

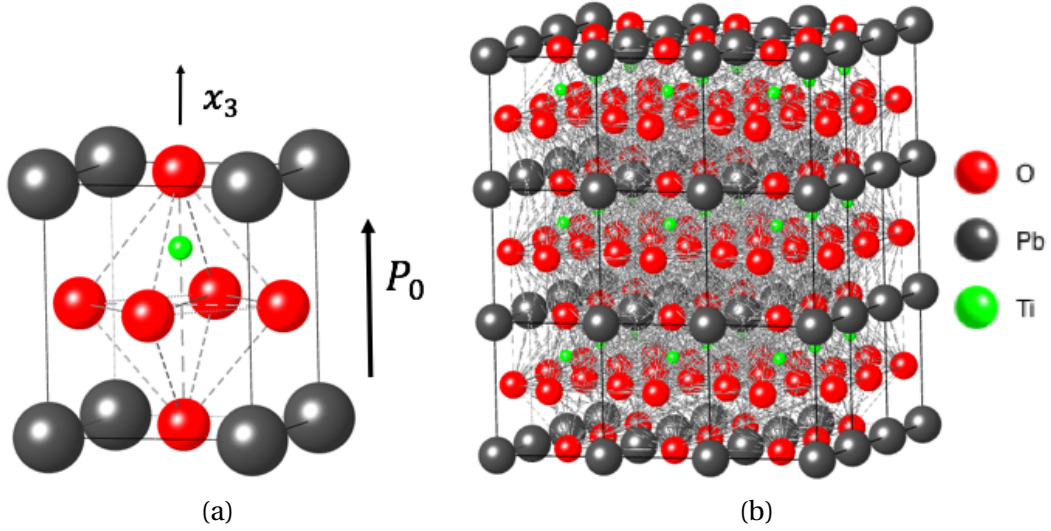


**Figure 2.5** (a) Ferroelectric phase for PbTiO<sub>3</sub>, with polarization oriented in the  $x_3$  direction. (b) Single domain structure for PbTiO<sub>3</sub>.

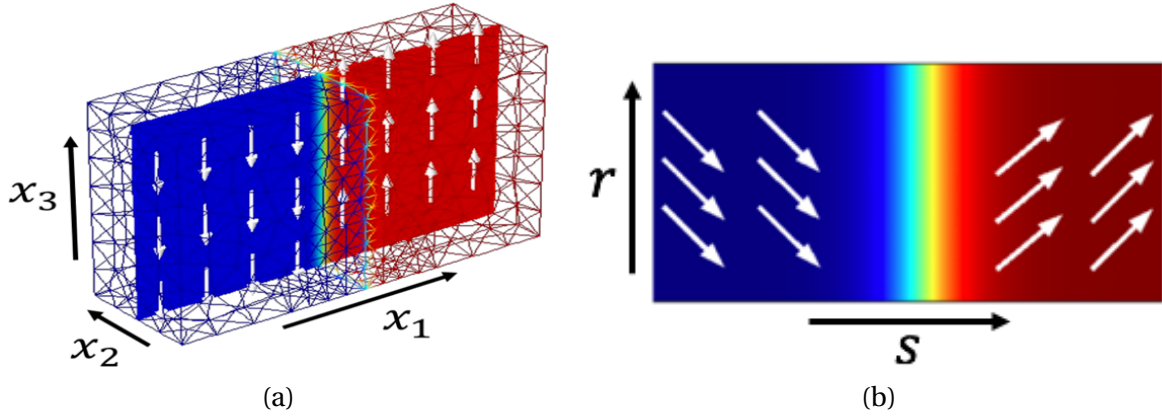


**Figure 2.6** (a) 180° and (b) 90° polydomain structures of polarization orientation. Domains are separated by corresponding domain walls or boundaries. We depict a new coordinate system for the 90° polydomain structure. As detailed in Section 2.2, this new 45°-rotated coordinate system is denoted by  $(s, r, x_3)$ , with the domain wall positioned at  $s = 0$ .

associated polarization and strain as the independent variables. Characterization of the electronic behavior via order parameters and nonlinear stress effects induced by domain wall structures produces uncertainty in the model response and parameters, due to the incorporation of quantum-scale effects into a continuum domain.

We focus on sensitivity analysis for model parameter selection, and uncertainty analysis and

propagation for free energy models informed by DFT simulations for lead titanate. These quantum-based calculations provide computational measures of polarization and free energy. Results obtained from [33] and other literature reference values [32, 56] are treated as high-fidelity calculations to inform our models for characterization of single- and multi-domain energy structures.

For linear operating regimes, corresponding to low input electric field levels, energy functionals, which incorporate linear electromechanical coupling, accurately characterize domain structure evolution. As detailed in [50], to incorporate additional ferroelectric hysteresis or phase transitions, it is necessary to quantify internal processes such as dipole switching or entropic effects in the absence of stresses or electromechanical coupling. To quantify this behavior, one can employ the Helmholtz energy relation

$$\psi(\varepsilon, P, T) = \frac{1}{2} Y^P \varepsilon^2 - a_1 \varepsilon P - a_2 \varepsilon P^2 + \psi_0(T) + \alpha_1 (T - T_C) P^2 + \alpha_2 P^4 + \alpha_3 P^6. \quad (2.1)$$

Here  $Y^P$  is the Young's modulus at constant polarization,  $a_1$  and  $a_2$  denote positive coupling coefficients,  $\alpha_1$  and  $\alpha_2$  are positive constants, and  $\psi_0(T)$  includes temperature effects independent of strain  $\varepsilon$  and polarization  $P$ . In comparison with energy functionals for linear operating regimes, relations such as (2.1) consider nonlinear electromechanical coupling terms, whose minima quantify polarization and strain densities in the absence of applied fields.

Whereas the Helmholtz energy relation (2.1), provides mechanisms for characterizing hysteresis in single crystal material compounds, we require a model that incorporates effects due to domain wall interactions as well as polarization and stress-dependent switching behavior across multiple domains. This is accomplished by using the Ginzburg-Landau theory for characterizing free energy [14], in which domain wall interactions are incorporated via the inclusion of polarization gradient terms of the form  $\frac{\partial P}{\partial x}$ . As illustrated in the work by Shu and Bhattacharya [49], Smith [50], Zhang and Bhattacharya [65], and further detailed in Chapter 4, the gradient energy terms incorporate local polarization changes due to domain wall effects. In addition, free energy is assumed to be nonlinearly dependent on quadratic, quartic and sextic polarization terms, and induced by electrostriction and a strain relationship motivated by Hooke's law.

In general, the phenomenological internal stored energy is divided into mechanical, polarization, electrostrictive, and gradient energy terms. Since one electronic coordinate vector is used to approximate the internal electronic structure in the DFT studies in [37], a polarization order parameter  $\mathbf{P}$  is used to represent the state. Thus, we treat polarization  $\mathbf{P}$  and strain  $\varepsilon$  as independent variables in the system. The 3-D stored free energy in the material polydomain system is thus given by

$$u(\mathbf{P}, \varepsilon) = u_M(\varepsilon) + u_P(\mathbf{P}) + u_C(\mathbf{P}, \varepsilon) + u_G(\mathbf{P}, \varepsilon), \quad (2.2)$$

which depends on the mechanical energy  $u_M$ , Landau or polarization energy  $u_P$ , electrostrictive

energy  $u_C$  and gradient energy  $u_G$ . For the analysis of the monodomain structures, we consider the first three terms on the right hand side of system (2.2), whereas we include the gradient energy term for analysis of the polydomain structures. Additionally, a residual energy term  $u_R$  is considered to compare with results from DFT studies where the unit cell is held fixed with respect to a reference cubic state. We provide more details about the residual energy in Chapter 4.

Our goal is to determine which phenomenological parameters are influential or identifiable in the sense that they are uniquely determined by available data as detailed in Section 1.1. In the case of the Landau energy

$$\begin{aligned} u_P(\mathbf{P}) = & \alpha_1 (P_1^2 + P_2^2 + P_3^2) + \alpha_{11} (P_1^2 + P_2^2 + P_3^2)^2 + \alpha_{12} (P_1^2 P_2^2 + P_2^2 P_3^2 + P_1^2 P_3^2) \\ & + \alpha_{111} (P_1^6 + P_2^6 + P_3^6) + \alpha_{112} [P_1^4 (P_2^2 + P_3^2) + P_2^4 (P_1^2 + P_3^2) \\ & + P_3^4 (P_1^2 + P_2^2)] + \alpha_{123} P_1^2 P_2^2 P_3^2, \end{aligned} \quad (2.3)$$

one seeks to determine whether or not a sixth-order expansion is necessary as compared to using a fourth-order expansion for characterization of phase transition and monodomain structure evolution. Relation (2.3) is analogous to the fifth, sixth and seventh terms in (2.1), with the exception that (2.3) incorporates 3-D polarization effects. Additionally, in (2.3) we consider a temperature  $T < T_C$  such that  $\alpha_1$  is an unknown phenomenological parameter whose value is less than zero.

The gradient energy density is taken to be

$$\begin{aligned} u_G(P_{i,j}) = & \frac{g_{11}}{2} (P_{1,1}^2 + P_{2,2}^2 + P_{3,3}^2) + g_{12} (P_{1,1} P_{2,2} + P_{1,1} P_{3,3} + P_{2,2} P_{3,3}) \\ & + \frac{g_{44}}{2} [(P_{1,2} + P_{2,1})^2 + (P_{1,3} + P_{3,1})^2 + (P_{2,3} + P_{3,2})^2], \end{aligned} \quad (2.4)$$

where  $g_{11}$ ,  $g_{12}$  and  $g_{44}$  denote the exchange parameters and

$$P_{i,j} = \frac{\partial P_i}{\partial x_j}$$

is the polarization gradient. For 180° and 90° domain wall polarization effects, we seek to determine the influential exchange parameters in (2.4), in the sense that their uncertainties directly contribute to the uncertainty in the response.

The mechanical and electrostrictive energy  $u_M$  and  $u_C$  are also analogous to the first, second and third terms in (2.1). We present the complete form of (2.2), as well as more details about the model analysis in Chapters 4-7.

## 2.4 Density Functional Theory Calculations

Density functional theory (DFT) calculations describe the quantum behavior of atoms and molecules through solutions of the Schrödinger equation. As such, DFT is used to determine many structure-dependent properties for collections of atoms. Of particular importance is the energy calculation of atoms and the change in energy as these atoms are moved. To effectively determine these energy states, solutions of the atoms' electron densities are required. The ground state energy  $E$  of the electrons, in Schrödinger's equation, is then expressed as the functional  $E[n(\mathbf{r})]$ , where  $n(\mathbf{r})$  is the electron density for a particular 3-coordinate position vector  $\mathbf{r}$ . This motivates the name *density functional theory*. More details about the theory behind DFT are provided in sources including [48, 64, 66]

For the ferroelectric phase-field model studied in this dissertation, DFT informs the continuum scale Landau energy and stresses associated with several uniform polarization states in lead titanate. For the monodomain structures, we use the DFT calculations from [33], treated as high fidelity results, to quantify the uncertainty in the Landau energy parameters and electrostrictive energy coefficients, in the stored energy (2.2). Model parameter uncertainty is present since we are going from a quantum DFT calculation to a continuum framework description using polarization as the order parameter.

As detailed in [33, 37], the DFT calculations for the monodomain structure were performed using ABINIT 7.0.5 [16] for lead titanate ( $\text{PbTiO}_3$ ). Starting with the centrosymmetric atomic configuration, atoms were linearly incremented, yielding an equilibrium tetragonal state and a double well potential energy. To estimate the full three-dimensional energy surface, atomic displacements under internal atomic shearing were used, quantifying polarization not aligned with the spontaneous polarization direction. Note that the corresponding polarization for the atomic displacement configurations was obtained using the Berry phase approach [43]. This yields the polarization rotation profiles plotted in Figure 2.7, for which DFT energy and stresses are calculated. More details about the DFT computational experiment for the monodomain analysis are provided in [33, 34, 37]

In the case of polydomain structures, we consider DFT calculations for  $180^\circ$  and  $90^\circ$  domain walls in [32, 56]. The reported values for the  $180^\circ$  and  $90^\circ$  domain wall energies are  $132 \text{ mJ/m}^2$  and  $50 \text{ mJ/m}^2$ , respectively. We use these values to quantify the uncertainty in the exchange parameters of the gradient energy  $u_G$  in (2.2). We provide more details in Chapters 5-7.



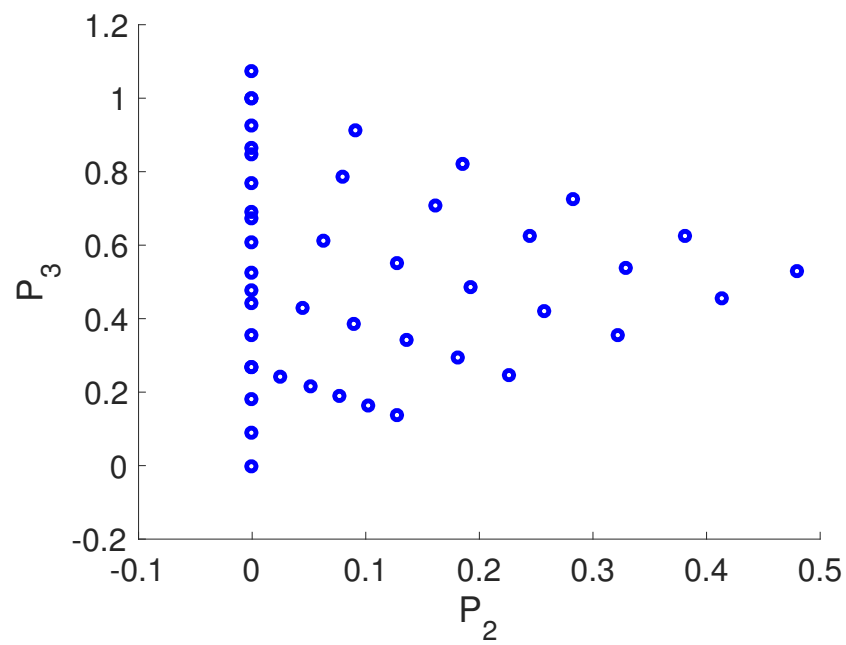


**Figure 2.7** Polarization states at which DFT energy and stresses were calculated in the computational study of [33].

## CHAPTER

# 3

# PARAMETER SUBSET SELECTION AND UNCERTAINTY QUANTIFICATION

In Chapter 1, we introduced the concept of influential and identifiable parameters, whereas in Chapter 2 we provided motivation for parameter subset selection in ferroelectric material models. In this chapter, we introduce global sensitivity analysis techniques, starting with Pearson correlation coefficients and including Morris screening methods and variance-based Sobol’ decomposition methods. Section 3.1 considers these methods with the assumption that the parameters are independently and uniformly distributed. Section 3.2 details the problems that arise when the parameters are actually correlated, and presents an alternate variance-based sensitivity analysis methodology based originally on the work by Li [29]. In Section 3.3, we consider a parameter subset selection methodology based on the Fisher information matrix, for identifying locally identifiable parameters. In Section 3.4, we present parameter subspace selection methodologies, including using active subspaces to determine activity scores as a sensitivity analysis alternative. Lastly, in Section 3.5 and 3.6, we summarize Bayesian inference and uncertainty propagation and detail how the parameter subset selection results are used to determine noninfluential parameters, which may be fixed in uncertainty quantification.

Consider the input-output system described by the relation

$$Y = f(\Theta), \tag{3.1}$$

where  $Y$  denotes the output and  $\Theta = [\Theta_1, \Theta_2, \dots, \Theta_p]$  denotes random input parameters. We let  $\theta$  and  $y$  denote realizations of the random variables  $\Theta$  and  $Y$ . The mean and variance are defined by

$$f_0 = \mathbb{E}[Y] = \int_{\Gamma} \rho(\theta) f(\theta) d\theta \quad (3.2)$$

and

$$D = \text{Var}[Y] = \mathbb{E}[(Y - \mathbb{E}[Y])^2] = \int_{\Gamma} \rho(\theta) f^2(\theta) d\theta - f_0^2. \quad (3.3)$$

Here,  $\Gamma$  is defined as the parameter space and  $\rho(\theta)$  is the probability density function for  $\theta$ .

The objective of sensitivity analysis is to quantify the sensitivity of the response  $Y$  to the parameters  $\Theta$ . In local sensitivity analysis, this is quantified by the derivative

$$\frac{\partial f}{\partial \theta_i}(\theta^*) \quad (3.4)$$

with respect to the parameter  $\theta_i$  evaluated at a nominal parameter value  $\theta^*$ . Alternatively, global sensitivity analysis more broadly quantifies the manner in which uncertainties in the response are apportioned to uncertainties in the model inputs. This is described in more detail in Chapter 15 of Smith [51] and in Saltelli et al. [45].

To perform global sensitivity analysis, we first determine maps for the parameter  $\theta_i$  realizations between the arbitrary physical interval  $[\theta_{\ell_i}, \theta_{u_i}]$  and the unit interval  $[0, 1]$ . In all the analyses, where the parameters are uniformly distributed, we randomly sample from the uniform distribution  $\mathcal{U}(0, 1)$  and then map to  $[\theta_{\ell_i}, \theta_{u_i}]$  before evaluating the physical model.

For general intervals  $[a, b]$  and  $[A, B]$ , the map  $g : [a, b] \rightarrow [A, B]$  is defined by

$$g(x) = \frac{x - a}{b - a}(B - A) + A$$

for  $x \in [a, b]$ . When  $[a, b] = [0, 1]$  and  $[A, B] = [\theta_{\ell_i}, \theta_{u_i}]$ , this yields the map

$$g(x) = x(\theta_{u_i} - \theta_{\ell_i}) + \theta_{\ell_i}. \quad (3.5)$$

If  $\theta_{\ell}$  and  $\theta_u$  are vectors for the lower and upper bounds of the physical intervals for the parameters  $\theta$ , then for  $\mathbf{x} \in [0, 1]^p$ , this yields

$$\theta = g(\mathbf{x}) = \text{diag}(\theta_u - \theta_{\ell})\mathbf{x} + \theta_{\ell}. \quad (3.6)$$

## Pearson Correlations

To obtain initial sensitivity indices, one often begins with centered parameter studies in which one individually perturbs parameters about nominal values to ascertain individual effects. As detailed previously, we randomly sample parameters from  $\mathcal{U}(0, 1)$  and map them to physical intervals  $[\theta_{\ell_i}, \theta_{u_i}]$  via the transformation (3.5).

To qualitatively observe the degree to which the responses depend on individual parameter variations, one can draw  $M$  samples from  $\mathcal{U}(0, 1)$  for each parameter and plot scatterplots of the realizations  $y$  as a function of  $\theta_i$  for  $i = 1, \dots, p$ . The correlation between the individual parameters  $\Theta_i$  and the output  $Y$  can be quantified by the Pearson correlation coefficient

$$\rho_i = \frac{\sum_{j=1}^M (\theta_i^j - \bar{\theta}_i)(y_j - \bar{y})}{\sqrt{\sum_{j=1}^M (\theta_i^j - \bar{\theta}_i)^2 \sum_{k=1}^M (y_k - \bar{y})^2}}, \quad (3.7)$$

where  $\theta_i^j$  and  $y_j$  are realizations of  $\Theta_i$  and  $Y$ , and  $\bar{\theta}_i$  and  $\bar{y}$  are the respective sample means. Parameters having large Pearson correlation coefficients are considered more influential on the response than those having small values as they reflect the trend of the model output. We note that this method quantifies only linear interactions and will not detect nonlinear interactions between parameters and outputs.

## 3.1 Global Sensitivity Analysis for Uncorrelated Inputs

In this section, we detail global sensitivity analysis techniques for models with uniformly and independently distributed parameters. We detail Morris screening in Section 3.1.1 and variance-based global sensitivity analysis in Section 3.1.2.

### 3.1.1 Morris Screening

In Morris screening [35], a measure of global sensitivity is provided by the average of finite-difference relations, referred to as elementary effects. The individual effects of parameters and the effect of interaction terms on the model response are respectively represented by the mean  $\mu_i^*$  and variance  $\sigma_i^2$  of the elementary effects. This method is typically quite computationally efficient and exhibits less dependence on potentially unknown parameter distributions than the variance-based method of Section 3.1.2.

To compute the elementary effects, the parameters are again mapped to  $[0, 1]^p$  and taken to be uniformly distributed as  $\theta_i \sim \mathcal{U}(0, 1)$ . The elementary effect for  $\theta_i$  is given by

$$d_i(\theta) = \frac{f(\theta_1, \dots, \theta_{i-1}, \theta_i + \Delta, \theta_{i+1}, \dots, \theta_p) - f(\theta)}{\Delta}. \quad (3.8)$$

In the analysis presented here, we employ a value of  $\Delta = \frac{1}{49}$ , as motivated by [51]. To compute parameter sensitivity measures, we first let

$$d_i^j = \frac{f(\theta^j + \Delta \mathbf{e}_i) - f(\theta^j)}{\Delta},$$

denote the elementary effect corresponding to the  $i^{\text{th}}$  parameter and  $j^{\text{th}}$  sample. We then employ the sensitivity indices

$$\mu_i^* = \frac{1}{s} \sum_{j=1}^s |d_i^j(\theta)|, \quad (3.9)$$

and

$$\sigma_i^2 = \frac{1}{s-1} \sum_{j=1}^s (d_i^j - \mu_i)^2, \quad \text{for } \mu_i = \frac{1}{s} \sum_{j=1}^s d_i^j. \quad (3.10)$$

Here, the index  $\mu_i^*$  quantifies effects due to individual parameter perturbations, while  $\sigma_i^2$  quantifies nonlinearities and interactions with other inputs in the admissible parameter space. Since two model evaluations are required per parameter, this yields a total of  $2ps$  model evaluations to compute the Morris sensitivity measures (3.9) and (3.10). The Morris screening strategy as presented in [61] is provided in Algorithm 3.1.1.

### 3.1.2 Variance-Based Sensitivity Analysis

To construct variance-based global sensitivity indices, we start by decomposing the model  $f(\theta)$  into its Sobol' decomposition [53],

$$\begin{aligned} f(\theta) &= f_0 + \sum_{i=1}^p f_i(\theta_i) + \sum_{1 \leq i < j \leq p} f_{ij}(\theta_i, \theta_j) + \dots + f_{12\dots p}(\theta_1, \dots, \theta_p) \\ &= f_0 + \sum_{n=1}^{2^p-1} f_{r_n}(\theta_{r_n}), \end{aligned} \quad (3.11)$$

where  $p$  denotes the number of parameters and  $r_n$ ,  $1 \leq n \leq 2^p - 1$ , represents all the sets  $\{i | 1 \leq i \leq p\}$ ,  $\{i | 1 \leq i < j \leq p\}, \dots$ . For example, the first- and second-order component functions are

$$1^{\text{st}} \text{ order: } f_{r_1}(\theta_{r_1}) = f_1(\theta_1), \dots, f_{r_p}(\theta_{r_p}) = f_p(\theta_p),$$

$$2^{\text{nd}} \text{ order: } f_{r_{p+1}}(\theta_{r_{p+1}}) = f_{12}(\theta_1, \theta_2), \dots, f_{r_{p+p_2}}(\theta_{r_{p+p_2}}) = f_{p-1,p}(\theta_{p-1}, \theta_p),$$

where  $p_2 = \binom{p}{2}$ . Note that this follows the functional form employed in Li [29]. The decomposition (3.11) is subject to the expected value condition

---

**Algorithm 3.1.1:** Morris screening sampling strategy.

---

1. A strictly lower triangular  $(p+1) \times p$  matrix  $\mathbf{B}$  is first created such that

$$\mathbf{B} = \begin{bmatrix} 0 & \cdots & 0 & 0 \\ 1 & \ddots & \vdots & \vdots \\ \vdots & \ddots & 0 & 0 \\ 1 & \cdots & 1 & 0 \end{bmatrix}.$$

2. Take the step size to be  $\Delta = \frac{1}{49}$ .
3. Choose an initial vector  $\theta^* \in I^{1 \times p}$ .
4. Build a diagonal  $p \times p$  matrix  $\mathbf{D}^*$ , with randomly chosen entries from  $\{-1, 1\}$ .
5. Construct a  $(p+1) \times p$  matrix  $J_{p+1,p}$  with entries equal to 1 and a  $p \times p$  permutation  $\mathbf{P}^*$  of the identity matrix to compute the sampling matrix

$$\mathbf{B}^* = J_{p+1,p} \theta^* + \frac{\Delta}{2} [(2\mathbf{B} - J_{p+1,p}) \mathbf{D}^* + J_{p+1,p}] \mathbf{P}^*.$$

6. Let  $\mathbf{C}_r^*$  denote the  $r^{\text{th}}$  row of  $\mathbf{C}^*$ . We then compute the elementary effects

$$d_i = \frac{f(\mathbf{C}_n^*) - f(\mathbf{C}_m^*)}{\Delta},$$

so that the  $n^{\text{th}}$  and  $m^{\text{th}}$  rows differ in the  $i^{\text{th}}$  entry.

7. For  $s$  samples, repeat procedure in steps 1-7.
8. Compute the average and variance of the local elementary effects

$$\mu_i^* = \frac{1}{s} \sum_{j=1}^s |d_i^j(\theta)|,$$

$$\sigma_i^2 = \frac{1}{s-1} \sum_{j=1}^s (d_i^j - \mu)^2, \quad \text{where } \mu = \frac{1}{s} \sum_{j=1}^s d_i^j$$

to determine the Morris measures. Large indices represent more influential parameters.

---

$$\mathbb{E}[f_{r_n}(\Theta_{r_n})] = \int_{\Gamma_{r_n}} \rho(\theta_{r_n}) f_{r_n}(\theta_{r_n}) d\theta_{r_n} = 0. \quad (3.12)$$

Here,  $\rho(\theta_{r_n})$  is the joint probability density function for the set of parameters  $\theta_{r_n}$ .

We define the component functions from (3.11) by the relations

$$\begin{aligned} f_0 &= \int_{\Gamma} \rho(\theta) f(\theta) d\theta = \mathbb{E}[Y], \\ f_i(\theta_i) &= \int_{\Gamma_{\sim i}} \rho_{\sim i}(\theta_{\sim i}) f(\theta) d\theta_{\sim i} - f_0 = \mathbb{E}[Y|\theta_i] - f_0, \quad (1 \leq i \leq p), \\ f_{ij}(\theta_i, \theta_j) &= \int_{\Gamma_{\sim \{ij\}}} \rho_{\sim \{ij\}}(\theta_{\sim \{ij\}}) f(\theta) d\theta_{\sim \{ij\}} - f_i(\theta_i) - f_j(\theta_j) - f_0 \\ &= \mathbb{E}[Y|\theta_i, \theta_j] - f_i - f_j - f_0, \quad (1 \leq i < j \leq p), \\ &\vdots \\ f_{1\dots p}(\theta_1, \dots, \theta_p) &= f(\theta) - f_0 - \sum_{1 \leq i \leq p} f_i - \sum_{1 \leq i < j \leq p} f_{ij} - \sum_{1 \leq i < j < k \leq p} f_{ijk} - \dots, \end{aligned} \quad (3.13)$$

which express contributions from each subset of parameters  $\theta_{r_n}$ . In (3.13),  $\Gamma$ ,  $\Gamma_{\sim i}$  and  $\Gamma_{\sim \{ij\}}$  are the image spaces for  $\theta$ ,  $\theta_{\sim i} \equiv [\theta_1, \dots, \theta_{i-1}, \theta_{i+1}, \dots, \theta_p]$  and

$$\theta_{\sim \{ij\}} \equiv [\theta_1, \dots, \theta_{i-1}, \theta_{i+1}, \dots, \theta_{j-1}, \theta_{j+1}, \dots, \theta_p].$$

Additionally,  $\rho_{\sim i}(\theta_{\sim i})$  and  $\rho_{\sim \{ij\}}(\theta_{\sim \{ij\}})$  denote the conditional probability density functions for  $\theta_{\sim i}$  and  $\theta_{\sim \{ij\}}$  given  $\theta_i$  and  $(\theta_i, \theta_j)$ , respectively. We can define the variance of the component functions by

$$D_{r_n} = \text{Var}[f_{r_n}(\Theta_{r_n})] = \mathbb{E}[(f_{r_n}(\Theta_{r_n}) - \mathbb{E}[f_{r_n}(\Theta_{r_n})])^2] = \int_{\Gamma_{r_n}} \rho(\theta_{r_n}) f_{r_n}^2(\theta_{r_n}) d\theta_{r_n}. \quad (3.14)$$

For earlier studies of variance-based global sensitivity analysis, the response  $Y = f(\Theta)$  was generally approximated by a subset of all the possible component functions [45, 46, 51]. In this section we consider the scenario in which each of the parameters  $\Theta_i$  is independently distributed and  $\Theta_i \sim \mathcal{U}(0, 1)$ , such that each individual range is  $\Gamma = [0, 1]$ . This yields the range  $\Gamma^p$  and joint density  $\rho(\Theta)$  for  $\Theta$ ,

$$\Gamma^p = \prod_{k=1}^p \Gamma, \quad \rho(\theta) = \prod_{k=1}^p \rho(\theta_k),$$

respectively. This assumption, along with the Sobol' decomposition (3.11), yields the variance

decomposition

$$D = \text{Var}[Y] = \sum_{n=1}^{2^p-1} \text{Var}[f_{r_n}(\Theta_{r_n})] = \sum_{n=1}^{2^p-1} D_{r_n}. \quad (3.15)$$

We consider the output  $f(\theta)$  to be adequately represented by the second-order expansion

$$f(\theta) = f_0 + \sum_{i=1}^p f_i(\theta_i) + \sum_{1 \leq i < j \leq p} f_{ij}(\theta_i, \theta_j). \quad (3.16)$$

Relation (3.12) then yields the constraints

$$\int_0^1 f_i(\theta_i) d\theta_i = \int_0^1 f_{ij}(\theta_i, \theta_j) d\theta_i = \int_0^1 f_{ij}(\theta_i, \theta_j) d\theta_j = 0$$

to ensure that the component functions are orthogonal and uniquely defined in the sense that

$$\int_{\Gamma^2} f_i(\theta_i) f_j(\theta_j) d\theta_i d\theta_j = \int_{\Gamma_{ij}} f_i(\theta_i) f_{ij}(\theta_i, \theta_j) d\theta_i d\theta_j = 0, \quad i, j = 1, \dots, p.$$

The expected values in (3.13) are then reduced to

$$\begin{aligned} f_0 &= \mathbb{E}(Y) = \int_{\Gamma^p} f(\theta) d\theta \\ f_i(\theta_i) &= \mathbb{E}(Y|\theta_i) - f_0 = \int_{\Gamma^{p-1}} f(\theta) d\theta_{\sim i} - f_0 \\ f_{ij}(\theta_i, \theta_j) &= \mathbb{E}(Y|\theta_i, \theta_j) - f_i(\theta_i) - f_j(\theta_j) - f_0 = \int_{\Gamma^{p-2}} f(\theta) d\theta_{\sim \{i,j\}} - f_i(\theta_i) - f_j(\theta_j) - f_0, \end{aligned} \quad (3.17)$$

where  $\theta_{\sim i} = [\theta_1, \dots, \theta_{i-1}, \theta_{i+1}, \dots, \theta_p]$ . To construct sensitivity indices, we define the total and partial variances

$$\begin{aligned} D &= \int_{\Gamma^p} f^2(\theta) d\theta - f_0^2 = \text{Var}[Y], \\ D_i &= \int_0^1 f_i^2(\theta_i) d\theta_i = \text{Var}[\mathbb{E}(Y|\theta_i)], \\ D_{ij} &= \int_0^1 \int_0^1 f_{ij}(\theta_i, \theta_j) d\theta_i d\theta_j = \text{Var}[\mathbb{E}(Y|\theta_i, \theta_j)] - \text{Var}[\mathbb{E}(Y|\theta_i)] - \text{Var}[\mathbb{E}(Y|\theta_j)]. \end{aligned}$$

This yields the Sobol' indices

$$S_i = \frac{D_i}{D} = \frac{\text{Var}[\mathbb{E}(Y|\theta_i)]}{\text{Var}[Y]}, \quad S_{ij} = \frac{D_{ij}}{D}, \quad i = 1, \dots, p, \quad (3.18)$$



satisfying

$$\sum_{i=1}^p S_i + \sum_{1 \leq i < j \leq p} S_{ij} = 1. \quad (3.19)$$

We also define the total sensitivity indices

$$S_{T_i} = S_i + \sum_{\substack{j=1 \\ i \neq j}}^p S_{ij} = 1 - \frac{\text{Var}[\mathbb{E}(Y|\theta_{\sim i})]}{\text{Var}[Y]}, \quad (3.20)$$

quantifying total effects of the parameter  $\theta_i$  including higher order interactions on the response.

We note that a rough guideline is to consider indices  $S_i$  greater than  $\frac{100}{p}\%$  as significant when analyzing Sobol' indices. This is because, in the absence of interactions, indices with this magnitude have greater than average effect on the response variability.

In most cases, the computation of the Sobol' indices (3.18) and (3.20) is prohibitive when using tensor product-based quadrature to estimate integrals over  $\Gamma^p$ ,  $\Gamma^{p-1}$  and  $\Gamma^{p-2}$ . In such cases, rather than implementing sparse grid quadrature techniques, we employ the techniques of Saltelli and other authors [38, 45, 46, 54, 60] for constructing Monte Carlo-based estimators for  $S_i$  and  $S_{T_i}$ . We implement Algorithm 3.1.2 for our global sensitivity analysis, which has variations from [46, 54, 60], as illustrated in [61].

## 3.2 Global Sensitivity Analysis for Correlated Inputs

In the classical global sensitivity analysis methods summarized in the previous section, one typically assumes uniformly and independently distributed model inputs in absence of additional information. However, when the parameters are strongly correlated, we need to verify whether or not this assumption may lead to incorrect interpretations about parameter sensitivities.

To address this issue, we expand the variance-based Sobol' decomposition method detailed in Section 3.1.2 to include contributions due to parameter correlation. We then summarize total sensitivity indices, which accurately account for underlying parameter correlation. When the model is linearly parameterized, we show that an analytic solution for the component functions in the Sobol' decomposition is available. Additionally, we provide a general method for determining component functions for nonlinearly parameterized problems based on basis function expansions. We detail the associated methodology next.

---

**Algorithm 3.1.2:** Saltelli algorithm for computing Sobol' sensitivity indices for uniform densities [46]

---

- (1) First create two  $M \times p$  matrices

$$\mathbf{A} = \begin{bmatrix} \theta_1^1 & \dots & \theta_i^1 & \dots & \theta_p^1 \\ \vdots & & \vdots & & \vdots \\ \theta_1^M & \dots & \theta_i^M & \dots & \theta_p^M \end{bmatrix} \text{ and } \mathbf{B} = \begin{bmatrix} \hat{\theta}_1^1 & \dots & \hat{\theta}_i^1 & \dots & \hat{\theta}_p^1 \\ \vdots & & \vdots & & \vdots \\ \hat{\theta}_1^M & \dots & \hat{\theta}_i^M & \dots & \hat{\theta}_p^M \end{bmatrix}.$$

The entries of these matrices are pseudo-random numbers drawn from the respective density. Note that  $M$  is the number of samples and  $p$  stands for the number of parameters in the model.

- (2) Then, create  $p$   $M \times p$  matrices

$$\mathbf{A}_B^{(i)} = \begin{bmatrix} \hat{\theta}_1^1 & \dots & \theta_i^1 & \dots & \hat{\theta}_p^1 \\ \vdots & & \vdots & & \vdots \\ \hat{\theta}_1^M & \dots & \theta_i^M & \dots & \hat{\theta}_p^M \end{bmatrix}, \quad i = 1, \dots, p,$$

where, as can be observed, the entries are identical to  $\mathbf{A}$ , with the exception of the  $i^{\text{th}}$  column which is taken from  $\mathbf{B}$ . Create  $\mathbf{B}_A^{(i)}$  in a similar manner.

- (3) Create

$$\mathbf{C} = \begin{bmatrix} \mathbf{A} \\ - \\ \mathbf{B} \end{bmatrix}, \quad (3.21)$$

which is the  $\mathbf{B}$  matrix appended to matrix  $\mathbf{A}$ .

- (4) Compute the column vectors  $f(\mathbf{A})$ ,  $f(\mathbf{B})$ ,  $f(\mathbf{A}_B^{(i)})$  and  $f(\mathbf{B}_A^{(i)})$  by evaluating the model at input values from the rows of matrices  $\mathbf{A}$ ,  $\mathbf{B}$ ,  $\mathbf{A}_B^{(i)}$  and  $\mathbf{B}_A^{(i)}$ . Here  $f(\mathbf{A})_j$  denotes the output computed from the  $j^{\text{th}}$  row of  $\mathbf{A}$ .

- (5) The first-order Sobol' indices are estimated by

$$S_i \approx \frac{\frac{1}{M} \sum_{j=1}^M [f(\mathbf{A})_j f(\mathbf{B}_A^{(i)})_j - f(\mathbf{A})_j f(\mathbf{B})_j]}{\frac{1}{2M} \sum_{j=1}^{2M} f(\mathbf{C})_j f(\mathbf{C})_j - E^2[f(\mathbf{C})]} \quad (3.22)$$

and the total indices by

$$S_{Ti} \approx \frac{\frac{1}{2M} \sum_{j=1}^M [f(\mathbf{A})_j - f(\mathbf{A}_B^{(i)})_j]^2}{\frac{1}{2M} \sum_{j=1}^{2M} f(\mathbf{C})_j f(\mathbf{C})_j - E^2[f(\mathbf{C})]}. \quad (3.23)$$


---

---

In (3.22), we approximated the squared mean,

$$f_0^2 = \int_{\Gamma^p} f(\theta)f(\theta')d\theta d\theta'$$

by

$$f_0^2 \approx \frac{1}{M} \sum_{j=1}^M f(\mathbf{A})_j f(\mathbf{B})_j, \quad (3.24)$$

as motivated in [45, 54].

---

### 3.2.1 Variance-Based Sensitivity Analysis

As noted in Section 3.1.2, the function  $Y = f(\Theta)$  is expressed in terms of its Sobol' decomposition

$$Y = f(\Theta) = f_0 + \sum_{n=1}^{2^p-1} f_{r_n}(\theta_{r_n}). \quad (3.25)$$

In the previous section, we illustrated how a second-order approximation (3.16) is used in the Saltelli algorithms from [46, 54, 60]. Independent of the second-order approximation, these algorithms also assume that the parameters  $\Theta$  are uniformly and independently distributed. In this section, we consider cases for which the assumption of independent inputs is false. We will start by considering an alternate decomposition of the model variance  $\text{Var}[Y]$ , such that this incorporates possible correlations and structural interactions between the model parameters. We illustrate the alternate derivation of the sensitivity indices based on the theory developed by Li [29].

Consider the Hilbert inner product  $\langle \cdot, \cdot \rangle_\rho$ ,

$$\langle f(\theta), g(\theta) \rangle_\rho = \int_{\Gamma} \rho(\theta) f(\theta) g(\theta) d\theta \quad (3.26)$$

for two arbitrary functions  $f(\theta)$  and  $g(\theta)$ . Using the Hilbert inner product, relations (3.11), (3.14), (3.25), and the definition of variance, then yield the variance decomposition

$$\begin{aligned}
\text{Var}[Y] &= \mathbb{E}[(Y - \mathbb{E}[Y])^2] = \left\langle \sum_{j=1}^{2^p-1} f_{r_j}, y - f_0 \right\rangle_{\rho} \\
&= \sum_{j=1}^{2^p-1} \text{Cov}[f_{r_j}, Y] \\
&= \sum_{j=1}^{2^p-1} \text{Var}[f_{r_j}] + \text{Cov} \left[ f_{r_j}, \sum_{k=1, k \neq j}^{2^p-1} f_{r_k} \right],
\end{aligned} \tag{3.27}$$

where

$$\text{Cov}[f_{r_k}, Y] = \int_{\Gamma} \rho(\theta) f_{r_k}(\theta_{r_k}) [f(\theta) - f_0] d\theta. \tag{3.28}$$

Whereas the relation  $\sum_{j=1}^{2^p-1} \text{Var}[f_{r_j}]$  accounts for individual parameter contributions to the total variance  $\text{Var}[Y]$ , the covariance

$$\text{Cov} \left[ f_{r_j}, \sum_{k=1, k \neq j}^m f_{r_k} \right]$$

accounts for correlation present in the component functions of the sets  $\theta_{r_j}$  and  $\theta_{r_k}$ .

As a counterpart to the sensitivity indices defined in (3.18) and (3.20), here we define the indices

$$\begin{aligned}
S_{r_j} &= \frac{\text{Cov}[f_{r_j}, Y]}{D}, \quad S_{r_j}^s = \frac{D_{r_j}}{D}, \\
S_{r_j}^c &= \frac{\text{Cov}[f_{r_j}, \sum f_{r_k}]}{D},
\end{aligned} \tag{3.29}$$

where  $D = \text{Var}[Y]$ . The Sobol' indices  $S_{r_j}^s$  and  $S_{r_j}^c$  correspond to the structural and correlative contributions [29] to the total index

$$S_{r_j} = S_{r_j}^s + S_{r_j}^c, \tag{3.30}$$

for the index of set of parameters  $r_j$ . These indices satisfy the condition

$$\sum_{j=1}^{2^p-1} S_{r_j} = 1.$$

We approximate indices  $S_{r_j}$  and  $S_{r_j}^s$  using Monte Carlo integration techniques, and simply solve for the index  $S_{r_j}^c$  in (3.30).

As an overall measure of sensitivity for individual parameters  $\theta_i$ , we define the total sensitivity

indices

$$S_{T_i} = S_i + \sum_{\substack{j=1 \\ j \neq i}}^p S_{i j} + \sum_{\substack{1 \leq j < k \leq p \\ j, k \neq i}} S_{i j k} + \cdots + S_{1 \dots p}, \quad i = 1, \dots, p. \quad (3.31)$$

Here, the indices  $S_i, S_{i j}, S_{i j k}, \dots$ , correspond to the component functions

$$f_i(\theta_i), f_{i j}(\theta_i, \theta_j), f_{i j k}(\theta_i, \theta_j, \theta_k), \dots,$$

respectively. It follows that the total indices quantify the complete influence of the parameter  $\theta_i$  on the response, which includes high-order structural interactions, as well as all parameter correlative contributions.

Recall from Section 3.1, that a guide to interpreting the first-order Sobol' sensitivity indices, is to regard indices  $S_i$  greater than  $\frac{100}{p}\%$  as significant, because they have greater than average effect on the variability of the response, in the absence of interactions. Here the indices,  $S_i, S_{i j}, S_{i j k}, \dots$ , may be negative due to parameter correlation. Furthermore, we consider the magnitude of the index as well as the value of the total index  $S_{T_i}$ , when asserting the significance of any negative Sobol' indices. To measure relative parameter importance, we compare and contrast the values of  $S_{T_i}$  for the parameters  $\theta = [\theta_1, \theta_2, \dots, \theta_p]$ .

### 3.2.2 Linearly Parameterized Problems

For linearly parameterized problems

$$Y = f(\Theta) = a_1 \Theta_1 + a_2 \Theta_2 + \cdots + a_p \Theta_p, \quad (3.32)$$

we give an analytic representation of the component functions from (3.29) derived in Section 3.2.1. We start by making the assumption that

$$\Theta \sim \mathcal{N}(\boldsymbol{\mu}, \mathbf{V}),$$

where  $\boldsymbol{\mu} = [\mu_1, \mu_2, \dots, \mu_p]^T$  is a vector of nominal values for  $\Theta$  and  $\mathbf{V}$  is the associated  $p \times p$  covariance matrix. Recall that  $\theta$  are realizations of the random variable  $\Theta$ .

We compute the expected values

$$\begin{aligned}
f_0 &= \mathbb{E}[Y] = \mathbb{E}[a_1\Theta_1 + a_2\Theta_2 + \cdots + a_p\Theta_p] = a_1\mathbb{E}[\Theta_1] + a_2\mathbb{E}[\Theta_2] + \cdots + a_p\mathbb{E}[\Theta_p] \\
&= a_1\mu_1 + \cdots + a_p\mu_p \\
f_i(\theta_i) &= \mathbb{E}[Y|\theta_i] - f_0 \\
&= a_1\mathbb{E}[\Theta_1|\theta_i] + \cdots + a_p\mathbb{E}[\Theta_p|\theta_i] - f_0, \\
f_{ij}(\theta_i, \theta_j) &= \mathbb{E}[Y|\theta_i, \theta_j] - f_i(\theta_i) - f_j(\theta_j) - f_0 \\
&= a_1\mathbb{E}[\Theta_1|\theta_i, \theta_j] + \cdots + a_p\mathbb{E}[\Theta_p|\theta_i, \theta_j] - f_i(\theta_i) - f_j(\theta_j) - f_0, \\
&\vdots
\end{aligned} \tag{3.33}$$

by evaluating the expectation terms  $\mathbb{E}[\Theta_r|\theta_i]$ , for  $r = 1, \dots, p$  in (3.33). For analytic evaluation, we partition  $\Theta$  and  $\mathbf{V}$  as

$$\Theta = [\Theta_1 \ \Theta_2]^T, \ \mathbf{V} = \begin{bmatrix} \mathbf{V}_{11} & \mathbf{V}_{12} \\ \mathbf{V}_{21} & \mathbf{V}_{22} \end{bmatrix}.$$

Here,  $\Theta_1$  is  $r \times 1$ ,  $\Theta_2$  is  $(p-r) \times 1$ , and  $\mathbf{V}$  has components with dimensions

$$\begin{bmatrix} r \times r & r \times (p-r) \\ (p-r) \times r & (p-r) \times (p-r) \end{bmatrix}.$$

The expected value is then

$$\mathbb{E}[\Theta_1, \Theta_2] = \mu_1 + \mathbf{V}_{12}\mathbf{V}_{22}^{-1}(\theta_2 - \mu_2). \tag{3.34}$$

With the expectation terms defined, we now apply these results to the problem (3.32). Assuming a normal distribution, we take

$$\mathbf{V} = \begin{bmatrix} \sigma_1^2 & \tau_{12} & \cdots & \tau_{1p} \\ \tau_{21} & \sigma_2^2 & & \\ \vdots & & \ddots & \\ \tau_{p1} & & & \sigma_p^2 \end{bmatrix}$$

as the covariance matrix. Using the entries in the covariance matrix, we express the component

functions in (3.33) as

$$\begin{aligned}
f_0 &= a_1\mu_1 + \dots + a_p\mu_p \\
f_i(\theta_i) &= a_i\theta_i + \sum_{\substack{j=1 \\ j \neq i}}^p a_j \left( \mu_j + \tau_{\sigma_i\sigma_j} \frac{\sigma_j}{\sigma_i} (\theta_i - \mu_i) \right) - f_0, \quad (i = 1, \dots, p), \\
f_{ij}(\theta_i, \theta_j) &= a_i\theta_i + a_j\theta_j + \sum_{\substack{k=1 \\ k \neq i, j}}^p a_k \left( \mu_k + [\tau_{ki} \ \tau_{kj}] \begin{bmatrix} \sigma_i^2 & \tau_{ij} \\ \tau_{ji} & \sigma_j^2 \end{bmatrix}^{-1} \begin{bmatrix} \theta_i - \mu_i \\ \theta_j - \mu_j \end{bmatrix} \right) - f_i - f_j - f_0, \\
&\vdots \\
f_{1\dots p}(\theta_1, \dots, \theta_p) &= f(\theta) - \dots - \sum_{1 \leq i < j < k < \ell \leq p} f_{ijkl} - \sum_{1 \leq i < j < k \leq p} f_{ijk} - \sum_{1 \leq i < j \leq p} f_{ij} - \sum_{i=1}^p f_i - f_0.
\end{aligned} \tag{3.35}$$

Here  $\tau_{ij}$  is the covariance between  $\theta_i$  and  $\theta_j$ ,  $\sigma_i^2$  is the variance for  $\theta_i$ , and  $\tau_{\sigma_i\sigma_j} = \frac{\tau_{ij}}{(\sigma_i\sigma_j)}$  is the Pearson correlation. The theory given here is employed in the ferroelectric phase-field single domain model analysis of Chapter 4 to construct Sobol' decomposition component functions analytically.

### 3.2.3 Numerical Basis Functions Expansion

Whereas the analytical solution for the component functions in (3.29), introduced and detailed in Section 3.2.2, is applicable only for linearly parameterized problems, here we discuss a general solution technique for nonlinearly parameterized problems

$$Y = f(\Theta).$$

The technique is similar in nature to the one based on the work by Li [29], utilizing cubic B-splines [12, 41],  $B_k(\theta)$ ,  $k = k = -1, \dots, m+1$ , and approximating the Sobol' decomposition terms in  $Y = f(\Theta)$ . We employ these basis functions in the component functions (3.13) approximations

$$\begin{aligned}
f_i(\theta_i) &\approx \sum_{r=-1}^{m+1} \alpha_r^i B_r(\theta_i), \\
f_{ij}(\theta_i, \theta_j) &\approx \sum_{u=-1}^{m+1} \sum_{q=-1}^{m+1} \beta_{uq}^{ij} B_u(\theta_i) B_q(\theta_j), \\
f_{ijk}(\theta_i, \theta_j, \theta_k) &\approx \sum_{u=-1}^{m+1} \sum_{q=-1}^{m+1} \sum_{v=-1}^{m+1} \gamma_{uqv}^{ijk} B_u(\theta_i) B_q(\theta_j) B_v(\theta_k).
\end{aligned} \tag{3.36}$$

Here the coefficients  $\alpha_r^i, \beta_{uq}^{ij}$  and  $\gamma_{uqv}^{ijk}$  are determined via least squares regression. Next, we consider the first-, second- and third-order component functions approximations

$$\begin{aligned}
f_i(\theta_i^s) &\approx Y^s - f_0, \\
f_{ij}(\theta_i^s, \theta_j^s) &\approx Y^s - f_0 - f_i(\theta_i^s) - f_j(\theta_j^s), \\
f_{ijk}(\theta_i^s, \theta_j^s, \theta_k^s) &\approx Y^s - f_0 - f_i(\theta_i^s) - f_j(\theta_j^s) \\
&\quad - f_k(\theta_k^s) - f_{ij}(\theta_i^s, \theta_j^s) - f_{ik}(\theta_i^s, \theta_k^s) - f_{jk}(\theta_j^s, \theta_k^s),
\end{aligned} \tag{3.37}$$

where we employ  $Y^s = f(\theta^s)$  as an unbiased estimator for  $\mathbb{E}[Y|\theta_{r_n}^s]$ . The samples  $\theta^s$  represent independent realizations from the underlying distribution for  $\theta$ . To determine a numerical approximation for each specific component function, we then substitute the expression (3.36) into (3.37), to obtain

$$\begin{aligned}
\sum_{r=-1}^{m+1} \alpha_r^i B_r(\theta_i^s) &\approx Y^s - f_0, \\
\sum_{u=-1}^{m+1} \sum_{q=-1}^{m+1} \beta_{uq}^{ij} B_u(\theta_i^s) B_q(\theta_j^s) &\approx Y^s - f_0 - f_i(\theta_i^s) - f_j(\theta_j^s), \\
\sum_{u=-1}^{m+1} \sum_{q=-1}^{m+1} \sum_{v=-1}^{m+1} \gamma_{uqv}^{ijk} B_u(\theta_i^s) B_q(\theta_j^s) B_v(\theta_k^s) \\
&\approx Y^s - f_0 - f_i(\theta_i^s) - f_j(\theta_j^s) - f_k(\theta_k^s) - f_{ij}(\theta_i^s, \theta_j^s) - f_{ik}(\theta_i^s, \theta_k^s) - f_{jk}(\theta_j^s, \theta_k^s).
\end{aligned} \tag{3.38}$$

The coefficients in (3.38) are solved for in a stepwise least squares regression fashion. For the first-order component functions, we determine the coefficients  $\alpha^i = [\alpha_{-1}^i, \dots, \alpha_{m+1}^i]^T$ , by minimizing the cost functional

$$\begin{aligned}
J_i(\alpha^i) &= \sum_{s=1}^K (Y^s - f_0 - f_i(\theta_i^s))^2 \\
&= \sum_{s=1}^K \left( Y^s - f_0 - \sum_{r=-1}^{m+1} \alpha_r^i B_r(\theta_i^s) \right)^2 \\
&= (\mathbf{Y}^i - \mathbf{A}^{\{i\}} \alpha^i)^T (\mathbf{Y}^i - \mathbf{A}^{\{i\}} \alpha^i) \\
&= \|\mathbf{Y}^i - \mathbf{A}^{\{i\}} \alpha^i\|_2^2,
\end{aligned} \tag{3.39}$$



for  $i = 1, \dots, p$ . We define the additional terms in (3.39) as

$$\mathbf{A}^{\{i\}} = \begin{bmatrix} B_{-1}(\theta_i^1) & B_0(\theta_i^1) & \cdots & B_{m+1}(\theta_i^1) \\ \vdots & \vdots & & \vdots \\ B_{-1}(\theta_i^K) & B_0(\theta_i^K) & \cdots & B_{m+1}(\theta_i^K) \end{bmatrix},$$

$$\mathbf{Y}^i = \begin{bmatrix} Y^1 \\ \vdots \\ Y^K \end{bmatrix} - f_0 \mathbf{1},$$

where  $K \equiv$  number of  $\theta$  samples and  $\mathbf{1} = [1, \dots, 1]^T$ . It follows that

$$\alpha^{i*} = \left( \mathbf{A}^{\{i\}T} \mathbf{A}^{\{i\}} \right)^{-1} \mathbf{A}^{\{i\}T} \mathbf{Y}^i \quad (3.40)$$

is a least squares solution to the sum of squares function (3.39).

Likewise, for the higher-order component functions, we minimize the cost functions

$$J_{ij}(\beta^{ij}) = \|\mathbf{Y}^{ij} - \mathbf{A}^{\{ij\}} \beta^{ij}\|_2^2,$$

$$J_{ijk}(\gamma^{ijk}) = \|\mathbf{Y}^{ijk} - \mathbf{A}^{ijk} \gamma^{ijk}\|_2^2,$$

where

$$\beta^{ij} = [\beta_{-1,-1}^{ij}, \dots, \beta_{m+1,-1}^{ij}, \beta_{-1,0}^{ij}, \dots, \beta_{uq}^{ij}, \dots, \beta_{m+1,m+1}^{ij}]^T$$

and

$$\gamma^{ijk} = [\gamma_{-1,-1,-1}^{ijk}, \dots, \gamma_{uqv}^{ijk}, \dots, \gamma_{m+1,m+1,m+1}^{ijk}]^T.$$

The solution of the coefficients in (3.38), is followed by random sampling from the underlying parameter distribution to approximate the integrals in the Sobol' sensitivity indices (3.29).

We implement the numerical method given here and compare it with the analytical method given in Section 3.2.2 for the ferroelectric single domain phase-field continuum model analysis of Chapter 4.

### 3.3 Subset Selection using the Singular Value Decomposition

An alternative method for verifying the results of the global sensitivity analysis is determining identifiable parameters via singular value decomposition-based algorithms. As we will detail, the first method requires a linearly parameterized model of the form

$$Y = \mathbf{A}\theta,$$

where  $\mathbf{A}$  is the design matrix and  $\theta$  are the parameters of interest. The second method uses local sensitivity in ascertaining the most identifiable parameters with respect to nominal parameter values. We extend this to consider global sensitivity by sampling from the underlying parameter distributions to the entries in sensitivity matrices. We give the two methods in Sections 3.3.1 and 3.3.2.

### 3.3.1 SVD Subset Selection for Linearly Parameterized Models

For problems where the model is linearly parameterized, Golub's algorithm for subset selection gives a least squares solution to a reduced system of parameters [15]. The algorithm uses the singular value decomposition of the design matrix  $\mathbf{A}$ , and determines a rank estimate  $\tilde{r}$  for  $r$  such that the parameter dimension is reduced. An associated QR decomposition is then used to determine an appropriate permutation matrix in selecting the significant columns of  $\mathbf{A}$ . We illustrate the full procedure in Algorithm 3.3.1. Note that the algorithm relies on the assumption that the smallest singular value of the matrix  $\mathbf{A}$  is small enough such that we obtain a rank approximation  $\tilde{r}$ . Typically, we invoke the threshold  $\epsilon = 10^{-8}$ , or the square root of machine epsilon, to appropriately define 'small enough'.

### 3.3.2 Fisher Information Matrix Analysis

Consider the function  $f(P_i, \theta)$  and its first order Taylor series approximation

$$f(P_i, \theta) \approx f(P_i, \theta^*) + \nabla_{\theta} f(P_i, \theta^*) \Delta \theta, \quad (3.41)$$

where  $P_i$  is some independent variable, and  $\theta^*$  is a nominal parameter value. Let  $Y_i = f(P_i, \theta^*) + \varepsilon_i$ ,

---

**Algorithm 3.3.1:** Golub's algorithm for subset selection using the singular value decomposition (SVD) for problems of the type  $\mathbf{Ax} = \mathbf{b}$  [15].

---

- (1) Construct the SVD of  $\mathbf{A} \in \mathbb{R}^{m \times p}$ , such that  $\mathbf{A} = \mathbf{U}\Sigma\mathbf{V}^T$ , where  $\Sigma = \text{diag}(\sigma_1, \sigma_2, \dots, \sigma_p)$  is the diagonal matrix of singular values of  $\mathbf{A}$ .
  - (2) Determine a rank estimate  $\tilde{r} \leq r = \text{rank}(\mathbf{A})$ , by filtering the small singular values of  $\mathbf{A}$ .
  - (3) Apply the QR factorization with column pivoting to  $\mathbf{V}(:, 1 : \tilde{r})^T$  such that  $\mathbf{V}(:, 1 : \tilde{r})^T \mathbf{P} = \mathbf{QR}$ , where  $\mathbf{P}$  is a permutation matrix and  $\mathbf{R}$  is upper triangular.
  - (4) Set  $\mathbf{AP} = [\mathbf{B}_1, \mathbf{B}_2]$ , where  $\mathbf{B}_1 \in \mathbb{R}^{m \times \tilde{r}}$  and  $\mathbf{B}_2 \in \mathbb{R}^{m \times (p - \tilde{r})}$ .
  - (5) Determine the least squares solution such that  $\min_{\mathbf{z} \in \mathbb{R}^{\tilde{r}}} \|\mathbf{B}_1 \mathbf{z} - \mathbf{b}\|_2$  is minimized.
-

where  $\varepsilon_i \sim \mathcal{N}(0, \sigma^2)$  is an independently and identically distributed random error, and let  $f_i(\theta^*) = f(P_i, \theta^*)$ . Then, we have the approximation  $Y_i \approx f(P_i, \theta)$ , and the cost function

$$J(\theta) = \frac{1}{N} \sum_{i=1}^N [Y_i - f(P_i, \theta^*)]^2. \quad (3.42)$$

Substituting (3.41) into (3.42), yields

$$\begin{aligned} J(\theta) &\approx \frac{1}{N} \sum_{i=1}^N [\nabla_{\theta} f(P_i, \theta^*) \cdot \Delta\theta]^2 \\ &= \frac{1}{N} (\mathbf{S} \Delta\theta)^T (\mathbf{S} \Delta\theta), \end{aligned} \quad (3.43)$$

where  $\mathbf{S}$  is the sensitivity matrix

$$\mathbf{S} = \begin{bmatrix} \frac{\partial f_1}{\partial \theta_1}(\theta^*) & \frac{\partial f_1}{\partial \theta_2}(\theta^*) & \cdots & \frac{\partial f_1}{\partial \theta_p}(\theta^*) \\ \frac{\partial f_2}{\partial \theta_1}(\theta^*) & \frac{\partial f_2}{\partial \theta_2}(\theta^*) & \cdots & \frac{\partial f_2}{\partial \theta_p}(\theta^*) \\ \vdots & \vdots & & \vdots \\ \frac{\partial f_N}{\partial \theta_1}(\theta^*) & \frac{\partial f_N}{\partial \theta_2}(\theta^*) & \cdots & \frac{\partial f_N}{\partial \theta_p}(\theta^*) \end{bmatrix}. \quad (3.44)$$

We can then formulate the cost function (3.43) as

$$J(\theta^* + \Delta\theta) \approx \frac{1}{N} \Delta\theta^T \mathbf{S}^T \mathbf{S} \Delta\theta. \quad (3.45)$$

If we take  $\Delta\theta$  to be an eigenvector of  $\mathbf{S}^T \mathbf{S}$ , then for a corresponding eigenvalue  $\lambda$ ,

$$\mathbf{S}^T \mathbf{S} \Delta\theta = \lambda \Delta\theta \implies J(\theta^* + \Delta\theta) \approx \frac{\lambda}{N} \|\Delta\theta\|_2^2.$$

When the eigenvalue  $\lambda \approx 0$ , its perturbations defined by the eigenvector  $\Delta\theta$ , yield negligible changes in the cost function,

$$J(\theta^* + \Delta\theta) \approx 0,$$

such that parameters in the direction of  $\Delta\theta$  are locally unidentifiable.

We define the matrix  $\mathbf{F} = \mathbf{S}^T \mathbf{S}$  as the Fisher information matrix. There are several algorithms which employ this methodology in determining locally identifiable parameters, such as the ones in Brun et al. [3], Burth et al. [4], Contron-Arias et al. [10], and Quaiser and Monnigmann [42]. To implement this methodology, we use Algorithm 3.3.2, as motivated by [42].

---

**Algorithm 3.3.2:** Method for determining locally identifiable parameters from the Fisher information matrix, based on [42].

---

- (0) Set  $\eta = p$ , where  $p$  is the number of parameters in the model. Next, compute construct the corresponding sensitivity matrix  $\mathbf{S}$  following relation (3.44). The variable  $\eta$  will change with the successive iterations of the algorithm.
- (1) Construct the Fisher information matrix  $\mathbf{F} = \mathbf{S}^T \mathbf{S}$  and determine its eigenvalues. Order the eigenvalue magnitudes as

$$|\lambda_1| \leq |\lambda_2| \leq \dots \leq |\lambda_\eta|.$$

- (2) If  $|\lambda_1| > \epsilon$ , where  $\epsilon$  is some prescribed threshold value, stop. We take all the parameters to be identifiable. In further implementations of the algorithm, we will take the threshold value  $\epsilon = 10^{-8}$ .
  - (3) If  $|\lambda_1| < \epsilon$ , then one of the parameters is not locally identifiable. Proceed as follows.
  - (4) Identify the component with the largest magnitude in the eigenvector  $\Delta\theta_1$  associated with  $\lambda_1$ . As motivated by (3.45), this component corresponds to the least identifiable parameter.
  - (5) Remove the column in  $\mathbf{S}$  corresponding to the component identified in Step 4 and set  $\eta = \eta - 1$ . Repeat Step 1 until all locally unidentifiable model parameters have been determined.
- 

### 3.3.3 Random Sampling of the Sensitivity Matrix

For a measure of quasi-global sensitivity, we expand the derived methodology for Algorithm 3.3.2, to include samples across the admissible parameter space. This is analogous to the elementary effects (3.8), given in Section 3.1.1, in that the entries to the sensitivity matrix are taken to be sampled derivative means. Therefore we define each final sensitivity matrix entry  $S_{ij}^*$  to be

$$S_{ij}^* = \frac{1}{r} \sum_{k=1}^r S_{ij}^k, \quad (3.46)$$

where

$$S_{ij}^k = \frac{\partial f_i}{\partial \theta_j}(\theta^k).$$

Here,  $k$  represents the  $k^{th}$  evaluation of the sensitivity matrix for a sample  $\theta^k$ . Note that the parameters  $\theta$  are sampled from the underlying parameter distributions.

### 3.4 Active Subspace Selection

Active subspace methods provide an alternative appealing approach that identifies important directions in the admissible parameter space that most strongly affect the output response. We typically employ these methods when models contain a high number of parameters and/or parameter subset selection techniques are infeasible due to high computational cost. Active subspaces may be used to derive response surfaces, that approximate the original output, and can subsequently be employed for model calibration. They can also be used to develop activity scores, to rank the relative influence of model inputs, as an alternative to classical global sensitivity analysis techniques.

When constructing an active subspace, we must approximate gradients, which quantify changes in the output with respect to parameter perturbations. When the parameters differ by large orders of magnitude, classical derivative approximations may yield incorrect gradient results. This motivates the normalized gradient evaluations described in Section 3.4.1. We use these normalized gradient evaluations to construct the active subspace detailed in Section 3.4.2. In Section 3.4.3, we detail techniques for verifying the dimension of the active subspace. Lastly, in Section 3.4.4, we detail the construction of activity scores.

#### 3.4.1 Normalized Gradient Evaluations

The active subspace method detailed in Section 3.4.2 requires gradient approximations for the model  $y = f(\theta)$ . When the parameters  $\theta$  vary vastly in magnitude, partial derivative approximations, such as

$$\frac{\partial}{\partial \theta_i} f(\theta) \approx \frac{f(\theta + \Delta \mathbf{e}_i) - f(\theta)}{\Delta},$$

where  $\Delta$  is a suitably small step size, may yield inaccurate results. Here,  $\mathbf{e}_i$  is the  $i^{\text{th}}$  canonical vector containing all entries equal to 0, except for the  $i^{\text{th}}$  entry which is equal to 1.

In some cases we may observe differences up to 20 orders of magnitude in parameter samples. To ensure that inputs or parameters with large or small values do not dominate the gradient evaluations, we must normalize our inputs. We consider two cases of scaling maps for normalizing our parameters. The first is the assumption that the parameters are uniformly distributed, whereas the second is the assumption that the parameters are normally distributed.

#### Scaling Maps

For the first scaling map, we consider the parameters  $\theta$  to be uniformly distributed such that

$$\Theta_i \sim \mathcal{U}(\theta_i^{\text{nom}} - \delta|\theta_i^{\text{nom}}|, \theta_i^{\text{nom}} + \delta|\theta_i^{\text{nom}}|). \quad (3.47)$$

Here,  $\theta_i^{\text{nom}}$ ,  $i = 1, \dots, p$ , represents the nominal values of the parameters  $\theta$ . For active subspace

construction, a typically chosen value for  $\delta$  is 0.10. To avoid issues due to differences in parameter values, we transform the distributions (3.47) to  $\mathcal{U}(0, 1)$ . The transformation normalizes all inputs, removes units and ensures that parameters containing relatively large or small values do not affect the analysis disproportionately. To transform back to the physical space for model evaluations, we use the mapping

$$g_U(\mathbf{x}) = \text{diag}(\theta_u - \theta_\ell)\mathbf{x} + \theta_\ell, \quad (3.48)$$

where  $\mathbf{x}$  is a  $p$ -vector with values between 0 and 1, and  $\theta_\ell$  and  $\theta_u$ , respectively, are the lower and upper bound vectors of the parameters  $\theta$ . For the above scenario, these vectors are

$$\theta_\ell = \theta^{nom} - \delta|\theta^{nom}| \text{ and } \theta_u = \theta^{nom} + \delta|\theta^{nom}|,$$

where  $\theta^{nom}$  are the nominal values for  $\theta$ .

Secondly, we consider the case when the parameters are normally distributed, such that

$$\Theta \sim \mathcal{N}(\theta^{nom}, \mathbf{V}), \quad (3.49)$$

where  $\mathbf{V}$  is the covariance matrix

$$\mathbf{V} = \begin{bmatrix} \text{var}(\Theta_1) & \text{cov}(\Theta_1, \Theta_2) & \cdots & \text{cov}(\Theta_1, \Theta_p) \\ \text{cov}(\Theta_2, \Theta_1) & \text{var}(\Theta_2) & \cdots & \\ \vdots & \vdots & \ddots & \\ \text{cov}(\Theta_p, \Theta_1) & & & \text{var}(\Theta_p) \end{bmatrix}.$$

We again normalize all inputs to avoid discrepancies in the analysis, as a result of parameters with relatively large or small values. We employ a Cholesky decomposition of  $\mathbf{V}$ , where

$$\mathbf{V} = \mathbf{A}\mathbf{A}^T.$$

Here, the mapping to the natural input space for model evaluations is

$$g_N(\mathbf{x}) = \theta^{nom} + \mathbf{A}\mathbf{x}, \quad (3.50)$$

where  $\mathbf{x}$  are generated from the standard normal distribution  $\mathcal{N}(\mathbf{0}, \mathbf{1})$ .

### Normalized Gradient Estimates

Here, we define the normalized derivative approximation to be used in the construction of the active subspace. This derivative has the normalized parameters as inputs, with evaluations in the physical space as outputs.

We define the function  $h$  as a composition of functions. Let  $\mathbb{Q} \subseteq \mathbb{R}$ ,  $\theta \in \mathbb{Q}$ ,  $\mathbf{x} \in [0, 1]$ , and consider the mappings

$$\begin{aligned} f &: \mathbb{Q} \rightarrow \mathbb{R}, \\ g &: [0, 1] \rightarrow \mathbb{Q}, \\ h &: [0, 1] \rightarrow \mathbb{R}, \end{aligned} \tag{3.51}$$

such that

$$h(\mathbf{x}) = (f \circ g)(\mathbf{x}) = f(g(\mathbf{x})). \tag{3.52}$$

We then obtain the relation

$$\begin{aligned} h'(x) &\approx \frac{h(x + \Delta) - h(x)}{\Delta} \\ &= \frac{f(g(x + \Delta)) - f(g(x))}{\Delta} \\ &\approx \frac{f(g(x) + \Delta g'(x)) - f(g(x))}{\Delta} \\ &\approx \frac{f(g(x)) + \Delta g'(x) f'(g(x)) - f(g(x))}{\Delta} \\ &= f'(g(x)) g'(x) \end{aligned}$$

where  $0 < \Delta \ll 1$ . This is equivalent to the chain rule derivative for composition (3.52). We implement this derivative in the gradient evaluations required for the determination of active subspaces to avoid inaccuracies due to varying units of magnitude. When  $p > 1$ , we approximate the required partial derivatives in the finite difference algorithms as

$$\frac{\partial}{\partial x_i} h(\mathbf{x}) \approx \frac{h(\mathbf{x} + \Delta \mathbf{e}_i) - h(\mathbf{x})}{\Delta}, \quad i = 1, \dots, p,$$

where  $\mathbf{e}_i$  is the  $i^{\text{th}}$  canonical vector.

To implement gradient evaluations in the uniform normalized space, we let  $\mathbf{T}_U = \text{diag}(\theta_u - \theta_\ell)$ , and define the function

$$h_U(\mathbf{x}) = f(g_U(\mathbf{x})) = f(\mathbf{T}_U \mathbf{x} + \theta_\ell). \tag{3.53}$$

Using (3.53), we obtain the finite difference partial derivative approximation

$$\begin{aligned}\frac{h_U(\mathbf{x} + \Delta) - h_U(\mathbf{x})}{\Delta} &= \frac{f(g_U(\mathbf{x} + \Delta)) - f(g_U(\mathbf{x}))}{\Delta} \\ &= \frac{f(\mathbf{T}_U(\mathbf{x} + \Delta) + \theta_\ell) - f(\mathbf{T}_U\mathbf{x} + \theta_\ell)}{\Delta}\end{aligned}\quad (3.54)$$

Similarly, when the parameters are normally distributed, we define

$$h_N(\mathbf{x}) = f(g_N(\mathbf{x})) = f(\mathbf{A}\mathbf{x} + \theta^{nom}), \quad (3.55)$$

such that the normalized gradient is

$$\begin{aligned}\frac{h_N(\mathbf{x} + \Delta\mathbf{e}_i) - h_N(\mathbf{x})}{\Delta} &= \frac{f(g_N(\mathbf{x} + \Delta\mathbf{e}_i)) - g_N(\mathbf{x})}{\Delta} \\ &= \frac{f(\mathbf{A}(\mathbf{x} + \Delta\mathbf{e}_i) + \theta^{nom}) - f(\mathbf{A}\mathbf{x} + \theta^{nom})}{\Delta}.\end{aligned}\quad (3.56)$$

### 3.4.2 Active Subspace Construction

We refer to parameter subspace selection methods as *active subspace* methods since *active variables* are determined as weighted linear combinations of the parameters indicating directions of strongest variability in the parameter space. Those directions are separated from ones in which the model output is relatively flat, yielding *inactive variables*.

Consider the function

$$Y = f(\Theta)$$

where  $\Theta = [\Theta_1, \Theta_2, \dots, \Theta_p]$  is a set of random variables with an associated distribution  $\rho(\Theta)$ . Then, we define the matrix

$$\mathbf{C} = \mathbb{E}[(\nabla_\theta f)(\nabla_\theta f)^T], \quad (3.57)$$

which is positive semidefinite by construction. Thus, it has the eigenvalue decomposition

$$\mathbf{C} = \mathbf{W}\mathbf{\Lambda}\mathbf{W}^T.$$

Here,  $\mathbf{\Lambda} = \text{diag}(\lambda_1, \lambda_2, \dots, \lambda_p)$ ,  $\lambda_1 \geq \lambda_2 \geq \dots \geq \lambda_p \geq 0$ . If there exists a significant gap in the eigenvalue spectrum, we obtain the partitions

$$\mathbf{W} = [\mathbf{W}_1 \mathbf{W}_2], \quad \mathbf{\Lambda} = \begin{bmatrix} \mathbf{\Lambda}_1 & \\ & \mathbf{\Lambda}_2 \end{bmatrix}, \quad \mathbf{\Lambda}_1 = \text{diag}(\lambda_1, \dots, \lambda_m), \quad m < p.$$



Based on the significant gap, we define the new rotated coordinate variables

$$\mathbf{y} = \mathbf{W}_1^T \boldsymbol{\theta}, \mathbf{z} = \mathbf{W}_2^T \boldsymbol{\theta},$$

where  $\mathbf{y} \in \mathbb{R}^m$  and  $\mathbf{z} \in \mathbb{R}^{p-m}$ . Here, the output  $f$  varies more prominently due to variability in directions dictated by  $\mathbf{y}$ , than in the directions dictated by  $\mathbf{z}$ , defining the *active* and *inactive* subspaces [8].

The construction of the matrix  $\mathbf{C}$  (3.57) may require the computation of high dimensional integrals, which may be prohibitive in practice. Therefore, we approximate the gradient matrix

$$\mathbf{G} = \frac{1}{\sqrt{M}} [\nabla_{\theta} f_1 \quad \nabla_{\theta} f_2 \quad \cdots \quad \nabla_{\theta} f_M] \quad (3.58)$$

using Monte Carlo sampling. Here,  $\mathbf{G}$  is composed of  $M$  gradient, or approximate gradient evaluations at values in the original input space, as motivated by Bang [1] and Constantine [8]. We extract an input active subspace basis by employing the singular value decomposition (SVD) of the matrix  $\mathbf{G}$ . As such, the active subspace basis is represented by a subset of singular vectors contained in the matrix  $\mathbf{W}$ , in

$$\mathbf{G} = \mathbf{W} \boldsymbol{\Sigma} \mathbf{V}^T, \quad (3.59)$$

where  $\boldsymbol{\Sigma}$  is the diagonal matrix containing the squared roots of the eigenvalues of  $\mathbf{C}$ . As shown by Russi [44], this active subspace computation methodology is equivalent to the one employed by the formation of the matrix  $\mathbf{C}$ .

## Implementation

The construction of the matrix  $\mathbf{G}$  (3.58) usually necessitates gradient approximations since an analytic gradient is typically not available for complex systems. This motivates the consideration of finite-difference algorithms to construct  $\mathbf{G}$  and determine the active subspace. Depending on the parameter distribution, we use either (3.54) or (3.56) to evaluate normalized derivative approximations. The main idea is to select normalized initial vectors  $\mathbf{x}^j \in \mathbb{R}^p$ ,  $j = 1, \dots, M$ , sampled from the corresponding probability density  $\rho(\mathbf{x})$ . Following the maps for the uniform and normal density distributions defined in (3.47)-(3.49), we then construct a set of derivative approximations termed elementary effects,

$$d_i(\mathbf{x}^j) = \frac{h(x_1^j, \dots, x_{i-1}^j, x_i^j + \Delta, x_{i+1}^j, \dots, x_p^j) - h(\mathbf{x}^j)}{\Delta} = \frac{h(\mathbf{x}^j + \Delta \cdot \mathbf{e}_i) - h(\mathbf{x}^j)}{\Delta} \quad (3.60)$$

similar to relation (3.8), with the distinction of the map  $h(\mathbf{x})$  and the normalized parameters  $\mathbf{x}$ . Here,  $\Delta$  is a given step size, and  $i$  represents an index for the  $i^{th}$  parameter and  $j$  for the  $j^{th}$

---

**Algorithm 3.4.1:** Finite-difference method for gradient matrix approximation [28].

---

(0) Identify the number of desired columns  $M$ , appropriate step size  $\Delta$ , and probability density  $\rho(\mathbf{x})$ . Use the model function  $h_U(\mathbf{x})$  (3.54) or  $h_N(\mathbf{x})$  (3.56) depending on the probability density  $\rho(\mathbf{x})$ .

**for**  $j = 1, \dots, M$

(1) Construct the row vector  $\mathbf{D}_{1 \times p}$  with randomly chosen entries  $\pm\Delta$ , where  $\Delta$  is the step size.

(2) Select  $\mathbf{x}^j$  from the probability density  $\rho(\mathbf{x})$ . In our case this is the uniform or normal distribution. Evaluate the model function at the sampled value along with the elementary effect as follows.

**for**  $i = 1, \dots, p$

$$d_i = \frac{h(\mathbf{x}_i^j + \mathbf{D}(i) \cdot \mathbf{e}_i) - h(\mathbf{x}^j)}{\mathbf{D}(i)}, \text{ where } \mathbf{e}_i \text{ is the } i^{\text{th}} \text{ standard basis vector.}$$

**end**

(3) Let  $\hat{\mathbf{G}}(:, j) = \mathbf{d}$ , where  $\hat{\mathbf{G}}$  is the gradient matrix approximation.

**end**

---

sample point drawn from  $\rho(\mathbf{x})$ . We use this method, as illustrated in Algorithm 3.4.1, to construct the columns of the gradient matrix (3.58) for the active subspace determination. Following an SVD of the gradient matrix, the first  $n$  singular vectors represent the basis vectors for an  $n$ -dimensional active subspace. To reduce the number of model evaluations, the gradient-free active subspace construction methods, detailed in [28], may also be used. In the next section, we visit the techniques employed in the determination of the dimension of the active subspace.

### 3.4.3 Finding the Dimension of the Active Subspace

To determine the dimension of the active subspace, we consider several criteria. The first and most straightforward criteria is to observe large gaps in the singular value spectrum upon a SVD of the gradient matrix (3.58). Typically, a large gap consisting of at least an order of magnitude is observed after the first or second singular value, thereby indicating a one- or two-dimensional active subspace, respectively [8]. Gap observations require a more quantitative verification step, which motivates the following methods for dimension selection.

A second criteria for determining the dimension of the active subspace, is error-based dimension selection. Here, we consider an approach based on an algorithm from [19]. The user selects an error tolerance  $\varepsilon_{tol}$  which is compared to an upper-error bound. The error tolerance is selected based on factors such as model computational time and resources available. When the error upper bound has decreased below the user-defined error tolerance, the algorithm is terminated and an appropriate

---

**Algorithm 3.4.2:** Error-based dimension selection algorithm based on [19].

---

(1) For the gradient matrix  $\mathbf{G}$  (3.58), compute the SVD  $\mathbf{G} = \mathbf{W}\Sigma\mathbf{V}^T$ .

**for**  $j = 1 : k - 1$

(a) Sample a set of  $p$  standard Gaussian vectors  $\{\mathbf{w}^1, \dots, \mathbf{w}^p\}$ .

(b) Let  $\hat{\mathbf{W}}_{m \times j}$  be the first  $j$  columns of  $\mathbf{W}$ .

(c) Define the upper bound error as  $\varepsilon_{upp}^j = 10\sqrt{2/\pi} \max_{i=1, \dots, p} \|(\mathbf{I} - \hat{\mathbf{W}}\hat{\mathbf{W}}^T)\mathbf{G}\mathbf{w}^i\|$ .

**end**

(2) When  $\varepsilon_{upp}^j < \varepsilon_{tol}$ , take  $j$  to be the active subspace dimension. If a value less than the error tolerance is not achieved, compute  $\mathbf{G}$  with more columns and repeat Step 1.

---

active subspace dimension is determined. As noted by Lewis et al. [28], this method retains the largest number of dimensions for response surface construction in the active subspace. We illustrate the outline of the algorithm in Algorithm 3.4.2.

The next criteria that we use to verify the active subspace dimension is principal component analysis (PCA). In this analysis, deviations from the sample mean of the gradient matrix  $\mathbf{G}$  are analyzed and a test statistic is developed, based on a covariance matrix  $\mathbf{C}$ , to assess the dimension of the active subspace [23]. We detail the outline of the procedure in Algorithm 3.4.3.

Lastly we construct a response surface as a verification step to the identification of the active subspace. In principle, the response surface should be aligned in the direction of strongest variability in the parameter space, while accurately fitting the model response. We use a comparison of mean relative errors (MRE) for several possible active subspace dimensions. We denote the actual model response at sample  $s$  as  $A_s$ , while we denote the response surface by  $F_s$ . Then, we define the mean relative error by

$$MRE = \frac{1}{N} \sum_{s=1}^N \left| \frac{A_s - F_s}{A_s} \right|,$$

where  $N$  is the number of realizations. The dimension of the active subspace is typically indicated when the reduction in the MRE is less than one order of magnitude, as the dimension is increased. We illustrate the procedure for constructing the response surface in Algorithm 3.4.4.

### 3.4.4 Activity Scores

Here, we present an alternative metric for global sensitivity analysis, based on active subspaces. This sensitivity metric ranks parameter influence based on the derived singular values and vectors used to define the active variables.

---

**Algorithm 3.4.3:** Principal component analysis (PCA) active subspace dimension selection based on [23].

---

- (1) For the gradient matrix  $\mathbf{G}$  (3.58), compute the sample mean  $u(j) = \frac{1}{m} \sum_{i=1}^m \mathbf{G}_{i,j}$ . Let  $\mathbf{1}$  be an  $m \times 1$  column vector of ones.
- (2) Calculate the deviations from the mean, employing the column vector of sample means  $\mathbf{u}$ , by

$$\mathbf{B} = \mathbf{G} - \mathbf{1}\mathbf{u}^T.$$

- (3) Compute the covariance matrix  $\mathbf{C}$  by calculating the outer product of  $\mathbf{B}$  with itself,

$$\mathbf{C} = \frac{1}{m-1} \mathbf{B}^T \mathbf{B}.$$

- (4) Compute the eigendecomposition of  $\mathbf{C}$ , such that

$$\mathbf{C} = \mathbf{V}\mathbf{D}\mathbf{V}^{-1},$$

where  $\mathbf{D}$  is the diagonal matrix which contains the eigenvalues of  $\mathbf{C}$ .

- (5) For each subset of  $j$  eigenvectors, compute the cumulative ‘energy’ content for each subset of  $j$  eigenvectors, to quantify the variance, which is contained in the set

$$g(j) = \sum_{k=1}^j \mathbf{D}(k, k), \quad \text{for } j = 1, \dots, m.$$

- (6) For some user-defined percentage  $100t^*$ , the active subspace dimension is the smallest  $j$  such that

$$\frac{g(j)}{g(n)} \geq t^*.$$


---

As detailed in [8], the activity scores are based on the formula

$$a_i = a_i(m) = \sum_{j=1}^m \lambda_j w_{i,j}^2, \quad i = 1, \dots, p, \tag{3.61}$$

where  $m$  is the dimension of the active subspace,  $\lambda_j$ ,  $j = 1, \dots, m$  correspond to the  $m$  eigenvalues in the active subspace, whereas  $w_{i,j}$  are the eigenvector entries. We use the activity scores to compare with the parameter subset selection methods derived in Section 3.3.2.

---

**Algorithm 3.4.4:** Algorithm for constructing response surface based on active subspace.

---

- (0) Sample the training input values  $\mathbf{x}_i$  with respect to its probability density function and construct corresponding responses  $q_i = g(\mathbf{x}_i)$ .
  - (1) Project the sampled values  $\mathbf{x}_i$  onto the active subspace by using the transformation  $\mathbf{y} = \mathbf{W}_1^T \mathbf{x}_i$ .
  - (2) Using regression analysis construct a response surface  $r(\mathbf{y})$ , using  $q_i$ , such that  $q_i \approx r(\mathbf{y}_i)$ .
  - (3) Verify the response surface by approximating the original function  $g(\mathbf{x}) \approx r(\mathbf{W}_1^T \mathbf{x})$ .
- 

### 3.5 Bayesian Inference

In Bayesian inference, we consider probabilities as quantifying the likelihood of an event occurring given prior knowledge and available information. Hence, as more information is acquired about a particular system or phenomenon of interest, Bayesian probabilities are updated. As a counterpart to frequentist statistical analysis, where probabilities are characterized as fixed relative frequency values with which events occur given a large number of performed experiments, Bayesian probabilities are not fixed values and change as more information is obtained.

As such, model parameters in Bayesian statistical analysis are treated as random variables with associated probability densities. The distributions characterize the information known about the parameters, and this involves the construction or approximation of probability density functions (PDFs). Due to the reliance of probabilities on prior information and current observations, Bayes' rule

$$P(A|B) = \frac{P(B|A)P(A)}{P(B)} \quad (3.62)$$

constitutes the natural foundation for Bayesian statistical inference investigations. Here,  $A$  and  $B$  represent events, while  $P(*)$  represents the probability of an event occurring.

For parameters  $\theta = [\theta_1, \theta_2, \dots, \theta_p]$  informed by observations  $[\nu_1, \nu_2, \dots, \nu_n]$ , we employ the corresponding relation

$$\pi(\theta|\nu) = \frac{\pi(\nu|\theta)\pi_0(\theta)}{\int_{\mathbb{R}^p} \pi(\nu|\theta)\pi_0(\theta) d\theta}. \quad (3.63)$$

Here,  $\pi(\theta|\nu)$  is the posterior distribution, while  $\pi_0(\theta)$  and  $\pi(\nu|\theta)$  represent the prior density and likelihood function, respectively, and the integral in the denominator is a normalization factor.

#### 3.5.1 Markov Chain Monte Carlo (MCMC)

In practice, direct implementation of (3.63) for large parameter dimensions is prohibitive. The state-of-the-art alternative to evaluating the normalization constant and obtaining marginal densities, is

the employment of Markov chain Monte Carlo (MCMC) techniques [51]. Here, the Markov chains' stationary distributions reflect the posterior densities for each iterative Monte Carlo random sample. In the next section, we summarize the main MCMC algorithm implemented in this dissertation for Bayesian statistical inference.

### 3.5.2 Delayed Rejection Adaptive Metropolis (DRAM)

Among MCMC algorithms for constructing posterior densities that characterize parameter uncertainties, the delayed rejection adaptive metropolis (DRAM) algorithm is an appealing option since it incorporates learned information as candidate parameter values are accepted in each Monte Carlo chain sample iteration [18, 51]. The algorithm uses the Metropolis-Hastings algorithm [7, 51] for random sampling from the posterior distributions, while adding two extra steps—adaptation and delayed rejection.

The delayed rejection step improves mixing in the parameter chains by decreasing the variance of the proposal distribution. Additionally, the adaptive step enhances updates to the proposal distributions via the chain covariance matrix and associated chain accepted candidates. This step efficiently enables the correction of poor initial estimates and prior distributions. We summarize the procedure in Algorithm A.0.1 in the Appendix, while the delayed rejection step is given in Algorithm A.0.2. Note that the updated chain covariance matrix design parameter  $s_p$  and length  $k_0$  of the adaptation interval, respectively depend on the dimension  $p$  of the parameter space and the necessity of ensuring a nonsingular proposal chain covariance matrix. Typically, the value of  $s_p$  is taken to be  $s_p = 2.38^2/p$ , while  $k_0$  is taken to be 100 [18]. Other design parameters such as  $n_s$  and  $\sigma_s^2$  are the number of observations and mean squared error of observations with respect to information producing the prior. Oftentimes with a noninformative prior, one takes  $n_s$  to be small, such that  $n_s = 0.1 to 1$  in value [51]. Note that for subsequent Bayesian statistical inference, we use the MATLAB DRAM code available at <https://wiki.helsinki.fi/display>.

### 3.5.3 Model Calibration

In this dissertation, we use the following general statistical model for Bayesian model calibration. The statistical model incorporates the parameter-dependent model response along with associated random errors, and is defined to be

$$M^{obs}(s) = f_s(\Theta) + \varepsilon_s, \quad s = 1, \dots, n. \quad (3.64)$$

Here, the random variables  $M^{obs}(s)$  and  $\varepsilon_s$ , respectively denote measurement observations and errors with respect to the model response  $f_s(\Theta)$ . Note that the errors  $\varepsilon_s$  are assumed to be independent and identically distributed (iid), and  $\varepsilon \sim \mathcal{N}(0, \sigma^2)$ . We let  $m^{obs}$  be realizations of the random

variable  $M^{obs}$ .

In the context of our subsequent models and Bayesian inference, Bayes equation becomes

$$\pi(\theta|m^{obs}) = \frac{\ell(m|\theta)\pi_0(\theta)}{\int_{\mathbb{R}^p} \ell(m|\theta)\pi_0(\theta) d\theta} \quad (3.65)$$

where the likelihood function is

$$\ell(m|\theta) = e^{-\sum_{s=1}^n [m^{obs}(s) - f_s(\theta)]^2 / 2\sigma^2}. \quad (3.66)$$

For all subsequent Bayesian model calibration studies in this dissertation we employ the DRAM algorithm given in Algorithm A.0.1 in the Appendix.

## 3.6 Uncertainty Propagation

Posterior densities of the type constructed from the Bayesian analysis introduced in Section 3.5, are often sampled to construct distributions for model responses. We use the probability densities to propagate input uncertainties and construct credible intervals which quantify the accuracy of the model fits, as detailed in Smith [51]. We refer to this method as sampling-based uncertainty propagation, and it is the method of choice for constructing the credible intervals in the 180° and 90° domain wall energy applications of Chapter 6 and Chapter 7.

### 3.6.1 Sampling

As discussed in Chapter 5, there are several cases considered for model parameters and their propagation of uncertainties. In the first case, we use the mean values and standard deviations from the sampled chains obtained from inference to construct densities assuming normal distributions. Upon the identification of a quantity of interest (QoI), we then randomly sample the parameters and perform corresponding model realizations with the goal of constructing credible intervals. In the second scenario, we sample directly from the chains constructed using Bayesian analysis techniques. Both methods are advantageous in that they are independent of the parameter dimension, since one can simultaneously sample from the parameter distributions or constructed chains.

As detailed in Chapter 9 of [51], the convergence rate for sampling-based uncertainty propagation is  $\frac{1}{\sqrt{M}}$ , where  $M$  is the number of simulations. Therefore, to increase the accuracy by one order of magnitude, we increase the number of simulations by factors of 100. This is infeasible for more computationally expensive models, but is appropriate for the models investigated here. We apply sampling-based uncertainty propagation techniques in later chapters of this dissertation.

### 3.6.2 Energy Statistics

To verify parameter selection results employed in later chapters, we compare credible intervals constructed from uncertainty propagation of all parameters  $\theta$ , with the uncertainty propagation of only sensitive parameters, denoted by  $\theta^{sens}$ . We construct densities from these credible intervals and measure how close the densities are to being the same, using energy statistics.

Energy statistics methods are used to measure distances between statistical observations. We employ the method based on [58] to test null hypothesis  $H_0 : F_X = F_Y$  that two distributions are the same against the alternate hypothesis  $H_1 : F_X \neq F_Y$ . We are often interested in distributions constructed from 99% credible intervals since these observations encapsulate the majority of the uncertainty.

To test the null hypothesis against the alternate hypothesis,

$$H_0 : F_X = F_Y \text{ versus } H_1 : F_X \neq F_Y,$$

consider two independent random samples

$$X = \{X_1, X_2, \dots, X_{n_1}\}, \quad Y = \{Y_1, Y_2, \dots, Y_{n_2}\},$$

respectively sampled from  $F_X$  and  $F_Y$ . We start by constructing the energy distance

$$\varepsilon_{n_1, n_2} = \frac{2}{n_1 n_2} \sum_{i=1}^{n_1} \sum_{m=1}^{n_2} \|X_i - Y_m\| - \frac{1}{n_1^2} \sum_{i=1}^{n_1} \sum_{j=1}^{n_1} \|X_i - X_j\| - \frac{1}{n_2^2} \sum_{k=1}^{n_2} \sum_{m=1}^{n_2} \|Y_k - Y_m\|, \quad (3.67)$$

to evaluate the test statistic

$$T_{n_1, n_2} = \frac{n_1 n_2}{n_1 + n_2} \varepsilon_{n_1, n_2}. \quad (3.68)$$

The null hypothesis is rejected if the test statistic  $T_{n_1, n_2}$  is large, whereas it cannot be rejected if  $T_{n_1, n_2}$  is small. To determine the relative size with statistic replicates we employ the bootstrap method.

Consider the pooled sample  $W = X \cup Y$ , containing the original samples  $X$  and  $Y$ . We choose a significance  $\alpha$ , along with total number of replicates  $M$ , such that  $(M + 1)\alpha$  is an integer. We then compute energy statistic replicates  $T_{n_1, n_2}^{(k)}$ , by resampling

$$X^{(k)} = \{X_1^{(k)}, X_2^{(k)}, \dots, X_{n_1}^{(k)}\}, \quad Y^{(k)} = \{Y_1^{(k)}, Y_2^{(k)}, \dots, Y_{n_2}^{(k)}\}$$

for  $k = 1, \dots, M$ , and evaluating relation (3.68). The pooled sample  $W$  enables mixing such that  $X_i^{(k)}, Y_j^{(k)} \in W$ ,  $i = 1, \dots, n_1$ ,  $j = 1, \dots, n_2$ . We reject the null hypothesis  $H_0$  if  $100(1 - \alpha)\%$  of the replicates  $T_{n_1, n_2}^{(k)}$  are exceeded by the original energy test statistic  $T_{n_1, n_2}$ .



## CHAPTER

# 4

## MONODOMAIN ENERGY ANALYSIS

The stored energy functional used in this dissertation follows from Ginzburg-Landau free energy theory [14]. A three-dimensional continuum stored energy modeling framework for ferroelectric materials, based on the Ginzburg-Landau theory, is given by Cao and Cross [5]. The derivation of our model follows this framework and is presented in [33, 37], where quantum density functional theory (DFT) calculations are implemented to inform the developed continuum model. Here, we use global sensitivity analysis to determine the most influential model parameters, and quantify the uncertainty in the output apportioned to the uncertainty in the inputs.

Here, we take polarization and strain to be the order parameters. We express the model as a function of polarization  $\mathbf{P}$  and total strain  $\varepsilon$ ,

$$u(\varepsilon, \mathbf{P}) = u_M(\varepsilon) + u_P(\mathbf{P}) + u_C(\varepsilon, \mathbf{P}) + u_R(\varepsilon). \quad (4.1)$$

In (4.1),  $u(\varepsilon, \mathbf{P})$  is the total energy per unit volume. The terms  $u_M$ ,  $u_P$ ,  $u_C$  and  $u_R$ , respectively denote the mechanical, Landau, electrostrictive, and residual energy per unit volume. The variables  $\mathbf{P}$  and  $\varepsilon$  are the independent polarization and strain variables, respectively.

The mechanical energy, with respect to a reference cubic state, is

$$u_M(\varepsilon) = \frac{c_{11}}{2}(\varepsilon_{11}^2 + \varepsilon_{22}^2 + \varepsilon_{33}^2) + c_{12}(\varepsilon_{11}\varepsilon_{22} + \varepsilon_{22}\varepsilon_{33} + \varepsilon_{11}\varepsilon_{33}) + 2c_{44}(\varepsilon_{12}^2 + \varepsilon_{23}^2 + \varepsilon_{13}^2), \quad (4.2)$$

based on the assumption of linear elasticity. Note that  $c_{11}$ ,  $c_{12}$  and  $c_{44}$  are elastic coefficients ex-

pressed in Voigt notation [30]. We note that the elasticity theory has been thoroughly developed in the literature for the material lead titanate. This includes properties for the elastic coefficients  $c_{11}$ ,  $c_{12}$  and  $c_{44}$  [24]. As a result, throughout the analysis of the monodomain and polydomain continuum models, we assume fixed elastic properties, setting  $c_{11}$ ,  $c_{12}$  and  $c_{44}$  at the values given in Table 4.1.

The sixth-order Landau polarization energy is

$$\begin{aligned} u_P(\mathbf{P}) = & \alpha_1(P_1^2 + P_2^2 + P_3^2) + \alpha_{11}(P_1^2 + P_2^2 + P_3^2)^2 + \alpha_{12}(P_1^2 P_2^2 + P_2^2 P_3^2 + P_1^2 P_3^2) \\ & + \alpha_{111}(P_1^6 + P_2^6 + P_3^6) + \alpha_{112}[P_1^4(P_2^2 + P_3^2) + P_2^4(P_1^2 + P_3^2) + P_3^4(P_1^2 + P_2^2)] \\ & + \alpha_{123}P_1^2 P_2^2 P_3^2. \end{aligned} \quad (4.3)$$

Here,  $\alpha_1$ ,  $\alpha_{11}$ ,  $\alpha_{12}$ ,  $\alpha_{111}$ ,  $\alpha_{112}$  and  $\alpha_{123}$  are phenomenological parameters influencing the ferroelectric phase transition in the Landau energy. When considering both paraelectric and ferroelectric phase transitions, the Landau parameters are functions of temperature. These are, however, treated as constants in the ferroelectric phase when cooling through the Curie temperature  $T_C$ . A goal of the global sensitivity and uncertainty analyses is to determine the importance of including sixth-order terms rather than employing only up to a fourth-order relation.

The coupling of strain  $\varepsilon$  and polarization  $\mathbf{P}$  is exhibited by the electrostrictive energy

$$\begin{aligned} u_C(\varepsilon, \mathbf{P}) = & -q_{11}(\varepsilon_{11}P_1^2 + \varepsilon_{22}P_2^2 + \varepsilon_{33}P_3^2) - q_{12}[\varepsilon_{11}(P_2^2 + P_3^2) + \varepsilon_{22}(P_1^2 + P_3^2) + \varepsilon_{33}(P_1^2 + P_2^2)] \\ & - q_{44}(\varepsilon_{12}P_1^2 P_2^2 + \varepsilon_{13}P_1 P_3 + \varepsilon_{23}P_2 P_3), \end{aligned} \quad (4.4)$$

where the parameters  $q_{11}$ ,  $q_{12}$  and  $q_{44}$  denote the electrostrictive coefficients.

Lastly, the residual energy is

$$u_R(\varepsilon) = \sigma_{ij}^R \varepsilon_{ij}. \quad (4.5)$$

This energy term is motivated by the monodomain continuum model analysis, where the unit cell is held fixed with respect to a reference cubic state. The residual stress parameters  $\sigma_{ij}^R$  constrain the unit cell to this cubic state, and thus must be estimated. We note that this is an additional energy term not originally included in Landau-Ginzburg theory, but proposed in the work by Miles et al. [33] to accommodate the DFT calculations informing the model.

We discuss the monodomain continuum model next, summarizing the parameters, independent variables, and responses relevant to our analysis.

**Table 4.1** Elastic coefficients obtained from [24].

Parameter	$c_{11}$	$c_{12}$	$c_{44}$	Units
Value	3.206e-1	1.397e-1	9.647e-2	$\mu\text{J}/\mu\text{m}^3$

## 4.1 Monodomain Continuum Model

We note that DFT calculations were implemented in [33] to calibrate the monodomain continuum model. The DFT analysis focused on energy, stress, and polarization computations derived from first-principles investigations. The total strain is zero in the cubic state when held fixed. This permits a calibration of the Landau energy (4.3), independent of coupling effects in the electrostrictive energy (4.4). Moreover, the effect of electrostriction is implemented via the continuum stress relation

$$\boldsymbol{\sigma} = \frac{\partial u}{\partial \boldsymbol{\varepsilon}}. \quad (4.6)$$

This relation yields the stress tensor

$$\boldsymbol{\sigma} = \mathbf{c} : \boldsymbol{\varepsilon} + \boldsymbol{\sigma}^R - \mathbf{q} : \mathbf{P}\mathbf{P}. \quad (4.7)$$

Here, the fourth-order elastic tensor  $\mathbf{c}$  and the residual stress tensor  $\boldsymbol{\sigma}^R$  follow after the derivative of the residual energy (4.5) with respect to strain.

DFT computations were carried out by constraining the polarization to rotate from  $P_3$  to  $P_2$ . The employed values are presented in Figure 4.1, and yield the simplified residual stresses  $\sigma_{11}^R = \sigma_{22}^R$  and  $\sigma_{13}^R = 0$ . The remaining stress component outputs are thus

$$\begin{aligned} \sigma_{11} &= c_{11}\varepsilon_{11} + c_{12}(\varepsilon_{22}\varepsilon_{33}) - q_{11}P_1^2 - q_{12}(P_2^2 + P_3^2) + \sigma_{11}^R, \\ \sigma_{22} &= c_{11}\varepsilon_{22} + c_{12}c_{12}(\varepsilon_{11} + \varepsilon_{33}) - q_{11}P_2^2 - q_{12}(P_1^2 + P_3^2) + \sigma_{22}^R, \\ \sigma_{22} &= c_{11}\varepsilon_{22} + c_{12}c_{12}(\varepsilon_{11} + \varepsilon_{33}) - q_{11}P_2^2 - q_{12}(P_1^2 + P_3^2) + \sigma_{22}^R, \\ \sigma_{23} &= 2c_{44}\varepsilon_{23} - 2q_{44}P_2P_3 + \sigma_{23}^R. \end{aligned} \quad (4.8)$$

Given the fixed elastic properties and the unit cell held fixed to a reference cubic state, we evaluate sensitivities and perform the uncertainty analysis with respect to the zero strain case.

Thus, we define the parameters of interest in the analysis as the Landau energy parameters

$$\theta_P = [\alpha_1, \alpha_{11}, \alpha_{12}, \alpha_{111}, \alpha_{112}], \quad (4.9)$$

and the set of normal and shear stress component parameters

$$\theta_{\sigma_{ns}} = [q_{11}, q_{12}, \sigma_{11}^R, \sigma_{22}^R, \sigma_{33}^R], \theta_{\sigma_s} = [q_{44}, \sigma_{23}^R]. \quad (4.10)$$

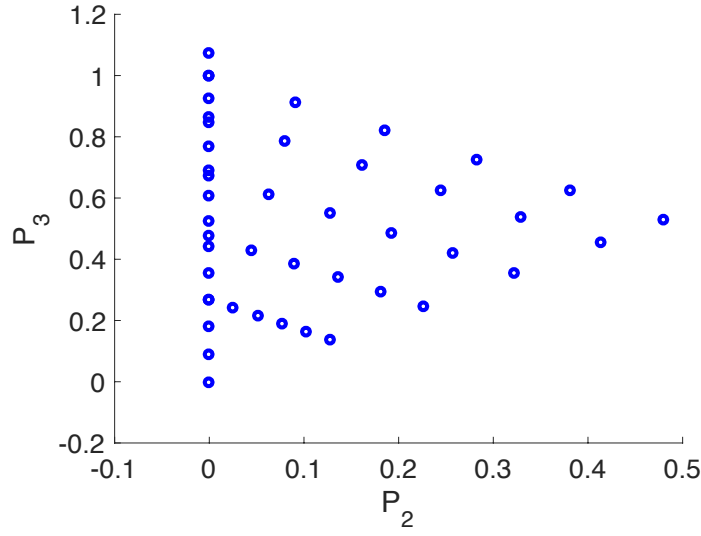


**Figure 4.1** Input polarization values of  $P_2$  and  $P_3$  obtained from the DFT analysis implemented in [33], and employed in the Landau polarization energy (4.3).

This forms the combined set of stress parameters

$$\theta_\sigma = [\theta_{\sigma_{ns}}, \theta_{\sigma_s}].$$

We denote the complete set of parameters in the monodomain analysis as

$$\theta_{MD} = [\theta_P, \theta_\sigma]. \quad (4.11)$$

Responses in our model are then compared to the DFT outputs via

$$y_{MD}(\theta_{MD}) = [u_P(\theta_P), \sigma_{11}(\theta_{\sigma_{ns}}), \sigma_{22}(\theta_{\sigma_{ns}}), \sigma_{33}(\theta_{\sigma_{ns}}), \sigma_{23}(\theta_{\sigma_s})]. \quad (4.12)$$

This includes the polarization energy, and the normal and shear stress components. To define a quantity of interest suitable for global sensitivity analysis, we suppress the dependence of the outputs on the polarization. This permits the discussion of the sensitivity of the responses to all parameters. In addition, the independence between the Landau energy  $u_P(\theta_P)$  and the stress components  $\sigma_{11}(\theta_{\sigma_{ns}})$ ,  $\sigma_{22}(\theta_{\sigma_{ns}})$ ,  $\sigma_{33}(\theta_{\sigma_{ns}})$ ,  $\sigma_{23}(\theta_{\sigma_s})$ , allows the sensitivity of these responses to the polarization energy parameters  $\theta_P$  and stress parameters  $\theta_\sigma$  to be analyzed separately. A least squares optimization of the parameters yields the nominal values of the parameters  $\theta_{MD}$ , presented in Table 4.2

In standard global sensitivity analysis, we define the scalar quantities of interest as follows. In

the case of the polarization energy response, we employ the pseudo-response

$$Y_P(\theta_P) = \frac{1}{N} \sum_{n=1}^N u_P(P_2^n, P_3^n; \theta_P). \quad (4.13)$$

This response averages over the  $N$  polarization values  $(P_2^n, P_3^n)$ ,  $n = 1, \dots, N$ , plotted in Figure 4.1. In the case of the vector-valued stress responses  $y_{\sigma_{ns}}(\theta_{\sigma_{ns}}) = [\sigma_{11}, \sigma_{22}, \sigma_{33}]$  and  $y_{\sigma_s}(\theta_{\sigma_s}) = \sigma_{23}$ , we define the pseudo-responses

$$Y_{\sigma_{ns}}(\theta_{\sigma_{ns}}) = \frac{1}{3N} \left( \sum_{n=1}^N \sigma_{11}(P_2^n, P_3^n; \theta_{\sigma_{ns}}) + \sum_{n=1}^N \sigma_{22}(P_2^n, P_3^n; \theta_{\sigma_{ns}}) + \sum_{n=1}^N \sigma_{33}(P_2^n, P_3^n; \theta_{\sigma_{ns}}) \right) \quad (4.14)$$

and

$$Y_{\sigma_s}(\theta_{\sigma_s}) = \frac{1}{N} \sum_{n=1}^N \sigma_{23}(P_2^n, P_3^n; \theta_{\sigma_s}). \quad (4.15)$$

Given that the monodomain responses given in (4.13), (4.14) and (4.15) are linearly parameterized, we express them as

$$\begin{aligned} Y_P(\theta_P) &= [a_1, a_2, a_3, a_4, a_5][\alpha_1, \alpha_{11}, \alpha_{12}, \alpha_{111}, \alpha_{112}]^T, \\ Y_{\sigma_{ns}}(\theta_{\sigma_{ns}}) &= [b_1, b_2, b_3, b_4, b_5][q_{11}, q_{12}, \sigma_{11}^R, \sigma_{22}^R, \sigma_{33}^R]^T, \\ Y_{\sigma_s}(\theta_{\sigma_s}) &= [c_1, c_2][q_{44}, \sigma_{23}^R]^T. \end{aligned}$$

Here,

**Table 4.2** Nominal values for the polarization parameters  $\theta_P$  and the stress component parameters  $\theta_{\sigma}$ , defined in (4.9) and (4.10), respectively. The nominal values were obtained from a least-squares optimization of the outputs (4.12).

Parameter	$\alpha_1$	$\alpha_{11}$	$\alpha_{12}$	$\alpha_{111}$	$\alpha_{112}$
Units	MV·m/C	MV·m <sup>5</sup> /C <sup>3</sup>	MV·m <sup>5</sup> /C <sup>3</sup>	MV·m <sup>9</sup> /C <sup>5</sup>	MV·m <sup>9</sup> /C <sup>5</sup>
Nominal Value	-389.2	761.1	414.6	61.61	-740.5
Parameter	$q_{11}$	$q_{12}$	$\sigma_{11}^R$	$\sigma_{22}^R$	$\sigma_{33}^R$
Units	GV·m/C	GV·m/C	GPa	GPa	GPa
Nominal Value	19.2	3.14	-3.98	-4.00	-3.41
Parameter	$q_{44}$	$\sigma_{23}^R$			
Units	GV·m/C	GPa			
Nominal Value	1.40	-8.16e-4			

$$a_1 = \frac{1}{N} \sum_{n=1}^N (P_{2_n}^2 + P_{3_n}^2), \quad a_2 = \frac{1}{N} \sum_{n=1}^N (P_{2_n}^2 + P_{3_n}^2)^2, \quad a_3 = \frac{1}{N} \sum_{n=1}^N P_{2_n}^2 P_{3_n}^2,$$

$$a_4 = \frac{1}{N} \sum_{n=1}^N (P_{2_n}^6 + P_{3_n}^6), \quad a_5 = \frac{1}{N} \sum_{n=1}^N (P_{2_n}^4 P_{3_n}^2 + P_{3_n}^4 P_{2_n}^2),$$

and

$$b_1 = -\frac{1}{3N} \sum_{n=1}^N (P_{2_n}^2 + P_{3_n}^2), \quad b_2 = -\frac{2}{3N} \sum_{n=1}^N (P_{2_n}^2 + P_{3_n}^2), \quad b_3 = b_4 = b_5 = \frac{1}{3},$$

$$c_1 = -\frac{1}{N} \sum_{n=1}^N (P_{2_n} P_{3_n}), \quad c_2 = 1.$$

This representation facilitates the analytic determination of the component functions necessary in the associated Sobol' decomposition for global sensitivity analysis.

## 4.2 Global Sensitivity Analysis

We employ sensitivity analysis to determine the sensitivity of the responses  $Y_P(\theta_P)$ ,  $Y_{\sigma_{ns}}(\theta_{\sigma_{ns}})$  and  $Y_{\sigma_s}(\theta_{\sigma_s})$  to the parameters  $\theta_P$ ,  $\theta_{\sigma_{ns}}$  and  $\theta_{\sigma_s}$ . Whereas in local sensitivity analysis partial parameter derivatives are used to quantify sensitivities about local nominal parameter values, global sensitivity analysis more broadly accommodates sensitivities across the entire parameter space as detailed in Chapter 3. This allows us to fix noninfluential or unidentifiable parameters for subsequent Bayesian analysis in the manner described in Chapter 1.

In the monodomain continuum model analysis, we employ the Morris screening and Sobol global sensitivity analysis methods, which we introduced in Chapter 3. We show how the assumption of uniformly distributed parameters can lead to incorrect interpretation of sensitivity analysis results, when fixing presumed non-influential parameters and performing Bayesian inference on the influential parameters. We employ the global sensitivity analysis method for highly correlated parameters, also developed in Chapter 3, to compare and contrast with previous results. Finally, we use the local sensitivity-based Fisher information matrix analysis to determine the identifiable parameters in the system and verify the results of the correlated global sensitivity analysis. These methods applied to the monodomain continuum model are presented in the following sections.

In the following analyses, we express the pseudo-responses (4.13), (4.14) and (4.15) generically

as

$$Y = f(\Theta),$$

where  $\Theta = [\Theta_1, \dots, \Theta_p]$  is a vector of random variables representing  $\Theta_P$ ,  $\Theta_{\sigma_{ns}}$  or  $\Theta_{\sigma_s}$ . Likewise,  $Y$  denotes the polarization response  $Y_P$ , the electrostrictive normal stress response  $Y_{\sigma_{ns}}$ , or the electrostrictive shear stress response  $Y_{\sigma_s}$ . Additionally,  $\theta$  will be used to indicate realizations of the random variables  $\Theta$ .

#### 4.2.1 Sensitivity Analysis for Uncorrelated Parameters

As part of parameter subset selection, global sensitivity analysis is in general performed before model calibration and Bayesian inference. Thus, in absence of information about parameter distributions incorporating any correlation structure, one typically assumes the parameters to be uniformly and independently distributed. This assumption simplifies the determination of the component functions relevant to Sobol' analysis, and justifies the employment of the methods detailed in Section 3.1.

Here, we assume the parameters  $\Theta$  to be uniformly and independently distributed such that

$$\Theta_i \sim \mathcal{U}(\theta_i^{nom} - 0.25|\theta_i^{nom}|, \theta_i^{nom} + 0.25|\theta_i^{nom}|), \quad \text{for } i = 1, \dots, p,$$

where  $|\theta_i^{nom}|$  are the nominal absolute values for  $\theta_P$  and  $\theta_\sigma$ , presented in Table 4.2. The value 0.25 was chosen as the perturbation value given that broad sampling is commonly provided in the parameter space, while the model behavior is not significantly changed. As detailed in Chapter 3, the intervals given here are mapped to  $[0, 1]$  to avoid scaling issues pertaining to physical parameter units.

#### Pearson Correlations

As was defined in Section 3, Pearson correlations quantify the degree to which responses depend on individual parameter variations. Qualitatively, this information is provided by scatterplots of responses computed by randomly sampling individual parameters. The intuition for employing Pearson correlations here is to obtain both initial qualitative and quantitative measures for global sensitivity of the polarization energy response (4.13), the normal stress response (4.14), and the shear stress response (4.15).

We analyze the Pearson correlations with respect to the polarization energy response (4.13). For the sampling procedure, we choose the interval

$$[\theta_i^{nom} - 0.25\theta_i^{nom}, \theta_i^{nom} + 0.25\theta_i^{nom}], \quad (4.16)$$

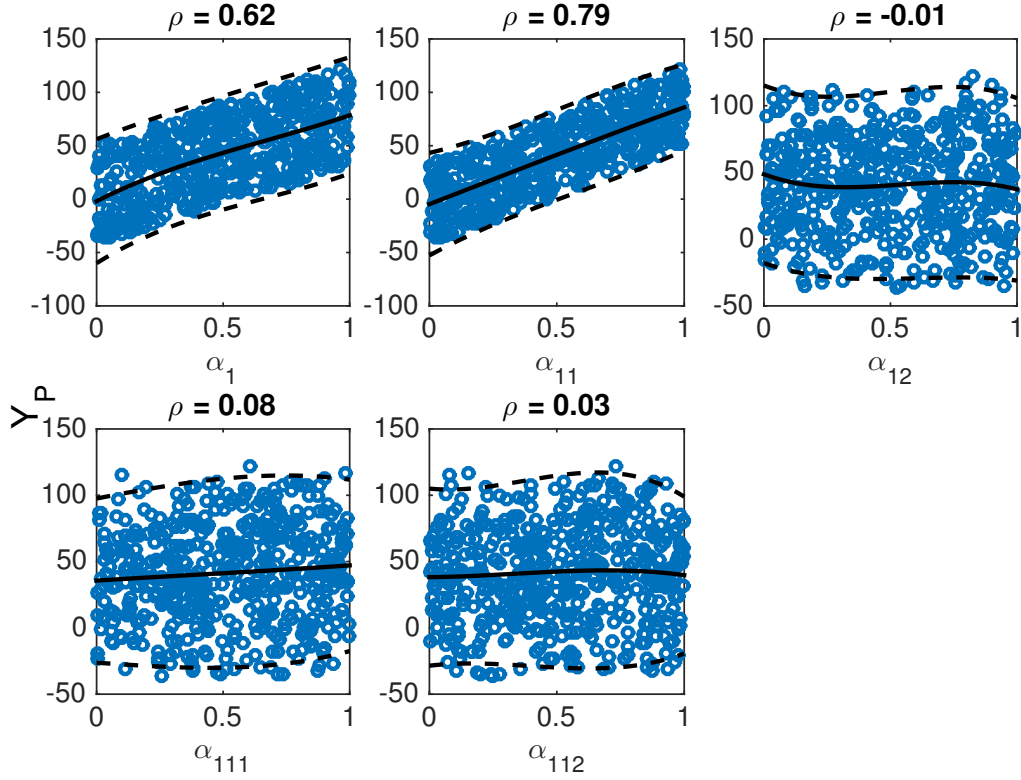


**Figure 4.2** Scatterplots, Pearson correlations  $\rho$  given by (3.7), means, and two standard deviation intervals for the polarization parameters  $\theta_p$  and response  $Y_p$  given (4.13).

where the nominal values  $\theta_i^{nom}$  are compiled in Table 4.2. In Figure 4.2, we plot scatterplots for the polarization parameters  $\alpha_1$ ,  $\alpha_{11}$ ,  $\alpha_{12}$ ,  $\alpha_{111}$  and  $\alpha_{112}$ . We obtained the scatterplots with  $M = 1000$  realizations of the model, along with means and two standard deviation intervals. Likewise, we report the associated Pearson coefficients in Figure 4.2, as well as in Table 4.3. In relative terms, Pearson correlation coefficients close to 1 in value, indicate strong linear trends and influence on (4.13), with respect to the parameters  $\theta_p$ . We note that the values  $\rho = 0.64$  and  $\rho = 0.78$  for  $\alpha_1$  and  $\alpha_{11}$  are an order of magnitude larger than the coefficients for  $\alpha_{12}$ ,  $\alpha_{111}$  and  $\alpha_{112}$ . Qualitatively, this is reflected in the trends observed in the means and two standard deviation intervals. Presumably, this would provide initial evidence that the sixth-order parameters  $\alpha_{111}$  and  $\alpha_{112}$  are noninfluential, thus concluding that these terms could be fixed.

Assuming that the parameters  $\alpha_1$  and  $\alpha_{11}$  are the most sensitive parameters in the sense that they most influence the response (4.13), we fix all the other parameters at nominal values, and randomly sample only  $\alpha_1$  and  $\alpha_{11}$  in subsequent function evaluations. We present the obtained



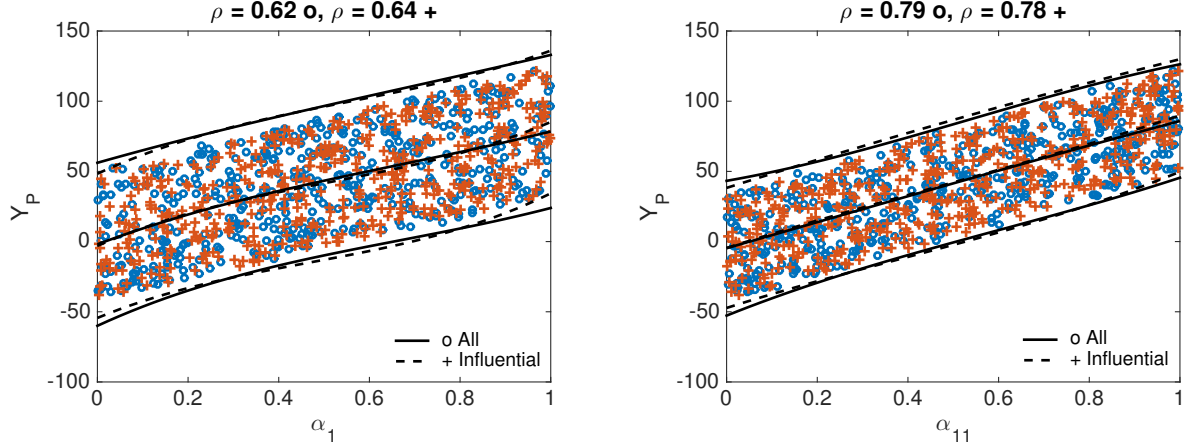


**Figure 4.3** Pearson correlations of sampled (a)  $\alpha_1$ , (b)  $\alpha_{11}$  against each of 500 realizations of  $Y_P$  (4.13), with all other parameters in  $\theta_P$  also sampled and only  $\alpha_1$ ,  $\alpha_{11}$  sampled. Pearson correlation coefficients  $\rho$  for each parameter are also presented. The labels (—) and (---) denote the means and two standard deviations for the cases where all parameters  $\theta_P$  are sampled to obtain the responses shown by (o), and only parameters  $\alpha_1$ ,  $\alpha_{11}$  are sampled to obtain the responses shown by (+).

scatterplot results in Figure 4.3, along with the associated Pearson correlation coefficients (3.7). This provides additional evidence that  $\alpha_1$  and  $\alpha_{11}$  are the most influential parameters.

### Morris Screening Measures

The Morris indices  $\mu_i^*$  and  $\sigma_i$  quantify individual effects as well as certain nonlinearities or interactions between parameters. Generally, one designates influential parameters as those having large values of both  $\mu_i^*$  and  $\sigma_i$ .

To construct the Morris sensitivity measures, we employed the Morris screening sampling strategy Algorithm 3.1.1. We used a total of  $s = 40$  samples in the determination of the measures. In the case of the Landau energy, parameters  $\alpha_1$  and  $\alpha_{11}$  seem to be the most sensitive, as exhibited by the coefficient values in Table 4.3.

### Sobol' Sensitivity Indices

The Sobol' sensitivity indices for correlated parameters are constructed assuming a uniform distribution for all the parameters. We implement Algorithm 3.1.2 introduced in Section 3.1.2, with a total of 40,000 samples to construct the indices. This yields the results given in Table 4.3. These results are consistent with the Pearson correlations and Morris screening sensitivity indices. Table 4.3 indicates that only  $\alpha_1$  and  $\alpha_{11}$  are influential, implying that a fourth-order Landau energy is sufficient for lead titanate. Typically, assuming that these results are correct, we then fix the non-influential parameters

**Table 4.3** Sobol' sensitivity indices  $S_i$ ,  $S_{T_i}$ , Morris screening measures  $\mu_i^*$ ,  $\sigma_i^*$  and Pearson correlation coefficients  $\rho_{all}$ ,  $\rho_{inf}$  for the Landau energy phenomenological parameters  $\theta_p$  (4.9). Note that  $\rho_{inf}$  indicates Pearson correlation coefficients when only presumed influential parameters are sampled while all others are fixed. The shaded cells correspond to significant indices, measures and coefficients.

	$\alpha_1$	$\alpha_{11}$	$\alpha_{12}$	$\alpha_{111}$	$\alpha_{112}$
$S_i$	0.40	0.60	4.53e-5	1.12e-3	1.49e-4
$S_{T_i}$	0.40	0.59	1.97e-4	1.89e-3	1.44e-4
$\mu_i^*$	74.77	90.17	1.64	5.13	1.41
$\sigma_i^*$	116.81	126.44	2.31	6.68	2.11
$\rho_{all}$	0.62	0.79	-0.01	0.08	0.03
$\rho_{inf}$	0.64	0.78	-	-	-

$\alpha_{12}$ ,  $\alpha_{111}$  and  $\alpha_{112}$ , and proceed with model calibration inferring only the influential parameters  $\alpha_1$  and  $\alpha_{11}$ . We expect to see no effect on the posterior densities of other parameters or the model uncertainties when fixing the noninfluential parameters since the associated perturbations would not be reflected in the output.

### 4.3 Bayesian Statistical Analysis

In this section, we calibrate the monodomain model while fixing the presumed non-influential parameters, and only sampling the influential ones. We compare this with the case where all parameters are randomly sampled.

We employ the DRAM algorithm to infer the parameters  $\theta_p$  and  $\theta_\sigma$  using Bayesian statistical analysis. Note that we use the DFT simulations obtained from [33] to calibrate the polarization energy  $u_p$ , the normal stresses  $\sigma_{11}$ ,  $\sigma_{22}$ ,  $\sigma_{33}$  and the shear stress term  $\sigma_{23}$ . This work is based on the results in [33].

In the analysis, we used a total of 10000 iterations of the DRAM algorithm. We obtain the plots presented in Figure 4.4, for the chain of accepted parameter values. Likewise, we present the associated pairwise density plots in Figure 4.5. The strong correlation of the pairwise plots is explained by the covariance matrix

$$\mathbf{V}_{freq} = \begin{bmatrix} 1.057\text{e}+2 & -2.871\text{e}+2 & -1.307\text{e}+3 & 1.774\text{e}+2 & 2.932\text{e}+3 \\ -2.871\text{e}+2 & 8.541\text{e}+2 & 3.485\text{e}+3 & -5.569\text{e}+2 & -8.495\text{e}+3 \\ -1.307\text{e}+3 & 3.485\text{e}+3 & 5.361\text{e}+4 & -2.092\text{e}+3 & -1.074\text{e}+5 \\ 1.774\text{e}+2 & -5.569\text{e}+2 & -2.092\text{e}+3 & 3.764\text{e}+2 & 5.373\text{e}+3 \\ 2.932\text{e}+3 & -8.495\text{e}+3 & -1.074\text{e}+5 & 5.373\text{e}+3 & 2.269\text{e}+5 \end{bmatrix}, \quad (4.17)$$

obtained by employing the ordinary least squares (OLS) techniques detailed in [27, 51]. This method for constructing the covariance matrix yields values within the same order of magnitude as the covariance matrix

$$\mathbf{V}_{DRAM} = \begin{bmatrix} 1.077\text{e}+2 & -2.900\text{e}+2 & -1.299\text{e}+3 & 1.778\text{e}+2 & 2.918\text{e}+3 \\ -2.900\text{e}+2 & 8.525\text{e}+2 & 3.451\text{e}+3 & -5.512\text{e}+2 & -8.377\text{e}+3 \\ -1.299\text{e}+3 & 3.451\text{e}+3 & 5.266\text{e}+4 & -2.064\text{e}+3 & -1.063\text{e}+5 \\ 1.778\text{e}+2 & -5.512\text{e}+2 & -2.064\text{e}+3 & 3.698\text{e}+2 & 5.257\text{e}+3 \\ 2.918\text{e}+3 & -8.377\text{e}+3 & -1.063\text{e}+5 & 5.257\text{e}+3 & 2.256\text{e}+5 \end{bmatrix}, \quad (4.18)$$

obtained via Bayesian inference.

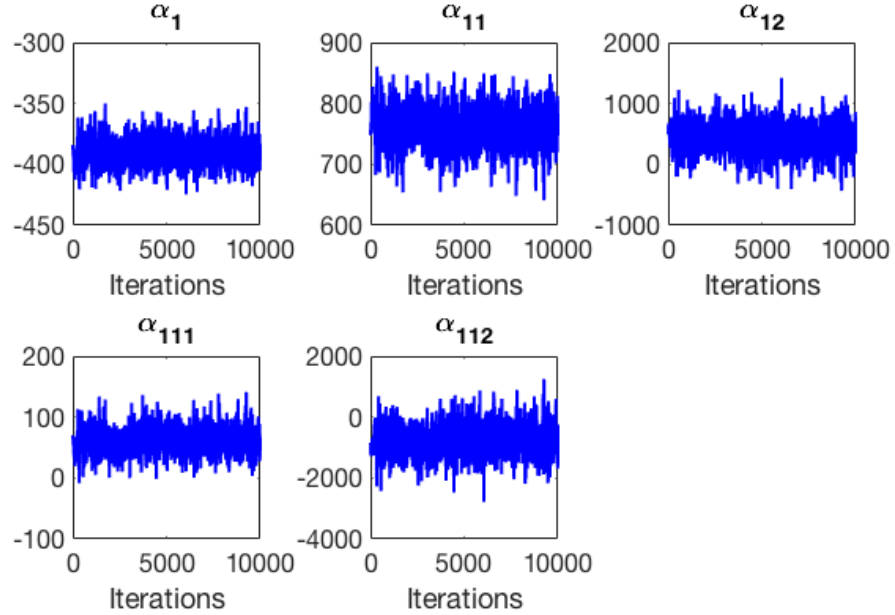


**Figure 4.4** Chain of accepted sampled Landau energy parameter values with respect to DFT simulations in [33], obtained using  $1 \times 10^4$  iterations.

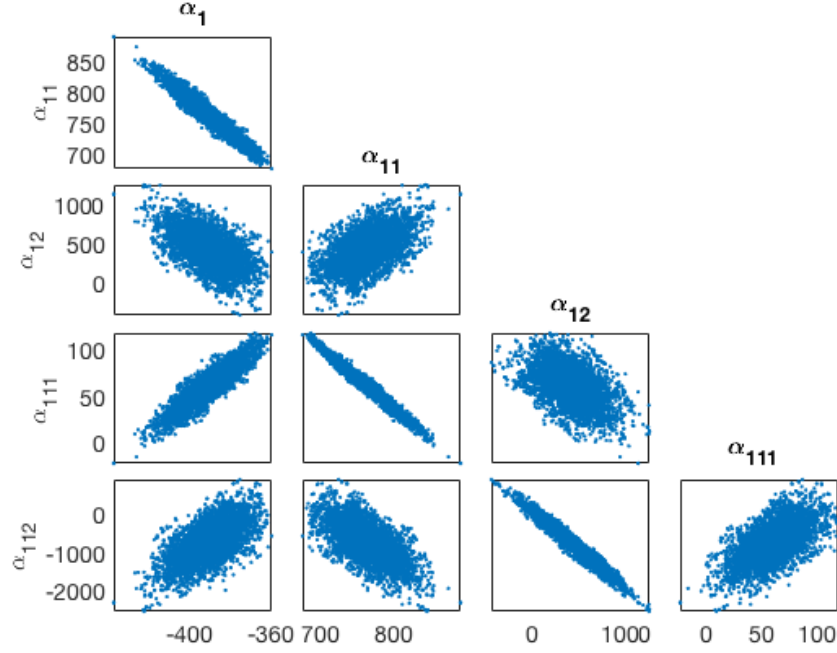


**Figure 4.5** Pairwise correlation among the Landau energy parameters (4.9). Strong correlation observed between the lower- and higher-order parameters.

The pairwise correlation plots and covariance matrix raise several questions with regard to our global sensitivity analysis. First, our assumption was that the parameters were uniformly and independently distributed in the absence of further prior information. What are the consequences given that we assumed these priors in the initial global sensitivity analysis? What effect does the correlation have on the model response? To answer these questions, we perform Bayesian inference when fixing the parameters determined to be non-influential while inferring only the influential ones. We present the analysis next.

### Bayesian Inference for Presumed Influential Parameters

In this case we fix the parameters  $\alpha_{12}$ ,  $\alpha_{111}$  and  $\alpha_{112}$  while using Bayesian analysis to infer  $\alpha_1$  and  $\alpha_{11}$ . If the fixed parameters are truly noninfluential, we would expect to see no effects on the distributions of the other parameters, given the high correlation we introduced in this section.

We present the resulting posterior densities obtained with 10,000 iterations of the DRAM algorithm in Figure 4.6. It is apparent that the parameters that were presumed to be noninfluential have an effect on the posterior distributions of the influential parameters. This motivates a sensitivity analysis where we incorporate the correlation given by the covariance matrix (4.17) as addressed in

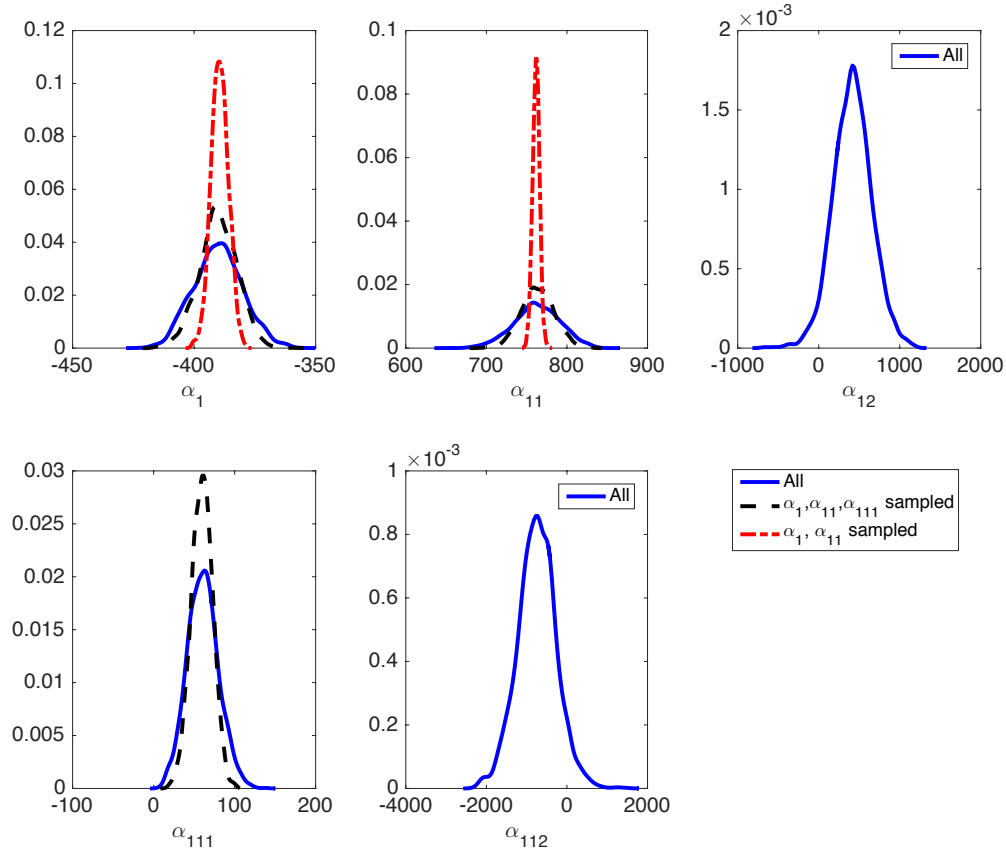


**Figure 4.6** Posterior densities obtained via Bayesian calibration of  $Y_p(\theta_p)$  in when (i) sampling all the parameters, (ii) sampling  $\alpha_1, \alpha_{11}, \alpha_{111}$  with  $\alpha_{12}, \alpha_{112}$  fixed, and (iii) sampling  $\alpha_1, \alpha_{11}$  with  $\alpha_{111}, \alpha_{12}, \alpha_{12}$  fixed.

the next section.

#### 4.4 Sensitivity Analysis for Correlated Parameters

There are two scenarios to consider when employing the global sensitivity analysis techniques for correlated parameters developed in Section 3.2; linearly or nonlinearly parameterized models. In the present case, the responses  $Y_p(\theta_p)$  (4.13),  $Y_{\sigma_{ns}}(\theta_{\sigma_{ns}})$  (4.14) and  $Y_{\sigma_s}(\theta_{\sigma_s})$  (4.15) are all linearly parameterized. Therefore, we illustrate the analytical and numerical techniques from Section 3.2.2 and Section 3.2.3 for quantifying the global sensitivity of the correlated parameters  $\theta_p$  (4.9) and  $\theta_{\sigma}$  (4.10).

## Analytic Determination of Component Functions

To incorporate parameter correlation when constructing the component functions (3.13), we first specify a distribution for the parameters  $\theta_P$ ,  $\theta_{\sigma_{ns}}$  and  $\theta_{\sigma_s}$ . This requires a parametric distribution approximation to the non-parametric posterior distributions created through Bayesian analysis. Namely, we require nominal values and covariance matrices in the construction of prior multivariate normal distributions. Recall from Table 4.2 in Section 4.1, and Section 4.3, that the nominal values and covariance matrices can be either obtained through Bayesian analysis, or by using asymptotic ordinary least squares (OLS) techniques.

We use the nominal values  $\mu_P$ ,  $\mu_{\sigma_{ns}}$  and  $\mu_{\sigma_s}$  provided in Table 4.2, and associated covariance matrices

$$\begin{aligned} \mathbf{V}_P &= \begin{pmatrix} 1.077\text{e}+2 & -2.900\text{e}+2 & -1.299\text{e}+3 & 1.778\text{e}+2 & 2.918\text{e}+3 \\ -2.900\text{e}+2 & 8.525\text{e}+2 & 3.451\text{e}+3 & -5.512\text{e}+2 & -8.377\text{e}+3 \\ -1.299\text{e}+3 & 3.451\text{e}+3 & 5.266\text{e}+4 & -2.064\text{e}+3 & -1.063\text{e}+5 \\ 1.778\text{e}+2 & -5.512\text{e}+2 & -2.064\text{e}+3 & 3.698\text{e}+2 & 5.257\text{e}+3 \\ 2.918\text{e}+3 & -8.377\text{e}+3 & -1.063\text{e}+5 & 5.257\text{e}+3 & 2.256\text{e}+5 \end{pmatrix}, \\ \mathbf{V}_{\sigma_{ns}} &= \begin{pmatrix} 0.0605 & 0.0014 & 0.0012 & 0.0021 & 0.0208 \\ 0.0014 & 0.0314 & 0.0115 & 0.0106 & 8.8239\text{e}-4 \\ 0.0012 & 0.0115 & 0.0097 & 0.0037 & 6.3619\text{e}-4 \\ 0.0021 & 0.0106 & 0.0037 & 0.0093 & 8.4661\text{e}-4 \\ 0.0208 & 8.8239\text{e}-4 & 6.3619\text{e}-4 & 8.4661\text{e}-4 & 0.0126 \end{pmatrix}, \\ \mathbf{V}_{\sigma_s} &= \begin{pmatrix} 3.4801\text{e}-4 & 3.6383\text{e}-5 \\ 3.6383\text{e}-5 & 1.1141\text{e}-5 \end{pmatrix} \end{aligned} \quad (4.19)$$

obtained through Bayesian inference, to construct the densities

$$\Theta_P \sim \mathcal{N}(\mu_P, \mathbf{V}_P), \Theta_{\sigma_{ns}} \sim \mathcal{N}(\mu_{\sigma_{ns}}, \mathbf{V}_{\sigma_{ns}}), \Theta_{\sigma_s} \sim \mathcal{N}(\mu_{\sigma_s}, \mathbf{V}_{\sigma_s}). \quad (4.20)$$

The strong correlation is incorporated through the random sampling of the parameters based on this distribution. We perform 10,000 realizations of the component functions (3.35), to obtain the plots in Figures 4.7, 4.8 and 4.9, for the Landau, normal stress, and shear stress parameters, respectively. The component functions determined analytically are denoted by the dashed black lines.

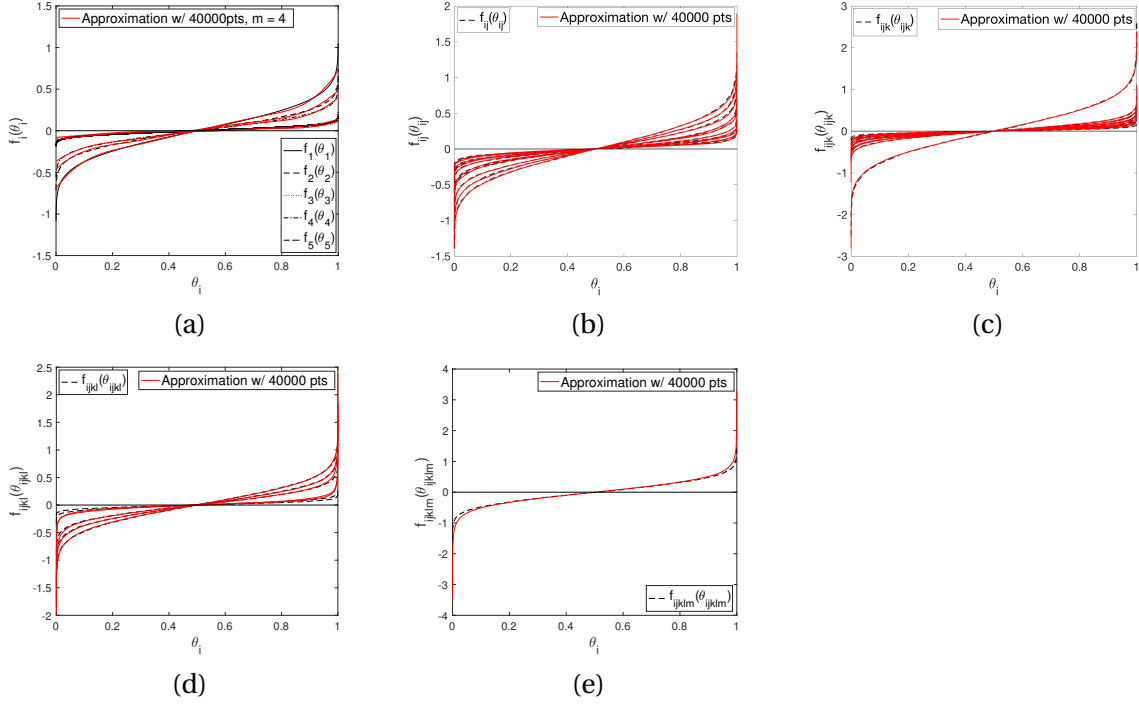


**Figure 4.7** (a) First, (b) second, (c) third, (d) fourth and (e) fifth-order component functions constructed using the analytical method (---) and the numerical method (—) for  $\theta_p$  in (4.13) with  $m = 4$  subintervals for the Cubic B spline basis functions.

## Numerical Determination of Component Functions

Using the numerical method, detailed in Section 3.2.3, for determining the Sobol' component functions, we again sample from densities (4.20) to incorporate the correlation in the parameters. Following the procedure, we first determine the basis expansion coefficients  $\alpha^i, \beta^{ij}, \gamma^{ijk}, \dots$ , in (3.38) by minimizing cost functionals of the type (3.39). We obtain the component functions presented in Figures 4.7, 4.8 and 4.9, for the Landau, normal stress, and shear stress parameters, respectively. Here, we denote the component functions determined via this numerical method by the red lines.

## Sobol' Sensitivity Indices

In the alternate variance-based sensitivity analysis framework of Section 3.2.1, first-order Sobol' sensitivity indices  $S_i$  quantify the fraction of uncertainty in the response that is attributed to the parameter  $\theta_i$ . The higher-order Sobol sensitivity indices  $S_{ij}, S_{ijk}, \dots$ , quantify effects due to parameter correlation and structural interactions in the model. The total sensitivity indices  $S_{T_i}$  additionally quantify the total fraction of uncertainty attributed to the individual parameter effects as well as

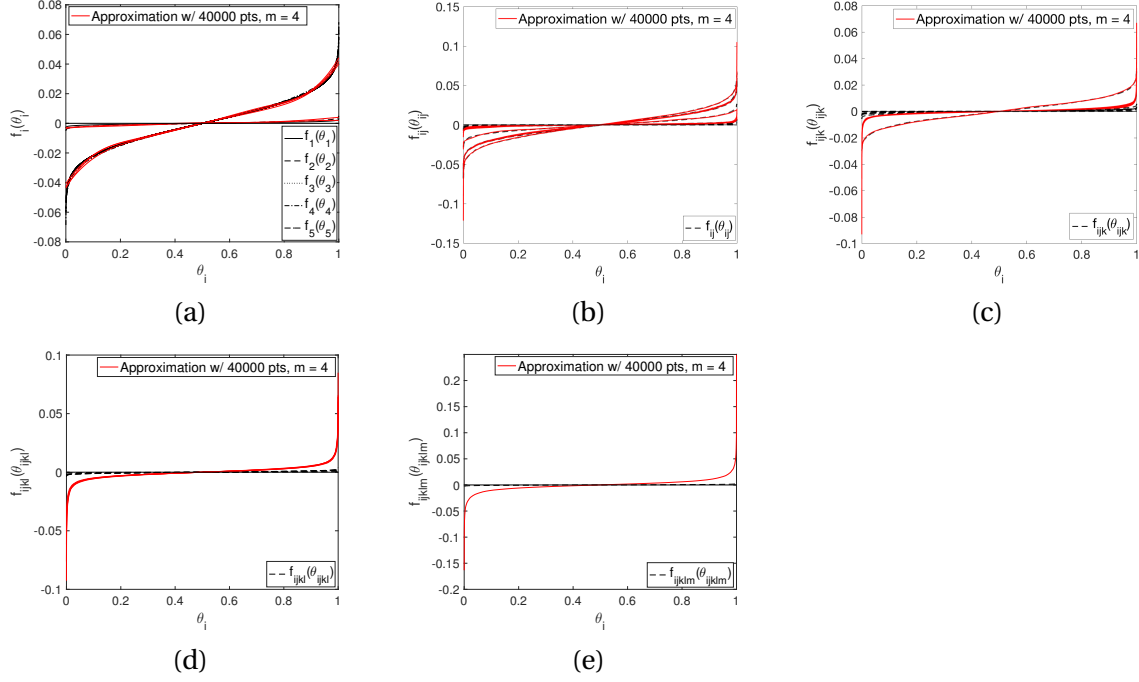


**Figure 4.8** (a) First, (b) second, (c) third, (d) fourth and (e) fifth order component functions constructed using the analytical method (---) and numerical method (—) for  $\theta_{\sigma_{ns}}$  in (4.14) with  $m = 4$  subintervals.

contributions from correlations and structural parameter interactions. Therefore, a more comprehensive measure of global parameter sensitivity is provided here as compared with the sensitivity

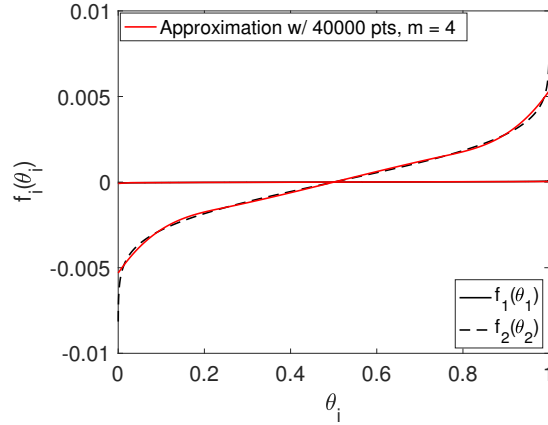


**Figure 4.9** First-order component functions constructed using the analytical method (---) and numerical method (—) for  $\theta_{\sigma_s}$  in (4.15) with  $m = 4$  subintervals.



measures obtained in Section 4.2.1.

For the component functions constructed using both the analytical and numerical methods, we construct the Sobol' indices (3.29), employing the Monte Carlo approximations

$$\begin{aligned}
S_{r_n} &= \frac{\text{cov}[f_{r_n}, Y]}{\text{var}[Y]} \approx \frac{\sum_{s=1}^K f_{r_n}(\theta_{r_n}^s) [f(\theta^s) - f_0]}{\sum_{s=1}^K [f(\theta^s) - f_0]^2}, \\
S_{r_n}^s &= \frac{\text{var}[f_{r_n}]}{\text{var}[Y]} \approx \frac{\sum_{s=1}^K f_{r_n}^2(\theta^s)}{\sum_{s=1}^K [f(\theta^s) - f_0]^2}, \\
S_{r_n}^c &= S_{r_n} - S_{r_n}^s,
\end{aligned} \tag{4.21}$$

Here, we employ the  $f_0$  approximation

$$f_0 \approx \frac{\sum_{s=1}^K f(\theta^s)}{K},$$

where  $K$  is the number of component function realizations to compute the sensitivity indices. We obtain the indices in Table 4.4 for  $\theta_P$ , Table 4.5 for  $\theta_{\sigma_{ns}}$  and Table 4.6 for  $\theta_{\sigma_s}$ , using a total of  $K = 10,000$  samples. We observe that for the pairs of most correlated Landau energy parameters second-order Sobol' sensitivity indices are significant, when the first-order indices are influential. For the normal stress parameters  $\theta_{\sigma_{ns}}$ , we make a similar observation in Table 4.5. The total sensitivity indices for  $\theta_P$ ,  $\theta_{\sigma_{ns}}$ , and  $\theta_{\sigma_s}$  all indicate that no parameter is non-influential due to contribution effects corresponding to parameter correlation.

To illustrate relative effects between the first-order and total sensitivity indices incorporating all contributions, in Figures 4.10, 4.11 and 4.12 we plot the indices  $S_i$  and  $S_{T_i}$ , respectively for the Landau parameters  $\theta_P$ , normal stress parameters  $\theta_{\sigma_{ns}}$  and shear stress parameters  $\theta_{\sigma_s}$ .

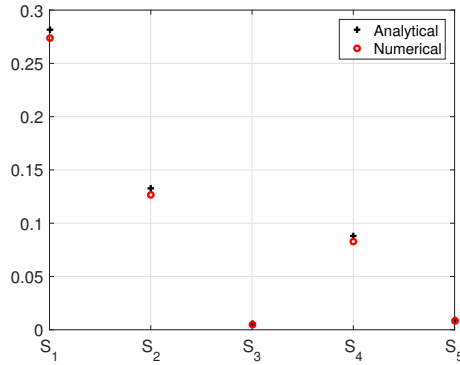
We observe that the magnitudes for the first-order indices  $S_3$  and  $S_5$  are relatively small, corresponding to parameters  $\alpha_{12}$  and  $\alpha_{112}$ . However, as observed in Figure 4.10(b), contributions due to higher-order parameter correlations have a significant effect on the values of the total sensitivity indices  $S_{T_1}$  and  $S_{T_2}$ . This observation indicates that the parameters  $\alpha_{12}$  and  $\alpha_{112}$  are still influential, thus explaining the results observed in posterior densities plotted in Figure 4.6. We make a similar conclusion about normal stress parameters  $q_{11}$  and  $q_{12}$ , as well as the shear stress parameter  $q_{44}$ .

## 4.5 Analysis Using the Fisher Information Matrix

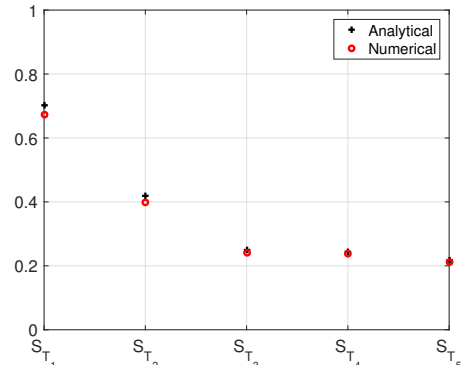
To corroborate the global sensitivity analysis results of Section 4.4, we employ the methodology detailed in Section 3.3.2, based on the analysis of the Fisher information matrix, to determine identifiable parameters. Namely, we apply Algorithm 3.3.2, to the Landau energy  $u_P$  (4.3), and the

**Table 4.4** Sensitivity indices for total contributions  $S_{r_n}$  constructed using the component functions  $f_{r_n}$  for the Landau energy parameters  $\theta_p$ . The A's and N's represent sensitivity indices derived from the analytical and numerical determination of the component functions, respectively. The indices correspond to the order specified by  $\theta_p = [\alpha_1, \alpha_{11}, \alpha_{12}, \alpha_{111}, \alpha_{112}]$ . The shaded cells designate significant indices.

	$S_1$	$S_2$	$S_3$	$S_4$	$S_5$					
A. 1 <sup>st</sup> order	0.281	0.133	0.006	0.088	0.009					
N. 1 <sup>st</sup> order	0.274	0.127	0.005	0.082	0.008					
	$S_{12}$	$S_{13}$	$S_{14}$	$S_{15}$	$S_{23}$	$S_{24}$	$S_{25}$	$S_{34}$	$S_{35}$	$S_{45}$
A. 2 <sup>nd</sup> order	0.100	0.062	0.060	0.067	0.012	0.021	0.016	-3.75e-4	0.002	-0.001
N. 2 <sup>nd</sup> order	0.109	0.065	0.068	0.072	0.014	0.029	0.019	0.002	0.004	0.002
	$S_{123}$	$S_{124}$	$S_{125}$	$S_{134}$	$S_{135}$	$S_{145}$	$S_{234}$	$S_{235}$	$S_{245}$	$S_{345}$
A. 3 <sup>rd</sup> order	-0.002	0.049	-0.052	0.013	-0.069	-0.024	0.032	-0.011	0.015	0.001
N. 3 <sup>rd</sup> order	4.20e-4	0.036	-0.052	0.016	-0.068	-0.023	0.036	-0.009	0.018	0.003
	$S_{1234}$	$S_{1235}$	$S_{1245}$	$S_{1345}$	$S_{2345}$					
A. 4 <sup>th</sup> order	-0.070	0.202	-0.011	0.088	-0.025					
N. 4 <sup>th</sup> order	-0.073	0.195	-0.011	0.092	-0.011					
	$S_{12345}$									
A. 5 <sup>th</sup> order	0.009									
N. 5 <sup>th</sup> order	-0.027									
	$S_{T_1}$	$S_{T_2}$	$S_{T_3}$	$S_{T_4}$	$S_{T_5}$					
A. Total Index	0.703	0.418	0.249	0.244	0.217					
N. Total Ind	0.672	0.400	0.242	0.238	0.211					



(a)



(b)

**Figure 4.10** Comparison of analytical and numerical methods obtain (a) first-order and (b) total sensitivity indices for (4.13).

**Table 4.5** Sensitivity indices for total contributions  $S_{r_n}$  constructed using the component functions  $f_{r_n}$  for the normal stress parameters  $\theta_{\sigma_{ns}}$ . The indices correspond to the order specified by  $\theta_{\sigma_{ns}} = [q_{11}, q_{12}, \sigma_{11}^R, \sigma_{22}^R, \sigma_{33}^R]$ . The shaded cells correspond to significant indices.

	$S_1$	$S_2$	$S_3$	$S_4$	$S_5$					
A. 1 <sup>st</sup> order	5.79e-4	0.001	0.158	0.176	0.164					
N. 1 <sup>st</sup> order	5.46e-4	0.001	0.156	0.179	0.162					
	$S_{12}$	$S_{13}$	$S_{14}$	$S_{15}$	$S_{23}$	$S_{24}$	$S_{25}$	$S_{34}$	$S_{35}$	$S_{45}$
A. 2 <sup>nd</sup> order	5.74e-5	-5.79e-4	-4.50e-4	0.180	0.157	0.141	0.002	-0.093	-0.018	-0.025
N. 2 <sup>nd</sup> order	7.42e-4	2.09e-4	9.70e-4	0.183	0.156	0.141	0.002	-0.092	-0.015	-0.023
	$S_{123}$	$S_{124}$	$S_{125}$	$S_{134}$	$S_{135}$	$S_{145}$	$S_{234}$	$S_{235}$	$S_{245}$	$S_{345}$
A. 3 <sup>rd</sup> order	-5.73e-5	3.35e-4	1.47e-5	6.99e-4	0.003	0.016	0.120	0.001	-0.003	0.012
N. 3 <sup>rd</sup> order	0.003	0.003	0.003	0.005	0.005	0.017	0.119	0.001	-0.003	0.014
	$S_{1234}$	$S_{1235}$	$S_{1245}$	$S_{1345}$	$S_{2345}$					
A. 4 <sup>th</sup> order	0.002	0.003	0.013	-0.005	-0.012					
N. 4 <sup>th</sup> order	0.006	0.009	0.016	0.005	-0.011					
	$S_{12345}$									
A. 5 <sup>th</sup> order	0.005									
N. 5 <sup>th</sup> order	-0.045									
	$S_{T_1}$	$S_{T_2}$	$S_{T_3}$	$S_{T_4}$	$S_{T_5}$					
A. Total Index	0.217	0.431	0.334	0.348	0.336					
N. Total Index	0.211	0.403	0.316	0.332	0.320					

**Table 4.6** Sensitivity indices for total contributions  $S_{r_n}$  constructed using the component functions  $f_{r_n}$  for the shear stress parameters  $\theta_{\sigma_s}$ . The indices correspond to the order specified by  $\theta_{\sigma_s} = [q_{44}, \sigma_{23}^R]$ .

	$S_1$	$S_2$	$S_{12}$	$S_{T_1}$	$S_{T_2}$
Sensitivity	6.812e-5	0.651	0.349	0.349	1.000
Numerical	5.347e-5	0.650	0.350	0.350	1.000

normal and shear continuum stress components  $\sigma_{11}, \sigma_{22}, \sigma_{33}$  and  $\sigma_{23}$  (4.8).

In the algorithm, we set the threshold  $\varepsilon = 10^{-8}$  to represent the square root of machine epsilon. The identifiable parameters correspond to those that have not been removed after the final iteration of the algorithm, when  $|\lambda_1| > \varepsilon$ . As observed in Table 4.7, we determine all parameters  $\theta_p$  to be identifiable. Similarly, in Table 4.8, we conclude that all continuum stress parameters are identifiable. These results are consistent with the global sensitivity analysis for correlated parameters performed in Section 4.4, where we showed that all parameters were influential as specified by the

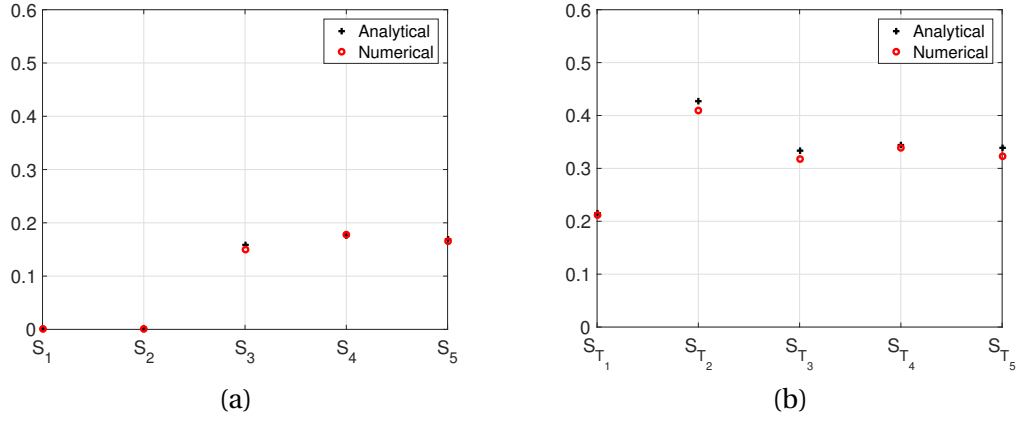


**Figure 4.11** Comparison of analytical and numerical methods to obtain (a) first-order and (b) total sensitivity indices for (4.14).

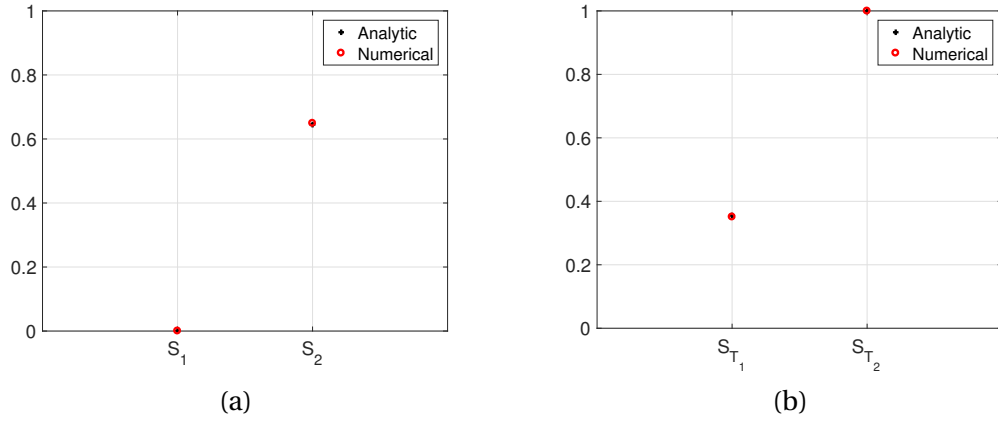


**Figure 4.12** Comparison of analytical and numerical methods to obtain (a) first-order and (b) total sensitivity indices for (4.15).

**Table 4.7** Results from Algorithm 3.3.2, to determine unidentifiable parameters in  $\theta_p$  (4.9) for the polarization energy  $u_p$  (4.3).

Iteration	$ \lambda_1 $	Eigenvector $\Delta\theta_1$ with associated parameters				
		$\alpha_1$	$\alpha_{11}$	$\alpha_{12}$	$\alpha_{111}$	$\alpha_{112}$
1	5.62e-5	1.16e-2	-3.30e-2	-4.31e-1	2.07e-2	9.01e-1
Result: All parameters $\theta_p$ are identifiable since $ \lambda_1  > \epsilon = 10^{-8}$ .						

total sensitivity indices  $S_{T_i}$ .

**Table 4.8** Results from Algorithm 3.2 to determine unidentifiable parameters in  $\theta_\sigma$  (4.10) for the normal and shear stress components  $\sigma_{ns}$  and  $\sigma_s$  (4.8).

		Eigenvector $\Delta\theta_1$ with associated parameters				
Iteration	$ \lambda_1 $	$q_{11}$	$q_{12}$	$\sigma_{11}^R$	$\sigma_{22}^R$	$\sigma_{33}^R$
1	3.67	-9.33e-1	-6.13e-2	-2.48e-2	-5.17e-2	-3.51e-1
Iteration	$ \lambda_1 $	$q_{44}$	$\sigma_{23}^R$			
1	8.99e-1	-9.94e-1	-1.07e-2			
Result: All parameters $\theta_\sigma$ are identifiable since $ \lambda_1  > \epsilon = 10^{-8}$ .						

## Conclusions

In conclusion, the global sensitivity analysis and Fisher information subset selection yield that all the parameters are influential. Broadly, this indicates that the sixth-order Landau polarization energy is necessary to approximate quantum calculations. These results additionally demonstrate that the incorrect assumption of uniformly and independently distributed parameters may yield incorrect interpretations about parameter sensitivity.

## CHAPTER

# 5

## POLYDOMAIN ENERGY MODELS

As stated in Chapter 2, domain walls form in ferroelectric materials as an energy minimization mechanism in response to the solid being cooled through the Curie temperature  $T_C$ . Properties of  $180^\circ$  and  $90^\circ$  domain walls are known to significantly influence material phenomena such as domain formation and evolution, in terms of ferroelectric switching mechanisms, as well as other properties such as permittivity, coercive fields and piezoelectric constants [32, 50, 56]. Therefore, the polarization and strain transitions through domain walls, as well as the total domain wall energy, play a significant role in the domain structure evolution of ferroelectric solids.

DFT studies for domain wall width and energy, such as those in [32, 56], highlight the uncertainty in the width and energy parameter values. These studies also highlight the importance of first-principles investigations, in comparison with Landau-Ginzburg continuum theory models. Here the estimation of model parameters often poses a challenge, due to the lack of available analytical and computational experimental data. This motivates a parameter selection and uncertainty analysis of the Ginzburg-Landau free energy functionals, and their corresponding uncertain parameters. We recall that parameters may not be influential, and therefore would need to be fixed in subsequent Bayesian inference and uncertainty propagation.

As defined earlier,  $180^\circ$  domain walls separate domains in which spontaneous polarization and strain are oriented in opposite directions, whereas  $90^\circ$  domain walls separated domains in which spontaneous polarization is oriented in perpendicular directions. In the analysis of Chapter 6, we consider the  $180^\circ$  polydomain structures where polarization switches from negative to positive

polarization as the domain wall is crossed in the  $x_1$  direction. A representative plot of the polydomain structure is presented in Figure 2.6(a). Additionally, in Chapter 7, we consider  $90^\circ$  polydomain structures where polarization transitions through a  $90^\circ$  change in polarization orientation as the domain wall is crossed in the  $x_1$  direction. For analysis convenience, the coordinate system is rotated by  $45^\circ$  to obtain the new system  $(s, r, x_3)$ . The corresponding polydomain structure is presented in Figure 2.6(b). In both Chapter 6 and Chapter 7, we develop polydomain relations modeling domain wall transitions, with polarization as the main independent variable. In these polydomain models, we are primarily focused on free energy as a result of the domain wall interactions, which strongly influence the material properties as described above.

We continue to focus on lead titanate. An approximation for the  $180^\circ$  domain wall energy for  $\text{PbTiO}_3$  has been calculated in other studies via DFT simulations [32], with an approximate value of  $132 \text{ mJ/m}^2$ . In addition, other first-principle investigations studies [56] noted an approximate value of  $50 \text{ mJ/m}^2$  for the total energy associated with the  $90^\circ$  domain wall. The use of DFT simulations to approximate domain wall energy and inform our continuum models, gives rise to uncertainty going from a quantum scale onto a continuum domain. This augments the previous uncertainty regarding parameters values for the relations in the Landau-Ginzburg free energy functionals. In Chapters 6 and 7, we address these challenges by performing parameter subset selection and uncertainty analysis of the additional gradient exchange parameters present in the polydomain energy models. We determine which parameters are most influential in the sense that they directly contribute to the uncertainty in the model responses, and we correspondingly quantify the uncertainty in the influential parameters.

In this chapter, we provide an overview of the stored energy relations used in the models analyzed in later chapters. This includes the overall stored energy model relations of Section 5.1, the derivation of spontaneous polarization and monodomain energy density of Section 5.2, and the introduction of the total domain wall energies we focus on in later chapters in Section 5.3. Additionally, in Section 5.4, we introduce notation for the parameters and associated proposal distributions used in the analysis of  $180^\circ$  and  $90^\circ$  polydomain structures in the coming chapters.

## 5.1 Stored Energy Relations

In our investigation, we use the  $180^\circ$  domain wall energy values in the literature to inform our continuum model. In Chapter 4, we considered the stored energy density for a monodomain structure with the unit cell held fixed. This motivated a residual energy term with extra residual stress parameters. In this case, there is gradient energy that is considered as a result of polarization gradient in the domain walls. Moreover, since we are no longer holding the unit cell fixed, we no longer account for

a residual energy term. The total form of the ferroelectric stored energy density is thus

$$u(\mathbf{P}, \boldsymbol{\varepsilon}, P_{i,j}) = u_M(\boldsymbol{\varepsilon}) + u_P(\mathbf{P}) + u_C(\mathbf{P}, \boldsymbol{\varepsilon}) + u_G(P_{i,j}), \quad (5.1)$$

where

$$\begin{aligned} u_M &= \frac{c_{11}}{2} (\varepsilon_{11}^2 + \varepsilon_{22}^2 + \varepsilon_{33}^2) + c_{12} (\varepsilon_{11} \varepsilon_{22} + \varepsilon_{22} \varepsilon_{33} + \varepsilon_{11} \varepsilon_{33}) \\ &\quad + 2c_{44} (\varepsilon_{12}^2 + \varepsilon_{23}^2 + \varepsilon_{13}^2), \\ u_P &= \alpha_1 (P_1^2 + P_2^2 + P_3^2) + \alpha_{11} (P_1^2 + P_2^2 + P_3^2)^2 \\ &\quad + \alpha_{12} (P_1^2 P_2^2 + P_2^2 P_3^2 + P_1^2 P_3^2) + \alpha_{111} (P_1^6 + P_2^6 + P_3^6) \\ &\quad + \alpha_{112} [P_1^4 (P_2^2 + P_3^2) + P_2^4 (P_1^2 + P_3^2) + P_3^4 (P_1^2 + P_2^2)] \\ &\quad + \alpha_{123} P_1^2 P_2^2 P_3^2, \\ u_C &= -q_{11} (\varepsilon_{11} P_1^2 + \varepsilon_{22} P_2^2 + \varepsilon_{33} P_3^2) \\ &\quad - q_{12} [\varepsilon_{11} (P_2^2 + P_3^2) + \varepsilon_{22} (P_1^2 + P_3^2) + \varepsilon_{33} (P_1^2 + P_2^2)] \\ &\quad - q_{44} (\varepsilon_{12} P_1 P_2 + \varepsilon_{13} P_1 P_2 + \varepsilon_{23} P_2 P_3), \end{aligned}$$

Here, the mechanical energy  $u_M$ , Landau energy  $u_P$  and electrostrictive energy  $u_C$  are defined the same as in the monodomain analysis of Chapter 4.

We define the gradient energy, which quantifies effects along the domain wall, as

$$\begin{aligned} u_G(P_{i,j}) &= \frac{g_{11}}{2} (P_{1,1}^2 + P_{2,2}^2 + P_{3,3}^2) \\ &\quad + g_{12} (P_{1,1} P_{2,2} + P_{1,1} P_{3,3} + P_{2,2} P_{3,3}) \\ &\quad + \frac{g_{44}}{2} [(P_{1,2} + P_{2,1})^2 + (P_{1,3} + P_{3,1})^2 + (P_{2,3} + P_{3,2})^2]. \end{aligned}$$

Here,  $g_{11}$ ,  $g_{12}$  and  $g_{44}$  are the exchange parameters, whereas the polarization gradient is

$$P_{i,j} = \frac{\partial P_i}{\partial x_j}.$$

The governing equations for polarization and polarization gradient with respect to the polydomain structure are derived using Euler's equations

$$\frac{\partial}{\partial x_j} \left( \frac{\partial u}{\partial P_{i,j}} \right) - \frac{\partial u}{\partial P_i} = 0, \quad (i, j = 1, 2, 3). \quad (5.2)$$



Likewise, the stress condition is given by

$$\sigma_{ij,j}^{\text{tot}} = \frac{\partial}{\partial x_j} \left( \frac{\partial u}{\partial \varepsilon_{ij}} \right) = 0. \quad (5.3)$$

We employ these conditions to obtain appropriate values for the independent order parameters polarization  $P$  and strain  $\varepsilon$ , and evaluate the stored energy (5.1).

## 5.2 Monodomain Energy Regions

First, we consider polarization far away from the domain walls, such that its value is equal to spontaneous polarization in the absence of applied electric field, or stress. This encompasses regions in which polarization is uniform, and we must characterize it in order to develop appropriate boundary conditions for our model. Note that the stored energy in these regions is only dependent on temperature, with no effects arising from polarization gradient variations. Thus, this is only governed by Landau energy phenomenological parameters, and electrostrictive and elastic coefficients. Employing the governing equations (5.2) and (5.3), we obtain

$$\frac{\partial u}{\partial P_i} = 0, \quad (5.4)$$

$$\sigma_{ij}^{\text{tot}} = 0. \quad (5.5)$$

We assume that polarization orientation is strictly in the  $x_3$  direction such that the uniform polarization vector is  $\mathbf{P} = (0, 0, \pm P_0)$  in regions away from the  $180^\circ$  domain wall. This assumption yields the system of equations

$$\frac{\partial u}{\partial P_3} = 2\alpha_1^+ P_3 + 4\alpha_{11} P_3^3 + 6\alpha_{111} P_3^5 = 0, \quad (5.6)$$

$$\begin{aligned} \frac{\partial u}{\partial \varepsilon_{11}} &= c_{11} \varepsilon_{11} + c_{12}(\varepsilon_{22} + \varepsilon_{33}) - q_{12} P_3^2 = 0, \\ \frac{\partial u}{\partial \varepsilon_{22}} &= c_{11} \varepsilon_{22} + c_{12}(\varepsilon_{11} + \varepsilon_{33}) - q_{12} P_3^2 = 0, \\ \frac{\partial u}{\partial \varepsilon_{33}} &= c_{11} \varepsilon_{33} + c_{12}(\varepsilon_{11} + \varepsilon_{22}) - q_{11} P_3^2 = 0, \end{aligned} \quad (5.7)$$

where

$$\alpha_1^+ = \alpha_1 - q_{11} \varepsilon_{33} - q_{12}(\varepsilon_{11} + \varepsilon_{22}). \quad (5.8)$$

In the ferroelectric phase for temperatures below the Curie temperature, we obtain the uniform

polarization and strain in the system to be

$$P_3 = P_0 = \left( \frac{-\alpha'_{11} + (\alpha'^2_{11} - 3\alpha_1\alpha_{111})^{1/2}}{3\alpha_{111}} \right)^{1/2}, \quad (5.9)$$

$$\begin{aligned} \varepsilon_{11} = \varepsilon_{22} = \varepsilon_{\perp} &= \frac{P_0^2}{3} \left( \frac{\hat{q}_{11}}{\hat{c}_{11}} - \frac{\hat{q}_{22}}{\hat{c}_{22}} \right), \\ \varepsilon_{33} = \varepsilon_{\parallel} &= \frac{P_0^2}{3} \left( \frac{\hat{q}_{11}}{\hat{c}_{11}} + \frac{2\hat{q}_{22}}{\hat{c}_{22}} \right), \end{aligned} \quad (5.10)$$

where

$$\begin{aligned} \alpha'_{11} &= \alpha_{11} + \frac{4c_{12}q_{11}q_{12} - q_{11}^2(c_{11} + c_{12}) - 2c_{11}q_{12}^2}{2\hat{c}_{11}\hat{c}_{22}}, \\ \hat{c}_{11} &= c_{11} + 2c_{12}, \\ \hat{c}_{22} &= c_{11} - c_{12}, \\ \hat{q}_{11} &= q_{11} + 2q_{12}, \\ \hat{q}_{22} &= q_{11} - q_{12}. \end{aligned} \quad (5.11)$$

In this investigation, we take polarization and strain to change with respect to the  $x_1$  direction, although this direction is arbitrary, and is chosen with respect to the type of considered coordinate system. With this assumption, we then use the uniform polarization and strain to define the monodomain energy  $u_0$ , which is obtained by substituting relations (5.9) and (5.10) into the stored energy equation (5.1). Note that the gradient terms  $P_{i,j}$  are zero in the uniform regions away from the  $180^\circ$  domain walls.

### 5.3 Total Domain Wall Energies

Here, we specify the total domain wall energies we will refer to in Chapters 6 and 7. To start we make the distinction between the polydomain energy density

$$u_\gamma(x) - u_0 \quad (5.12)$$

and the total domain wall energy

$$E_\gamma(\theta_\gamma) = \int_{-\infty}^{\infty} u_\gamma(x) - u_0 \, dx. \quad (5.13)$$

Here,  $\gamma$  denotes either  $180^\circ$  or  $90^\circ$ , whereas  $x$  is an arbitrary spatial variable. Although the polydomain energy density (5.12) is vector-valued and can be used to infer the width and transition region of

the associated domain wall, the total domain wall energy (5.13) is scalar-valued and can be used, for example, to quantify the ease through which new domain walls are introduced as a result of polarization reversal processes [56].

In the polydomain energy density (5.12),  $u_0$  is the monodomain energy obtained by evaluating (5.1) with respect to the spontaneous polarization in the monodomain regions. The subtraction from the energy term  $u_\gamma$  eliminates contributions from regions far away from the domain wall. In the next section, we provide the proposal distribution methodology used for the parameters  $\theta = \theta_\gamma$ , which denote either  $\theta_{180}$  or  $\theta_{90}$ .

## 5.4 Parameters and Distributions

As in Chapter 4, unless otherwise noted, we use  $\theta$  to arbitrarily denote either of the prospective parameters  $\theta_{180}$  or  $\theta_{90}$ , as well as to denote realizations of the random variable  $\Theta$ . In addition, we use  $\theta_i$  to denote the  $i^{th}$  parameter in  $\theta_{180}$  or  $\theta_{90}$ .

As stated previously, the available data for the 180° and 90° total domain wall energies are reported to be  $E_{180^\circ}^* = 132 \text{ mJ/m}^2$  and  $E_{90^\circ}^* = 50 \text{ mJ/m}^2$ , respectively from the studies [32] and [56]. Since both of these values are scalar-valued, we use the characterized uncertainties for the Landau phenomenological parameters and electrostrictive coefficients in Section 4.3. Recall that these values are given in Table 4.2. We determine the nominal values for gradient exchange parameters via least squares optimizations.

In the analysis, we propose two cases for the Landau and electrostrictive parameter distributions. First, we construct independent normal density distributions

$$\Theta_i \sim \mathcal{N}(\mu_i, \sigma_i^2), \quad (5.14)$$

where  $\mu_i$  and  $\sigma_i$  are provided in Table 4.2. In the second case, we sample these parameters directly from the chains and densities presented in Figure 4.4 and Figure 4.6.

Lastly, similar to the monodomain continuum model, we take elastic coefficients to be fixed at the nominal values provided in Table 4.1.

## CHAPTER

# 6

# 180° POLYDOMAIN STRUCTURE ANALYSIS

In this chapter, we consider parameter subset selection, and uncertainty analysis and propagation for stored energy models characterizing the transition region of 180° domain walls separating oppositely-oriented domains. We detail the 180° domain wall energy model and provide solution procedures in Section 6.1. In Section 6.2, we employ Bayesian inference to quantify the uncertainty in additional gradient exchange parameters. We use this information to construct appropriate distributions for the parameter subset selection and active subspace methods of Sections 6.3 and 6.4, respectively. We verify the results of parameter subset selection and activity scores derived from the active subspace, by propagating influential parameter uncertainties, while fixing non-influential parameters, on the model, in Section 6.5. We derive the model and solution procedures next.

### 6.1 180° Domain Wall Energy Model

We fix the position of the 180° domain wall at  $x_1 = 0$ , so the polarization vector is characterized by

$$\mathbf{P} = (0, 0, P_3(x_1)). \quad (6.1)$$

Domains in which polarization is oriented in opposite directions are separated by the 180° domain walls. In the uniform region, the material exhibits a spontaneous polarization and we obtain the boundary conditions

$$\begin{aligned}\lim_{x_1 \rightarrow \pm\infty} \mathbf{P} &= (0, 0, \pm P_0), \\ \lim_{x_1 \rightarrow \pm\infty} \sigma_{ij}^{\text{tot}}(x_1) &= 0, \quad ij = 11, 22, 33, \\ \lim_{x_1 \rightarrow \pm\infty} \sigma_{ij}^{\text{tot}}(x_1) &= 0, \quad ij = 23, 13, 12,\end{aligned}\tag{6.2}$$

for polarization and stress.

Employment of the equilibrium conditions (5.2) and (5.3) yields the differential equation

$$\frac{\partial}{\partial x_1} \left( \frac{\partial u}{\partial P_{3,1}} \right)_1 - \frac{\partial u}{\partial P_3} = 0,$$

which implies that

$$2\alpha_1^+ P_3 + 4\alpha_{11} P_3^3 + 6\alpha_{111} P_3^5 - g_{44} P_{3,1} = 0.\tag{6.3}$$

Likewise, conditions (5.3) and (6.2) yield the differential equation governing strain

$$\sigma_{11,1} = 0 = c_{11} \varepsilon_{11,1} + c_{12} (\varepsilon_{22,1} + \varepsilon_{33,1}) - 2q_{12} P_3 P_{3,1}.\tag{6.4}$$

Polarization and strain solutions for the system (6.3)-(6.4) are used to obtain the energy surface  $u_{180}$ , which quantifies effects with respect to the domain wall. This is performed in the same manner as the monodomain energy surface  $u_0$ , by substituting into the polydomain stored energy (5.1). We obtain the total energy associated with the 180° domain wall by taking the difference between  $u_{180}$  and  $u_0$ , while integrating through the  $x_1$  domain. Hence, we obtain the relation

$$E_{180^\circ}(\theta_{180}) = \int_{-\infty}^{\infty} (u_{180} - u_0) dx_1,\tag{6.5}$$

where the unknown governing input parameters are

$$\theta_{180} = [\alpha_1, \alpha_{11}, \alpha_{111}, q_{11}, q_{12}, g_{44}].\tag{6.6}$$

For the rest of the analysis, we use the nominal values for the Landau energy and electrostrictive energy parameters, obtained from the monodomain analysis presented in Section 4.3, to define a mean response for  $E_{180}$ . Previous computational DFT simulations performed by Meyer and Vanderbilt [32] are used to inform a least-squares approximation to obtain an initial estimate for the

exchange parameter  $g_{44}$ . In the next section we present solutions for the  $180^\circ$  domain wall model system.

### 6.1.1 Model Solution Procedure

The differential equation (6.3) has a kink solution [11],

$$P_3(x_1) = \frac{P_0 \sinh(x_1/\xi_{180^\circ})}{[A + \sinh^2(x_1/\xi_{180^\circ})]^{1/2}}, \quad (6.7)$$

for polarization  $P_3(x_1)$  that satisfies the boundary conditions (6.2). Here, the additional parameters are defined by

$$\xi_{180^\circ} = \frac{\sqrt{g_{44}}}{P_0(6\alpha_{111}P_0^2 + 2\alpha_{11}^+)^{1/2}}, \quad (6.8)$$

$$A = \frac{3\alpha_{111}P_0^2 + \alpha_{11}}{2\alpha_{111}P_0^2 + \alpha_{11}}. \quad (6.9)$$

This solution for polarization  $P_3$  is differentiated with respect to  $x_1$  and substituted in the equilibrium condition for stress (5.3) to yield the strain component

$$\varepsilon_{11}(x_1) = \varepsilon_\perp - \frac{q_{12}}{c_{11}} \frac{P_0^2}{1 + A^{-1} \sinh^2(x_1/\xi_{180^\circ})}. \quad (6.10)$$

Note that with the assumption of polarization distortion only in the  $x_1$  direction as a result of the domain wall, the other strain components are the same as in the monodomain case. Hence, we again define

$$\begin{aligned} \varepsilon_{22} &= \varepsilon_\perp, \\ \varepsilon_{33} &= \varepsilon_\parallel. \end{aligned}$$

Note that not solving the system defined by (6.3) and (6.4) simultaneously, raises questions about momentum effects due to change in strain. This motivates the implementation of a simultaneous numerical solution to the  $180^\circ$  domain wall model for polarization and strain. For comparison, we use a numerical finite-difference approach proposed by Miles et al. [34] with an addition of a first-order polarization time-dependent term for conversion to a steady-state solution. The new system is

$$\omega \frac{\partial P_3}{\partial t} = 2\alpha_1^+ P_3 + 4\alpha_{11} P_3^3 + 6\alpha_{111} P_3^5 - g_{44} \frac{\partial^2 P_3}{\partial x_1^2}, \quad (6.11)$$

where  $\omega$  is an appropriate damping parameter. The system reaches a steady state solution via an

iterative method when

$$\frac{\partial P_3}{\partial t} = 0.$$

Note that in (6.4), the  $\varepsilon_{22}$  and  $\varepsilon_{33}$  terms vanish since we assume they are uniform with respect to  $x_1$ . In terms of material displacement in the  $x_1$  direction  $v_1$ , this yields the differential equation

$$\omega \frac{\partial v_1}{\partial t} = c_{11} \frac{\partial^2 v_1}{\partial x_1^2} - 2q_{12}P_3 \frac{\partial P_3}{\partial x_1}, \quad (6.12)$$

for

$$\varepsilon_{11} = \frac{\partial v_1}{\partial x_1}.$$

For the numerical scheme, we use an implicit iterative method with temporal and spatial indices. We approximate the first- and second-order spatial derivatives using central difference approximations. For example, letting  $z$  represent  $\varepsilon_{11}$  and  $v$  represent  $v_1$ , each strain iterative solution is approximated by

$$z_j^n \approx \frac{v_{j+1}^n - v_{j-1}^n}{2\Delta x}.$$

For convenience, we let the subscript  $j$  represent the spatial index, whereas the superscript  $n$  represents the temporal index. Representing polarization  $P_3$  by  $y$ , yields the discretized form

$$\begin{aligned} \omega \frac{y_j^n - y_j^{n-1}}{\Delta t} \approx & g_{44} \frac{y_{j+1}^n - 2y_j^n + y_{j-1}^n}{\Delta x^2} - 2(\alpha_1 - q_{11}\varepsilon_{33} - q_{12}\varepsilon_{22})y_j^n \\ & + 2q_{12}z_j^{n-1}y_j^{n-1} - 4\alpha_{11}(y_j^{n-1})^3 - 6\alpha_{111}(y_j^{n-1})^5 \end{aligned} \quad (6.13)$$

of the differential equation (6.11), with respect to polarization  $P_3$ . Likewise, we obtain the discretized form of the displacement and strain differential equation,

$$\omega \frac{v_j^n - v_j^{n-1}}{\Delta t} \approx c_{11} \frac{v_{j+1}^n - 2v_j^n + v_{j-1}^n}{\Delta x^2} - 2q_{12}y_j^{n-1} \frac{y_{j+1}^{n-1} - y_{j-1}^{n-1}}{\Delta x}. \quad (6.14)$$

The discretized forms yield two tridiagonal matrix systems. Thus we solve each system iteratively using the Thomas algorithm, while appropriately satisfying the boundary conditions (6.2). This method requires appropriate initial conditions satisfying the boundary conditions and distortion with respect to the domain wall. We choose a hyperbolic tangent function represent the initial condition for polarization  $P_3$ , whereas we choose a line for the strain  $\varepsilon_{11}$ .

We additionally solve the system defined by (6.3) and (6.4) using MATLAB's boundary value problem solver `bvp4c.m`. We define the initial conditions for this method using the function `bvpinit.m`. While this method does not require a time-dependent term, its convergence is slower than the finite-difference approach where we adopt an adaptive step size  $\Delta x$  depending on the parameter

values  $\theta_{180}$ .

### 6.1.2 Implementation

After solving the differential equations for polarization and strain, we evaluate the resulting energy density  $u_{180} - u_0$  and the total energy associated with the  $180^\circ$  domain wall as defined in (6.5). Note that the parameter values for  $\alpha_1, \alpha_{11}, \alpha_{111}, q_{11}, q_{12}$  used in the solution and evaluation are obtained from the monodomain analysis of Chapter 4. We obtain an initial nominal value for the gradient exchange parameter by employing least-squares regression. This is achieved by first simulating data with respect to the reported value of  $E_{180^\circ}^* = 132 \text{ mJ/m}^2$  [32], such that

$$E_{180^\circ}^{data}(i) = E_{180^\circ}^* + \varepsilon_i. \quad (6.15)$$

Here, the measurements  $E_{180^\circ}^{data}(i)$  are obtained by adding random noise where  $\varepsilon_i \sim \mathcal{N}(0, \sigma^2)$ . We assume that  $\sigma = 0.01 E_{180^\circ}^*$ , let  $\theta_{180}^{MD} = [\alpha_1, \alpha_{11}, \alpha_{111}, q_{11}, q_{12}]$  represent the nominal values from Table 4.2 and find a nominal value for  $g_{44}$  by minimizing the cost function

$$J(g_{44}) = \sum_{i=1}^K [E_{180^\circ}^{data}(i) - E_{180^\circ}(\theta_{180}^{MD}, g_{44})]. \quad (6.16)$$

to obtain a value of  $g_{44} = 6.00 \times 10^{-6} \frac{\text{mV} \cdot \text{mm}^3}{\mu\text{C}}$ . We compile the set of parameters used in the  $180^\circ$  domain wall energy evaluation in Table 6.1.

Note that the unit system is changed for this model with respect to the monodomain analysis of Chapter 4 due to the vast difference in parameter magnitudes when employing single domain units. For example with voltage as  $MV$  or  $GV$ , we would have obtained a value of  $g_{44} \sim 10^{-18} MV \cdot m^3/C$ , which is below machine epsilon. The new unit system employed here is presented in Table 6.2

In Figure 6.1, we present the solutions for polarization  $P_3(x_1)$ ,  $P_{3,1}(x_1)$ ,  $\varepsilon_{11}(x_1)$ , and  $u_{180} - u_0$  using the three methods defined in this section. All three methods are in close agreement, verifying the solution. Nonetheless, the `bvp4c.m` solver is the slowest solution procedure, and furthermore we do not use it in further realizations of the model in Sections 6.2-6.5. Since the analytic solution ignores a

**Table 6.1** List of parameters used in solution and evaluation of the domain wall energy (6.5), along with corresponding units. The parameters  $\theta_{180}^{MD}$  are appropriately scaled from Table 4.2 to reflect the new unit system employed here.

Parameter	$\alpha_1$	$\alpha_{11}$	$\alpha_{111}$	$q_{11}$	$q_{12}$	$g_{44}$
Units	$\frac{\text{mV} \cdot \text{mm}}{\mu\text{C}}$	$\frac{\text{mV} \cdot \text{mm}^5}{\mu\text{C}^3}$	$\frac{\text{mV} \cdot \text{mm}^9}{\mu\text{C}^5}$	$\frac{\text{mV} \cdot \text{mm}}{\mu\text{C}}$	$\frac{\text{mV} \cdot \text{mm}}{\mu\text{C}}$	$\frac{\text{mV} \cdot \text{mm}^3}{\mu\text{C}}$
Nominal Value	-389.4e+6	761.3e+6	61.46e+6	19.2e+9	3.14e+9	5.73e-6



**Table 6.2** Units of measurement used in the 180° domain wall model for energy, length, charge, and voltage

Measurement	Energy	Length	Charge	Voltage
Units (PD)	nJ/mm <sup>3</sup>	mm	μC	mV

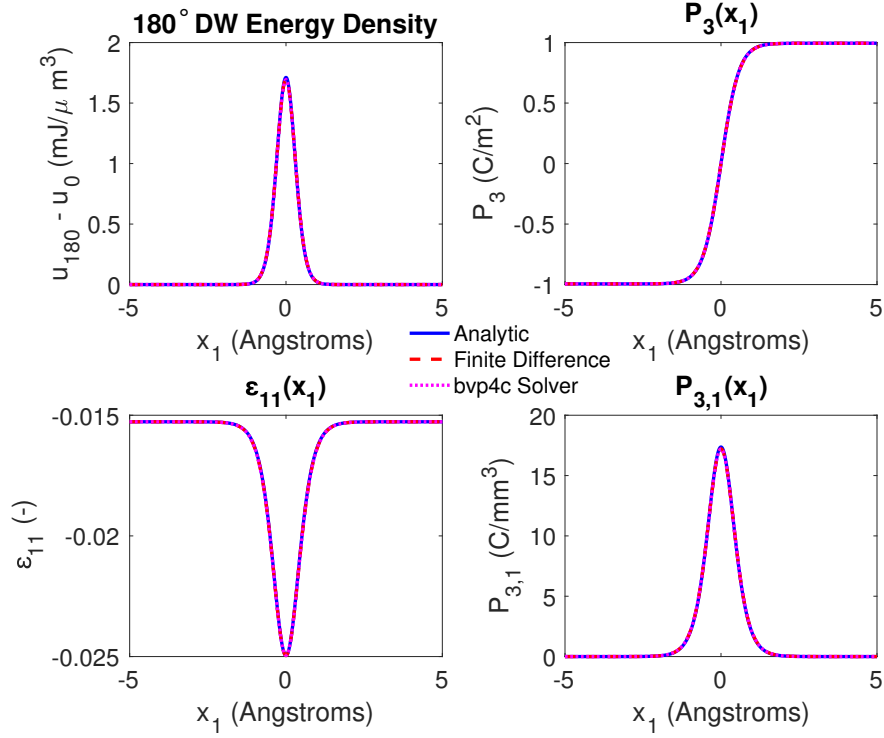


**Figure 6.1** Comparison of analytic, finite difference and MATLAB bvp4c .m solver for solution 180° domain wall energy system. From top left to bottom right, 180° domain wall energy density solution, polarization  $P_3$  in the  $x_1$  direction, strain  $\epsilon_{11}$  in the  $x_1$  direction, and polarization gradient in the  $x_1$  direction as we cross the 180° domain wall.

simultaneous solution of polarization and strain, we also do not use this implementation in further realizations of the model. Therefore, we use the finite-difference procedure in the analyses of the upcoming sections.

## 6.2 Bayesian Inference

Typically, parameter subset selection is performed before model calibration, in order to determine non-influential parameters which may be fixed in Bayesian inference. In this case, the only additional parameter for the 180° domain wall energy with respect to the monodomain continuum

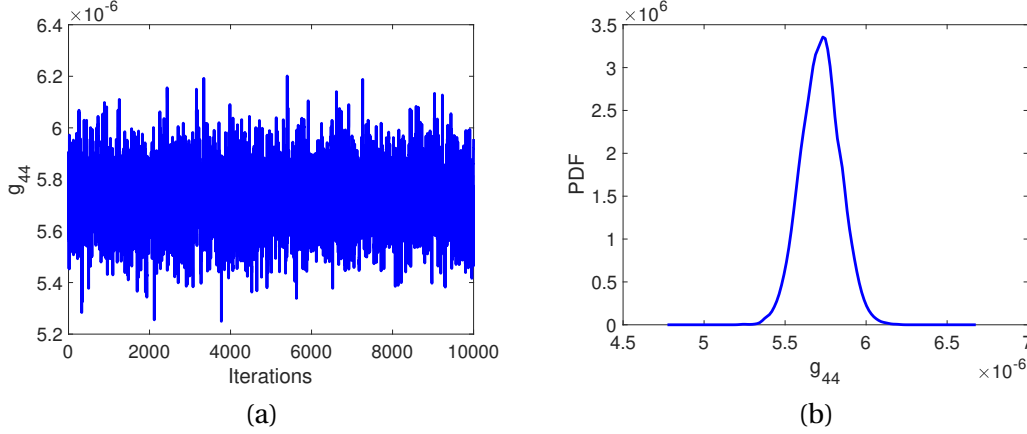


**Figure 6.2** (a) Chain of accepted values and (b) kernel density estimation (kde) for the parameter  $g_{44}$  obtained from the Bayesian uncertainty analysis with respect to  $E_{180^\circ}$ .

model analysis of Section 4.1, is the exchange parameter  $g_{44}$ . To more accurately construct a parameter distribution for  $g_{44}$  from which we can sample for the parameter subset selection and active subspace techniques of Section 6.3 and 6.4, we employ Bayesian inference to identify a corresponding mean value from an obtained posterior distribution. We note that one could additionally employ frequentist inference, which is computationally more efficient, to obtain a distribution.

To quantify the uncertainty in  $g_{44}$ , we employ the delayed rejection adaptive metropolis (DRAM) algorithm, given in Algorithm A.0.1 and detailed in Section 3.4. We generate synthetic data  $E_{180^\circ}^{data}(i)$  for the total  $180^\circ$  domain wall energy by employing the relation (6.15), as described in Section 6.1.2. We let  $N = 50$  specify the total number of synthetic observations.

In Figure 6.2, we present the chain and posterior density obtained from the implementation of the DRAM algorithm. Here, we used a uniform prior for  $g_{44}$ , along with 10,000 accepted value iterations. We obtain a mean value  $\mu_{g_{44}} = 5.73\text{e-}6 \text{ mV}\cdot\text{mm}^3/\mu\text{C}$ , along with a standard deviation  $\sigma_{g_{44}} = 1.21\text{e-}7 \text{ mV}\cdot\text{mm}^3/\mu\text{C}$  from the chain in Figure 6.2(a). In Sections 6.3 and 6.4, we use a Gaussian distribution constructed based on these values, for the parameter subset selection and active subspace analysis.

### 6.3 Parameter Subset Selection

In this section, we present the results of the parameter subset selection techniques introduced in Section 3.3 applied to the  $180^\circ$  domain wall model. We intend to reduce the computational cost of future Bayesian model calibration and uncertainty propagation by determining the most influential set of parameters while isolating the non-influential ones, which may be fixed.

We consider the Fisher information matrix-based methodology developed in Section 3.3.2, with

**Table 6.3** Results from Algorithm 3.3.2 with the global sensitivity matrix (3.44) to determine noninfluential parameters in  $\theta_{180}$  (6.6) for the  $180^\circ$  domain wall energy  $E_{180^\circ}$  (6.5).

Iteration	$ \lambda_1 $	Eigenvector $\Delta\theta_1$ with corresponding parameters					
		$\alpha_1$	$\alpha_{11}$	$\alpha_{111}$	$q_{11}$	$q_{12}$	$g_{44}$
1	6.22e-13	8.01e-2	-8.20e-2	1.13e-2	-3.64e-1	-9.24e-1	-9.14e-3
2	7.55e-12	9.33e-1	-3.08e-1	8.64e-2	-6.01e-2	—	-1.51e-1
3	2.62e-9	—	-5.43e-1	2.01e-2	-7.12e-1	—	-4.45e-1
Result: The parameters $\alpha_1$ and $q_{12}$ are not influential.							

the construction of the global sensitivity analysis matrix  $\mathbf{S}^*$ , constructed from the entries (3.46). Here, we use the nominal values provided in Table 6.1, along with the standard deviations in Table 4.2, to construct the multivariate normal distribution, as defined in (5.14).

Using a total of 500 realizations of the sensitivity entries  $S_{ij}$  in the construction of the global sensitivity matrix for Algorithm 3.3.2, we obtained the results presented in Table 6.3. We find that the most influential parameters in the  $180^\circ$  domain wall energy model are  $\alpha_{11}$ ,  $\alpha_{111}$ ,  $q_{11}$  and  $g_{44}$  when using a threshold of  $\varepsilon = 1e-9$ . These results highlight the importance of the higher-order Landau phenomenological parameters in the  $180^\circ$  polarization transition through the domain wall. The results for  $q_{11}$  also illustrate its electromechanical coupling influence on the  $180^\circ$  domain wall energy.

## 6.4 Active Subspace Construction

To verify the results of Section 6.3, in this section we construct activity scores based on an active subspace analysis for the model  $E_{180^\circ}$  (6.5). We construct the active subspace employing the methodology in Section 3.4.2. To determine the dimension of the active subspace, we implement several dimension assessment techniques. We use the dimension to identify the active variables, and compute activity scores, which provide an additional measure of global parameter sensitivity.

We start by constructing the gradient matrix  $\mathbf{G}$  (3.58), employing Algorithm 3.4.1. We assume uniform and normal distributions of the type (3.47) and (3.49), centered around the nominal values in Table 6.1, to sample the parameters. Following 10,000 iterations of the algorithm, a singular value decomposition  $\mathbf{G} = \mathbf{W}\Sigma\mathbf{V}^T$  then yields the singular values presented in Figure 6.3. Based on the gap-based criteria for determining the dimension of the active subspace, we presume there to be a one- or two-dimensional active subspace. We proceed with the other dimension selection methods detailed in Section 3.4.2 to accurately determine the dimension of the active subspace.

As detailed in Constantine [8], active subspaces are often low-dimensional, since the output varies dominantly in one or two directions dictated by linear combinations of the model parameters in the input space. Therefore, we construct response surfaces based on one-, two- and three-

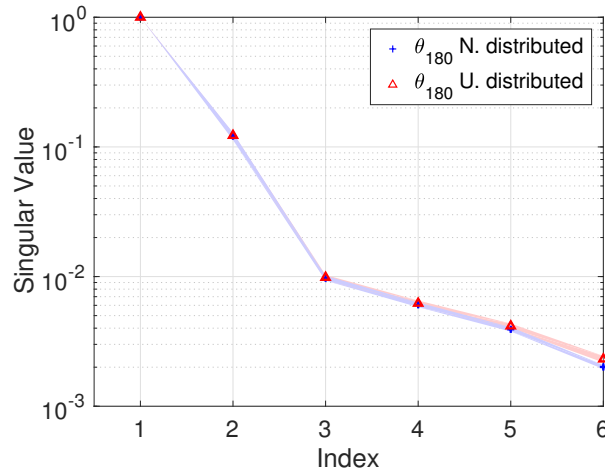


**Figure 6.3** Singular values obtained from the active subspace determination for  $E_{180^\circ}$  assuming uniform (3.47) and normal (3.49) distributions for parameters  $\theta_{180}$ . The shading indicates two standard deviations from the sample mean.

**Table 6.4** Mean relative errors (MRE) for response surfaces considering 1-, 2-, and 3-dimensional active subspaces for the mode response  $E_{180^\circ}$ .

Dimension	1	2	3
MRE	0.0244	0.0116	0.0116

dimensional active subspaces and compare the reduction in the mean relative errors (MRE) as motivated in Section 3.4.3. We plot the one- and two-dimensional-based response surfaces in Figure 6.4, and present the corresponding MRE in Table 6.4. The dimension of the active subspace based on this criteria is indicated when the reduction in the MRE is less than one order of magnitude. As is observed from Table 6.4, this method implies that the dimension of the active subspace is equal to one.

The final method used for dimension selection is principal component analysis (PCA). Implementing Algorithm 3.4.3, with a tolerance  $t^* = 0.95$ , yields a one-dimensional active subspace, consistent with the other dimension selection methods above. Note that we determine this based on the samples used to construct the gradient matrix  $\mathbf{G}$ , as detailed in Algorithm 3.4.3.

## Activity Scores

Activity scores provide an additional global sensitivity metric by exploiting information from the active variables defined in Section 3.4.2. This method ranks the relative influence of the parameters on the model output. We compare the computation of the activity scores based on one- and two-

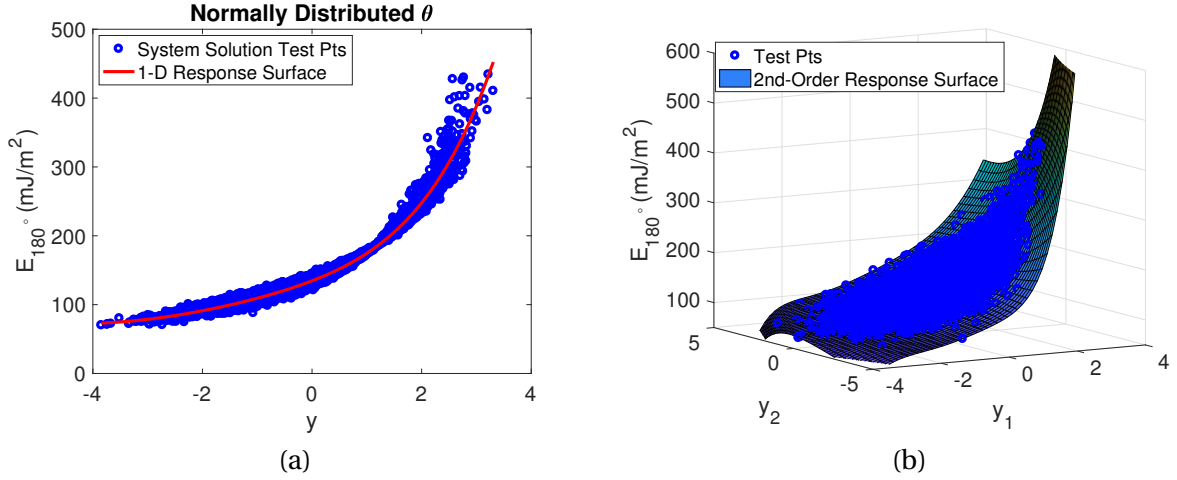


**Figure 6.4** Response surfaces for  $E_{180^\circ}$  constructed based on a (a) one-dimensional and (b) two-dimensional active subspace.

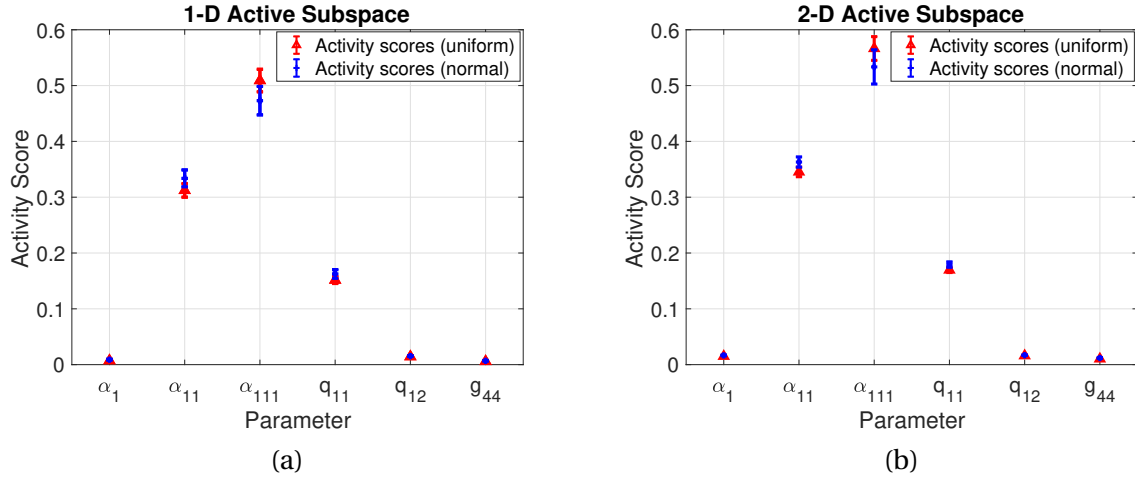


**Figure 6.5** Activity scores for the model response  $E_{180^\circ}$  assuming uniform (3.47) and normal (3.49) parameter distributions, and a (a) one-dimensional and (b) two-dimensional active subspace.

dimensional active subspaces, and normal and uniform distributions, to obtain the results plotted in Figure 6.5.

Based on the activity scores, the parameters  $\alpha_{11}$ ,  $\alpha_{111}$  and  $q_{11}$  are most influential. The significant Landau energy parameter results are in agreement with the parameter subset selection results from Section 6.3. In contrast with the parameter subset selection, the gradient exchange parameter appears less influential here. However, we note that the active subspace analysis considers the total

domain wall energy  $E_{180^\circ}$  (6.5) or (5.13), whereas the parameter subset selection analysis considers the vector valued energy density  $u_{180}(x_1) - u_0$  (5.12), presented in Figure 6.1. Recall the distinction between the two relations was made in Section 5.3. Thus, the contribution of the gradient exchange parameter is more apparent in the domain wall energy density, as compared with the response  $E_{180^\circ}$ . Incorporating the results of both the parameter subset selection of Section 6.3, as well as the activity scores given here, we conclude that the gradient exchange parameter  $g_{44}$  is significant, to propagate its uncertainty on the model output, as detailed in the Section 6.5 uncertainty propagation analysis.

## 6.5 Uncertainty Propagation

From the results of Sections 6.3 and 6.4, we obtain the sensitive parameters

$$\theta_{180}^{sens} = [\alpha_{11}, \alpha_{111}, q_{11}, g_{44}]. \quad (6.17)$$

In this section we compare the results of uncertainty propagation on the energy density  $u_{180}(x_1) - u_0$  when only sampling the sensitive parameters (6.17), with the case where we sample all parameters  $\theta_{180}$  (6.6).

As detailed in Section 6.4, we consider two cases for the random sampling of the parameters. In the first case, we consider the parameters to be normally distributed with the distributions of the type (5.14). The associated nominal values and standard deviations are provided in Table 4.2 for the Landau and electrostrictive energy parameters, whereas the nominal value and standard deviation for  $g_{44}$  were obtained from the Bayesian inference in Section 6.2. In the second scenario, we randomly sample all parameters from the chains given in Figures 4.4 and 6.2(a). This permits the evaluation of the energy densities incorporating the strong correlation in the Landau energy parameters with respect to the monodomain analysis of Section 4.3, and verify if the parameter selection results are independent of the choice of parameter distribution.

Using 500 realizations of the energy density  $u_{180}(x_1) - u_0$ , we construct and plot 50%, 90%, 95% and 99% credible intervals in Figure 6.6. In Figure 6.6(a), we plot the results, when we all parameters  $\theta_{180}$ , whereas in Figure 6.6(b), we plot the results, when we only sample the sensitive parameters  $\theta_{180}^{sens}$ , while fixing all other parameters, for uncertainty propagation. From a qualitative perspective, we observe that the intervals are almost identical.

To obtain a better qualitative measure of the proximity between the credible intervals in Figures 6.6(a) and (b), we consider the “peak values” (at  $x_1 = 0$ ). We take 40 simulation and subtract the  $\theta_{180}^{sens}$  uncertainty propagation-based peaks from the ones associated with the  $\theta_{180}$  uncertainty propagation, to obtain the peak residuals plotted in Figure 6.7. Additionally, we plot the peak value distributions for both parameter sampling scenarios discussed earlier in Figure 6.8. From a qualitative point of view, the distributions are almost identical.

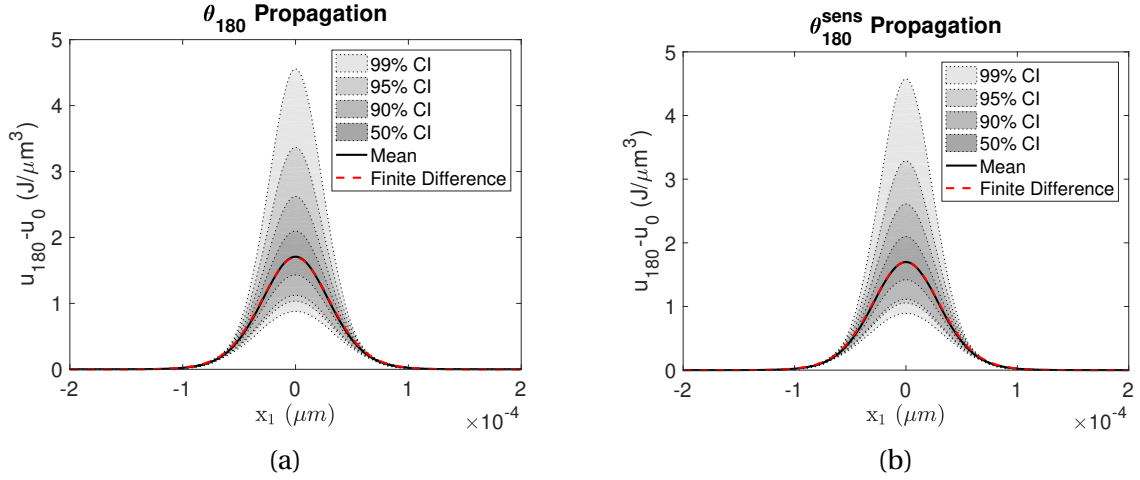


**Figure 6.6** Uncertainty propagation of the (a)  $\theta_{180}$  model inputs and (b)  $\theta_{180}^{sens}$  influential inputs on the energy density  $u_{180}(x_1) - u_0$ .

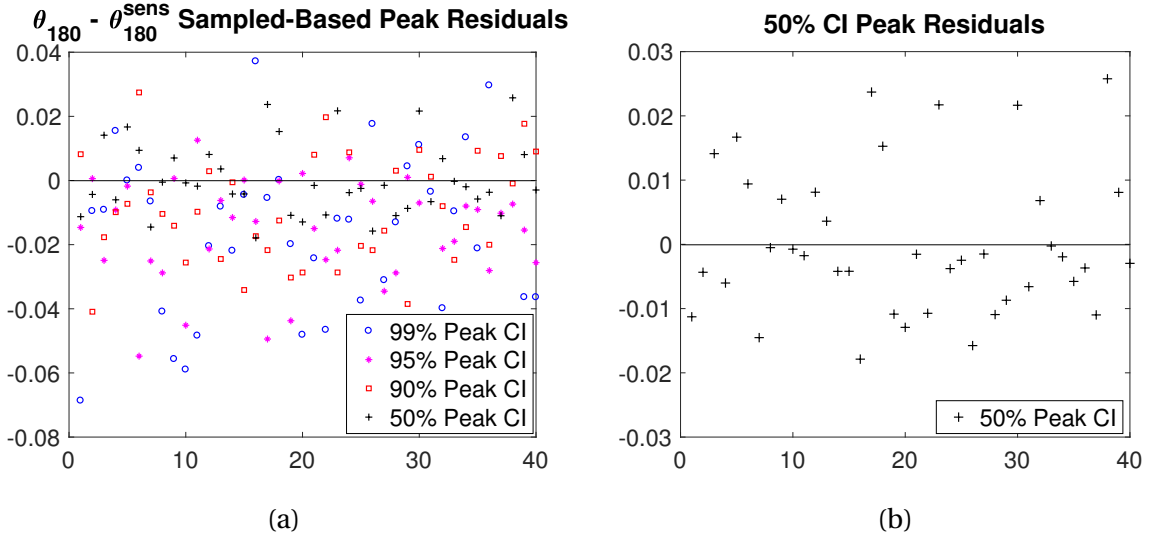


**Figure 6.7** (a) Peak residuals obtained for the different credible intervals (CI) peaks of Figure 6.6(a) subtracted by the peaks of Figure 6.6(b). (b) 50% CI peak residuals obtained from the 50% CI peaks of Figure 6.6(a) subtracted by the peaks of Figure 6.6(b).

To quantitatively measure the distance between the statistical observations of Figure 6.8, we employ energy statistics, detailed in Section 3.6.2. We test the null hypothesis  $H_0 : F_{180} = F_{180}^{sens}$  that the two densities are equal against the alternate hypothesis  $H_1 : F_{180} \neq F_{180}^{sens}$ . For  $M = 499$ ,  $n_1 = n_2 = 4,000$ , we obtain the energy test statistic  $T_{n_1, n_2} = 0.2413$ . We construct the energy statistic

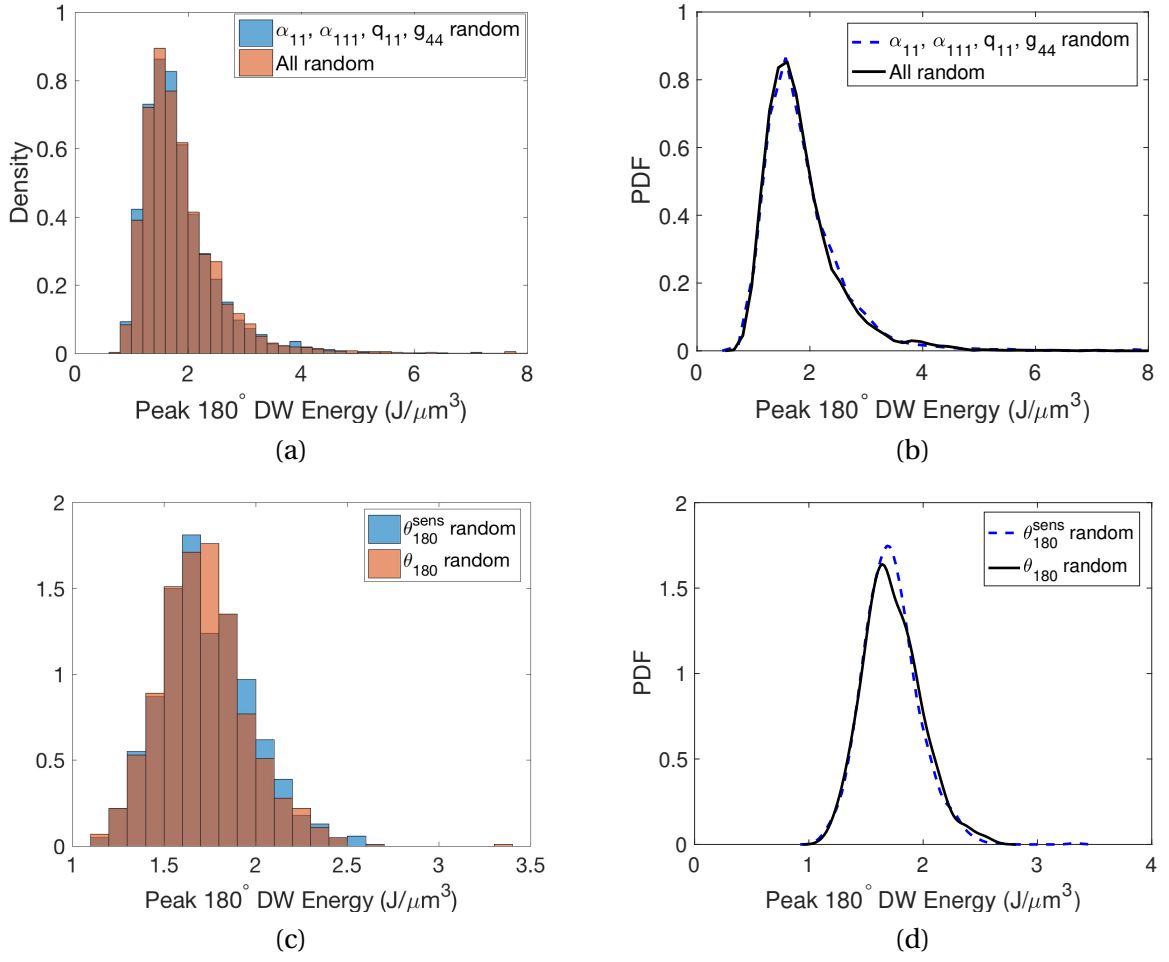


**Figure 6.8** (a) Histogram and (b) probability density of the 180° domain wall energy  $u_{180}(0) - u_0$  distributions with respect to the case where the uncertainties of all parameters  $\theta_{180}$  are propagated, as compared with the case where only the uncertainties of parameters  $\theta_{180}^{sens}$  are propagated. In (c) and (d) parameters were sampled directly from the chains in the monodomain analysis of Section 4.3 and [33], and the uncertainty analysis of Section 6.2.

replicates in the manner detailed in Section 3.6.2, to obtain the results presented in Figure 6.9. We take confidence levels  $\alpha = 0.05, 0.10$ , and present their associated values in Table 6.5. The energy test statistic is clearly below the critical values specified by the confidence levels  $\alpha$ . As a result, we cannot reject the null hypothesis that the two distributions are equal, verifying the close proximity of the credible intervals, based on  $\theta_{180}^{sens}$  being the most sensitive parameters in the 180° domain wall energy model.



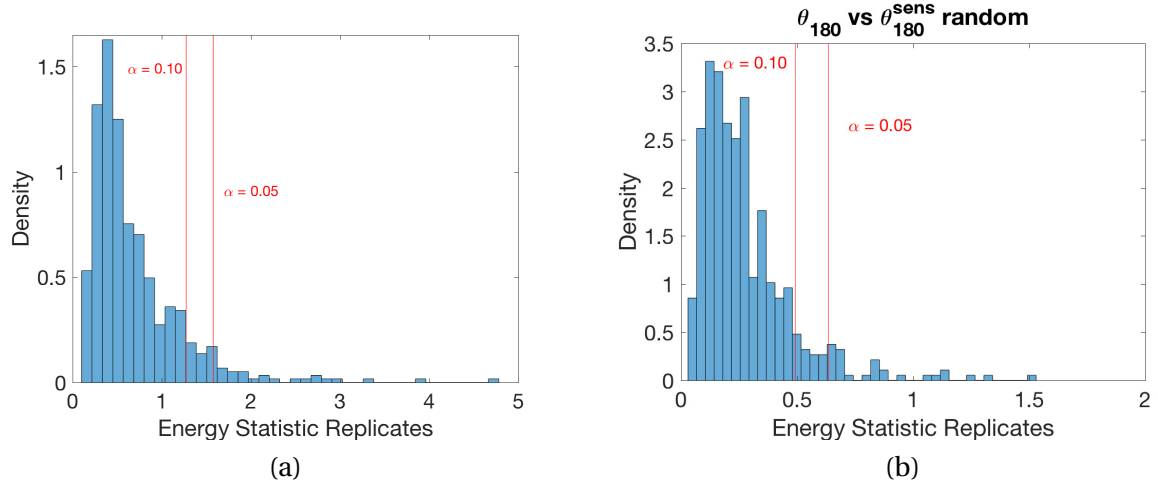


**Figure 6.9** Energy test statistic replicates for the analysis of the  $u_{180}(0) - u_0$  distribution considering a (a) normal distribution and (b) direct sampling from the monodomain chains of [33] for the Landau and electrostrictive parameters in  $\theta_{180}$ .

**Table 6.5** Energy test statistic and critical values for  $\alpha = 0.05$ ,  $\alpha = 0.10$  with respect to normally distributed  $\theta_{180}$  (normal) and sampled from the chains in the single domain (MD) analysis of [33].

Density Peak Samples (normal)	Test Statistic	Critical Value ( $\alpha = 0.05$ )	Critical Value ( $\alpha = 0.10$ )
$\theta_{180}$ versus $\theta_{180}^{sens}$ sampled	0.2413	1.5761	1.2728
Density Peak Samples (MD)	Test Statistic	Critical Value ( $\alpha = 0.05$ )	Critical Value ( $\alpha = 0.10$ )
$\theta_{180}$ versus $\theta_{180}^{sens}$ sampled	0.3428	0.6353	0.4919

## CHAPTER

# 7

## 90° POLYDOMAIN STRUCTURE ANALYSIS

Here we consider 90° domain walls separating domains. In Section 7.1, we detail the 90° domain wall energy model and provide solution frameworks for calculation of the polarization transition and total energy associated with the domain wall. We then determine the most influential gradient energy exchange parameter, and quantify the associated parameter's uncertainty in Sections 7.2 and 7.3, using the techniques detailed in Sections 3.3-3.5. In Section 7.4, we use the active subspace techniques developed in Section 3.4 to construct activity scores, providing a final measure of global sensitivity, to use in determining which parameters to fix in further Bayesian analysis. Lastly, in Section 7.5, we propagate the parameters' uncertainty on the model to determine credible intervals, which measure the model's fit in light of the parameter uncertainties.

### 7.1 90° Domain Wall Energy

The 90° polydomain structure consists of two twined domains whose spontaneous polarizations are perpendicular to each other, separated by a domain wall or boundary. Thus, the polarization vector of interest is  $\mathbf{P} = [P_1(x_1), P_2(x_1), 0]$  with boundary conditions

$$\lim_{x_1 \rightarrow -\infty} \mathbf{P} = (P_0, 0, 0), \quad \lim_{x_1 \rightarrow +\infty} \mathbf{P} = (0, P_0, 0), \quad (7.1)$$

where  $P_0$  is the spontaneous polarization. Note that this analysis is analogous with the inclusion of  $P_3$ .

We rotate the  $x_1$ - $x_2$  plane counterclockwise by  $45^\circ$  to facilitate the analysis, considering a polarization vector

$$\mathbf{P} = (P_s(s), P_r(s), 0). \quad (7.2)$$

This corresponds to the new coordinate system  $(s, r, x_3)$ , obtained by employing the rotation matrix

$$R = \begin{bmatrix} \cos(45^\circ) & -\sin(45^\circ) & 0 \\ \sin(45^\circ) & \cos(45^\circ) & 0 \\ 0 & 0 & 1 \end{bmatrix} = \begin{bmatrix} 1/\sqrt{2} & -1/\sqrt{2} & 0 \\ 1/\sqrt{2} & 1/\sqrt{2} & 0 \\ 0 & 0 & 1 \end{bmatrix}, \quad (7.3)$$

where the rotated values for polarization and strain are  $\bar{P} = RP$  and  $\bar{\epsilon} = R\epsilon R^T$ .

The employment of the rotation transformations yields new stored energy terms for the relation (5.1). In the case of the mechanical energy, we obtain

$$\begin{aligned} u_M(\epsilon_{kl}) = & \frac{c_{11}}{2} \left( \epsilon_{33}^2 + 2\epsilon_{sr}^2 + \frac{1}{2}(\epsilon_{rr} + \epsilon_{ss})^2 \right) \\ & + c_{12} \left( \frac{1}{4}(\epsilon_{rr} + \epsilon_{ss})^2 - \epsilon_{sr}^2 + \epsilon_{33}(\epsilon_{rr} + \epsilon_{ss}) \right) \\ & + 2c_{44} \left( \epsilon_{r3}^2 + \epsilon_{s3}^2 + \frac{1}{4}(\epsilon_{rr} - \epsilon_{ss})^2 \right), \end{aligned} \quad (7.4)$$

where  $\epsilon_{kl}$ ,  $k, l = s, r, 3$ , denotes the rotated strains. The Landau energy is

$$\begin{aligned} u_P(P_i) = & \alpha_1 P_r^2 + \alpha_{11}^+ P_r^4 + \alpha'_{111} P_r^6 + \alpha_1 P_s^2 + \alpha_{11}^+ P_s^4 + \alpha'_{111} P_s^6 \\ & + (2\alpha_{11} - \frac{1}{2}\alpha_{12}) P_r^2 P_s^2 + \alpha_{111}^+ (P_r^4 P_s^2 + P_r^2 P_s^4) \end{aligned} \quad (7.5)$$

considering the rotated polarization vector (7.2). Additionally, we obtain the electrostrictive energy

$$\begin{aligned} u_C(P_i, \epsilon_{kl}) = & -q_{11} \left[ \frac{1}{2}(\epsilon_{rr} + \epsilon_{ss})(P_r^2 + P_s^2) + 2\epsilon_{sr} P_r P_s + \epsilon_{33} P_3^2 \right] \\ & - q_{12} \left[ \frac{1}{2}(\epsilon_{rr} + \epsilon_{ss})(P_r^2 + P_s^2) - 2\epsilon_{sr} P_r P_s \right. \\ & \quad \left. + \epsilon_{33}(P_r^2 + P_s^2) \right] \\ & - 2q_{44} \left[ \frac{1}{4}\epsilon_{rr}(P_r^2 - P_s^2) - \frac{1}{4}\epsilon_{ss}(P_r^2 - P_s^2) \right]. \end{aligned} \quad (7.6)$$

Lastly, the gradient energy is

$$u_G(P_{i,j}) = \frac{G_{rs}}{2} P_{r,s}^2 + \frac{G_{ss}}{2} P_{s,s}^2, \quad (7.7)$$

where

$$\begin{aligned} G_{rs} &= \frac{g_{11} - g_{12}}{2}, \\ G_{ss} &= \frac{g_{11} + g_{12} + 2g_{44}}{2}, \end{aligned} \quad (7.8)$$

are new conveniently defined parameters.

Application of the rotation matrix (7.3) also yields the boundary conditions

$$\lim_{s \rightarrow \pm\infty} P_s = \frac{P_0}{\sqrt{2}}, \quad \lim_{s \rightarrow \pm\infty} P_r = \pm \frac{P_0}{\sqrt{2}}, \quad (7.9)$$

and

$$\begin{aligned} \lim_{s \rightarrow \pm\infty} \varepsilon_{rr} &= \lim_{s \rightarrow \pm\infty} \varepsilon_{ss} = \frac{\varepsilon_{\parallel} + \varepsilon_{\perp}}{2}, \\ \lim_{s \rightarrow \pm\infty} \varepsilon_{sr} &= \pm \frac{\varepsilon_{\parallel} - \varepsilon_{\perp}}{2}. \end{aligned} \quad (7.10)$$

We assume no mechanical constraints or shear stresses with respect to the  $x_3$ -direction in the single domain regions as  $s \rightarrow \infty$ . This assumption yields the total stress boundary conditions

$$\begin{aligned} \lim_{s \rightarrow \pm\infty} \sigma_{ij}^{\text{tot}}(s) &= 0 \quad (i, j = r, s, x_3), \\ \sigma_{s3} &= \sigma_{rs} = 0. \end{aligned} \quad (7.11)$$

Additionally, we obtain the constraints

$$\varepsilon_{rr,ss} = \varepsilon_{33,ss} = \varepsilon_{rs,ss} = 0. \quad (7.12)$$

The boundary conditions (7.9)-(7.11), and constraints (7.12) yield the spatially constant strain components

$$\varepsilon_{r3} = \varepsilon_{s3} = 0, \quad \varepsilon_{rr} = \frac{1}{2}(\varepsilon_{\parallel} + \varepsilon_{\perp}), \quad \varepsilon_{33} = \varepsilon_{\perp}. \quad (7.13)$$

The strain equilibrium condition (5.3) and stress boundary conditions (7.11) yield the remaining spatially varying strain components

$$\varepsilon_{sr} = \frac{\hat{q}_{22}}{\hat{c}_{22}} P_s P_r, \quad (7.14)$$

$$\begin{aligned} \varepsilon_{ss} &= -\frac{1}{2}(\varepsilon_{\parallel} + \varepsilon_{\perp}) - \frac{1}{2C_{ss}} \left[ (c_{11} + c_{12})(\varepsilon_{\parallel} + \varepsilon_{\perp}) \right. \\ &\quad \left. + 2c_{12}\varepsilon_{\perp} - (P_s^2 q^* + P_r^2 \bar{q}) \right], \end{aligned} \quad (7.15)$$

which are only polarization dependent. Here,  $C_{ss}$ ,  $q^*$  and  $\bar{q}$  are

$$\begin{aligned} C_{ss} &= \frac{c_{11} + c_{12}}{2} + c_{44}, \\ q^* &= q_{11} - q_{12}, \\ \bar{q} &= q_{11} + q_{12} + q_{44}. \end{aligned}$$

Employing the polarization equilibrium condition (5.2), we obtain the system of differential equations

$$\begin{aligned} G_{rs} P_{r,ss} &= [2\alpha_1 - (q_{11} + q_{12})(\epsilon_{rr} + \epsilon_{ss}) - 2q_{12}\epsilon_{33} \\ &\quad + q_{44}(\epsilon_{ss} - \epsilon_{rr})]P_r + 4\alpha_{11}^+ P_r^3 + 6\alpha_{111}' P_r^5 \\ &\quad + (4\alpha_{11} - \alpha_{12})P_r P_s^2 + 4\alpha_{111}^+ P_r^3 P_s^2 \\ &\quad + 2\alpha_{111}^+ P_r P_s^4 + 2\epsilon_{sr}(q_{11} - q_{12})P_s, \end{aligned} \quad (7.16)$$

and

$$\begin{aligned} G_{ss} P_{s,ss} &= [2\alpha_1 - (q_{11} + q_{12})(\epsilon_{rr} + \epsilon_{ss}) - 2q_{12}\epsilon_{33} \\ &\quad - q_{44}(\epsilon_{ss} - \epsilon_{rr})]P_s + 4\alpha_{11}^+ P_s^3 + 6\alpha_{111}' P_s^5 \\ &\quad + (4\alpha_{11} - \alpha_{12})P_r^2 P_s + 4\alpha_{111}^+ P_r^2 P_s^3 \\ &\quad + 2\alpha_{111}^+ P_r^4 P_s - 2\epsilon_{sr}(q_{11} - q_{12})P_r. \end{aligned} \quad (7.17)$$

modeling the  $90^\circ$  domain wall transition.

We obtain the energy density  $u_{90}$  associated with the entire  $90^\circ$  polydomain structure by substituting appropriate solutions  $P_s(s)$  and  $P_r(s)$  for (7.16)-(7.17), into the energy components (7.4)-(7.7). The energy density associated with the domain wall transition is obtained by evaluating and subtracting the monodomain energy corresponding to the uniform regions  $u_0$ , from the polydomain energy density  $u_{90}$ . Here,  $u_0$  employs the rotated energy terms (7.4)-(7.7). The total  $90^\circ$  domain wall energy is then

$$E_{90^\circ}(\theta_{90}) = \int_{-\infty}^{\infty} (u_{90} - u_0) ds, \quad (7.18)$$

where

$$\theta_{90} = [\alpha_1, \alpha_{11}, \alpha_{12}, \alpha_{111}, \alpha_{112}, q_{11}, q_{12}, q_{44}, g_{11}, g_{12}, g_{44}] \quad (7.19)$$

are the unknown parameters governing the  $90^\circ$  polydomain structure.

### 7.1.1 Model Solution Procedure

We consider two solution procedures for the system defined by (7.16)-(7.17), with the second procedure used for verification. The first solution procedure involves rearranging the equations to produce a root finding problem, that can be solved using MATLAB's `fsolve.m` solver, for example. The second method involves using the `bvp4c.m` MATLAB boundary value problem solver.

The root finding procedure requires the discretized form of (7.16)-(7.17). For notation convenience, we let  $u$  and  $v$  represent  $P_s$  and  $P_r$  respectively. We thus obtain the discretized forms

$$0 = G_{rs} \frac{u_{i+1}^n - 2u_i^n + u_{i-1}^n}{\Delta s^2} - \left( \beta_1 u_i^n + \beta_2 (u_i^{n-1})^3 + \beta_3 (u_i^{n-1})^5 + \beta_4 u_i^{n-1} (v_i^{n-1})^2 \right. \\ \left. + \beta_5 u_i^{n-1} (v_i^{n-1})^4 + \beta_6 (u_i^{n-1})^3 (v_i^{n-1})^2 \right) \quad (7.20)$$

and

$$0 = G_{ss} \frac{v_{i+1}^n - 2v_i^n + v_{i-1}^n}{\Delta s^2} - \left( \gamma_1 v_i^n + \gamma_2 (v_i^{n-1})^3 + \gamma_3 (v_i^{n-1})^5 + \gamma_4 v_i^{n-1} (u_i^{n-1})^2 \right. \\ \left. + \gamma_5 v_i^{n-1} (u_i^{n-1})^4 + \gamma_6 (v_i^{n-1})^3 (u_i^{n-1})^2 \right), \quad (7.21)$$

where  $i = 1, \dots, N-1$ ,

$$\beta_1 = 2\alpha_1 - \bar{\epsilon}(q_{11} + q_{12}) - 2q_{12}\epsilon_{\perp} + \frac{q^*}{2C_{ss}} \left( c_{11}\bar{\epsilon} + c_{12}(\bar{\epsilon} + 2\epsilon_{\perp}) \right), \\ \beta_2 = \left( \bar{\alpha}_{11} - \frac{q^{*2}}{2C_{ss}} \right), \beta_3 = \frac{3}{2}\alpha_{111}^*, \beta_4 = \alpha_{11}^* - \frac{q^*\bar{q}}{2C_{ss}} - 2\frac{\hat{q}_{22}^2}{\hat{c}_{22}}, \\ \beta_5 = \frac{1}{2}\bar{\alpha}_{111}, \beta_6 = \bar{\alpha}_{111},$$

and

$$\gamma_1 = 2\alpha_1 - \bar{\epsilon}(q_{11} + q_{12}) - 2q_{12}\epsilon_{\perp} + \frac{\bar{q}}{2C_{ss}} \left( c_{11}\bar{\epsilon} + c_{12}(\bar{\epsilon} + 2\epsilon_{\perp}) \right), \\ \gamma_2 = \left( \bar{\alpha}_{11} - \frac{\bar{q}^2}{2C_{ss}} \right), \gamma_3 = \beta_3, \gamma_4 = \beta_4, \gamma_5 = \beta_5, \gamma_6 = \beta_6.$$

We illustrate the root finding problem for  $u_i$ . Following (7.9)-(7.10), we let  $u_0, u_N, v_0, v_N$  represent the boundary conditions

$$u_0 = -\frac{P_0}{\sqrt{2}}, \quad u_N = v_0 = v_N = \frac{P_0}{\sqrt{2}}.$$

Relations (7.20)-(7.20) then yield the root finding problem

$$\mathcal{F}(\mathbf{u}) = \mathbf{0}, \quad \mathcal{F} : \mathbb{R}^{N-1} \rightarrow \mathbb{R}^{N-1}, \quad (7.22)$$

where  $\mathbf{u} = [u_1, \dots, u_{N-1}]$  and  $\mathbf{0}$  is an  $N-1 \times 1$  column vector of zeros. The solver `fsolve.m` can now be used to solve this problem, simply by finding the roots of (7.22), through an iterative procedure. To facilitate a solution in a lower number of iterations, we define and input the Jacobian

$$J = \left[ \frac{\partial \mathcal{F}}{\partial u_{i-1}}, \frac{\partial \mathcal{F}}{\partial u_i}, \frac{\partial \mathcal{F}}{\partial u_{i+1}} \right]^T,$$

where

$$\begin{aligned} \frac{\partial \mathcal{F}}{\partial u_{i-1}} &= 1, \\ \frac{\partial \mathcal{F}}{\partial u_i} &= -2 - \frac{\Delta s^2}{G_{rs}} (\beta_1 + 3\beta_2 u_i^2 + 5\beta_3 u_i^4 + \beta_4 v_i^4 + 3\beta_6 u_i^2 v_i^2), \\ \frac{\partial \mathcal{F}}{\partial u_{i+1}} &= 1. \end{aligned} \quad (7.23)$$

We then compare the root finding problem solution with the one obtained using MATLAB's boundary value problem solver `bvp4c.m`.

### 7.1.2 Implementation

We use solution to the system (7.16)-(7.17) to evaluate the total domain wall energy  $E_{90^\circ}(\theta_{90})$  (7.18). Recall that

$$\theta_{90} = [\alpha_1, \alpha_{11}, \alpha_{12}, \alpha_{111}, \alpha_{112}, q_{11}, q_{12}, q_{44}, g_{11}, g_{12}, g_{44}].$$

We fit the model (7.18) to the reported value  $E_{90^\circ}^* = 50$  by determining appropriate nominal values for  $\theta_{90}$ . The parameter values for  $\alpha_1, \alpha_{11}, \alpha_{12}, \alpha_{111}, \alpha_{112}, q_{11}, q_{12}, q_{44}$  are all obtained from Table 4.2 in the monodomain analysis of Chapter 4, whereas the value for  $g_{44}$  is obtained from Table 6.1 in the  $180^\circ$  domain wall energy analysis of Chapter 5.

Additionally, we obtain values for  $g_{11}$  and  $g_{12}$  by employing a least squares optimization with respect to the synthetic data

$$E_{90^\circ}^{data}(i) = E_{90^\circ}^* + \varepsilon_i, \quad (7.24)$$

where  $E_{90^\circ}^* = 50 \text{ mJ/m}^2$  and  $\varepsilon_i \sim \mathcal{N}(0, \sigma^2)$  with  $\sigma = 0.01 E_{90^\circ}^*$ . Letting

$$\theta_{90}^{MD} = [\alpha_1, \alpha_{11}, \alpha_{12}, \alpha_{111}, \alpha_{112}, q_{11}, q_{12}, q_{44}]$$

**Table 7.1** Nominal values for parameters  $\theta_{90}$  with respect to the domain wall model energy model  $E_{90^\circ}(\theta_{90})$ .

$\theta_{90}$	$\alpha_1$	$\alpha_{11}$	$\alpha_{12}$	$\alpha_{111}$	$\alpha_{112}$	$q_{11}$
Nominal Value	-389.4e6	761.1e6	414.1e6	61.46e6	-740.56e6	19.2e9
Units	$\frac{\text{mV}\cdot\text{mm}}{\mu\text{C}}$	$\frac{\text{mV}\cdot\text{mm}^5}{\mu\text{C}^3}$	$\frac{\text{mV}\cdot\text{mm}^5}{\mu\text{C}^3}$	$\frac{\text{mV}\cdot\text{mm}^9}{\mu\text{C}^5}$	$\frac{\text{mV}\cdot\text{mm}^9}{\mu\text{C}^5}$	$\frac{\text{mV}\cdot\text{mm}}{\mu\text{C}}$
$\theta_{90}$	$q_{12}$	$q_{44}$	$g_{11}$	$g_{12}$	$g_{44}$	
Nominal Value	3.14e9	1.40e9	1.65e-5	-2.17e-8	5.73e-6	
Units	$\frac{\text{mV}\cdot\text{mm}}{\mu\text{C}}$	$\frac{\text{mV}\cdot\text{mm}}{\mu\text{C}}$	$\frac{\text{mV}\cdot\text{mm}^3}{\mu\text{C}}$	$\frac{\text{mV}\cdot\text{mm}^3}{\mu\text{C}}$	$\frac{\text{mV}\cdot\text{mm}^3}{\mu\text{C}}$	

represent the respective values from Table 4.2, and  $g_{44}^{180^\circ}$  represent its corresponding value in Table 6.1, we find nominal values for  $g_{11}$  and  $g_{12}$  by minimizing the cost function

$$J(g_{11}, g_{12}) = \sum_{i=1}^K [E_{90^\circ}^{data}(i) - E_{90^\circ}(\theta_{90}^{MD}, g_{44}^{180^\circ}, g_{11}, g_{12})]^2. \quad (7.25)$$

We take initial values for  $g_{11}$  and  $g_{12}$  to be equal to the order exchange parameter  $g_{44}$ . Upon minimization of (7.25), we obtain the nominal values compiled in Table 7.1.

Given the  $\theta_{90}$  nominal values, we evaluate and plot the solutions to the  $90^\circ$  domain wall energy system in Figure 7.1. The `fsolve.m` and `bvp4c.m` implementations are in close agreement, thus verifying the solution. Whereas the two methods yield the same solution, the root finding problem is more efficient for the high number of evaluations needed in the implementation of parameter subset selection techniques and Bayesian uncertainty analysis. Furthermore, we use the `fsolve.m` solver is used in further evaluations of  $E_{90^\circ}^*$  (7.18).

Investigations such as [5, 32] cite the vague parameter assumptions made in Landau-Ginzburg theory analysis of  $90^\circ$  polydomain structures. This poses a parameter uncertainty challenge which we address in Section 7.2 by first determining which gradient exchange parameter is most influential in the sense that its uncertainty is most apportioned to the uncertainty in the  $90^\circ$  domain wall energy response.

## 7.2 Parameter Subset Selection

Here, we implement the parameter subset selection methodology developed in Section 3.3 for the parameters  $\theta_{90}$  in the model  $E_{90^\circ}(\theta_{90})$  (7.18). This involves the construction of the global sensitivity matrix  $\mathbf{S}$  (3.44) to be employed in Algorithm 3.3.2. As detailed in Section 3.3, the use of the global sensitivity matrix in this algorithm explores the entire parameter space, thus providing a better measure of global identifiability.



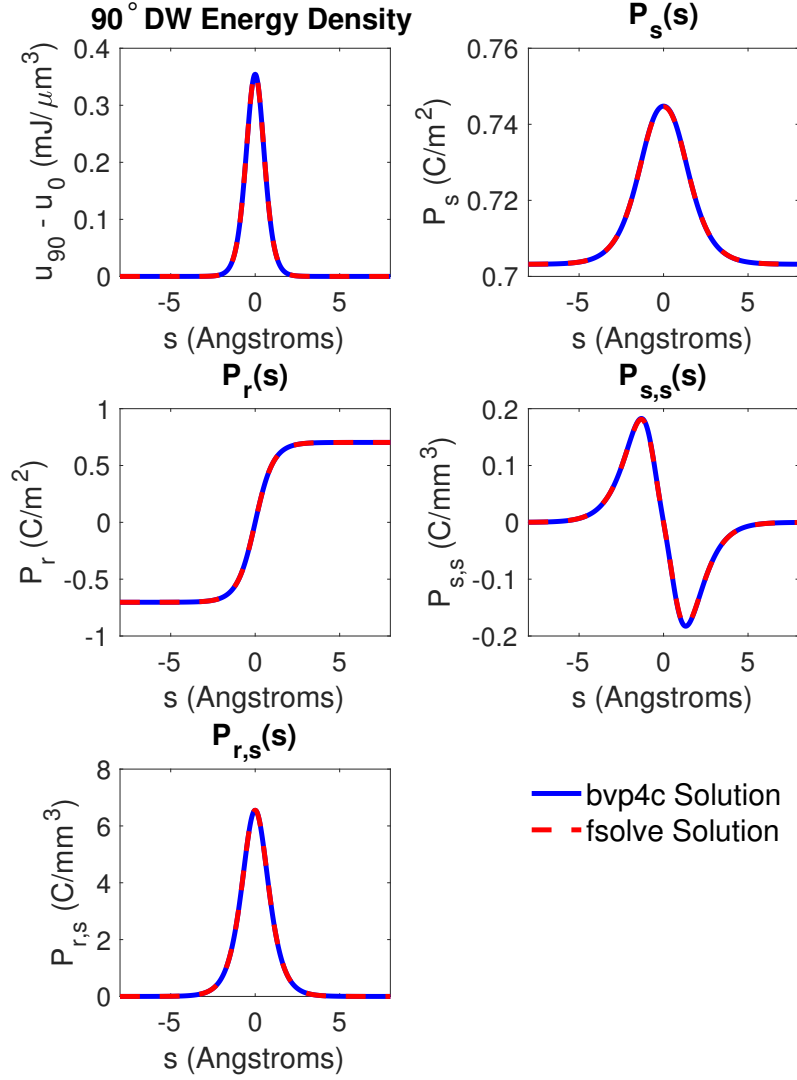


**Figure 7.1** Comparison of finite difference `fsolve.m` and `bvp4c.m` MATLAB solvers for solution of the  $90^\circ$  domain wall energy system. From top left to bottom right,  $90^\circ$  domain wall energy density solution, polarization  $P_s$  in the  $s$  direction, polarization  $P_r$  in the  $s$  direction, and polarization gradients  $P_{s,s}$  and  $P_{r,s}$  in the  $s$  direction as we cross the  $90^\circ$  domain wall.

To construct the global sensitivity matrix, we assume the proposal distribution (5.14). We employ the nominal values and standard distributions from Table 4.2 for the Landau parameters and electrostrictive coefficients. For the gradient exchange parameter  $g_{44}$ , we use the nominal value

**Table 7.2** Results from Algorithm 3.3.2 with the global sensitivity matrix (3.44) to determine noninfluential parameters in  $\theta_{90}$  (7.19) for the  $90^\circ$  domain wall energy  $E_{90^\circ}$  (7.18).

Iteration	$ \lambda_1 $	Eigenvector $\Delta\theta_1$ with corresponding parameters										
		$\alpha_1$	$\alpha_{11}$	$\alpha_{12}$	$\alpha_{111}$	$\alpha_{112}$	$q_{11}$	$q_{12}$	$q_{44}$	$g_{11}$	$g_{12}$	$g_{44}$
1	3.34e-14	4.67e-1	8.95e-2	-9.31e-2	2.68e-1	-3.91e-2	3.22e-1	-1.52e-1	1.66e-1	1.97e-1	-6.99e-1	-9.68e-2
2	4.23e-14	6.16e-2	-8.35e-2	-1.21e-1	5.32e-2	2.45e-2	-2.00e-1	-5.08e-1	-3.00e-1	-1.53	—	7.49
3	6.75e-13	-7.48e-1	2.09e-1	-2.75e-3	-4.15e-1	2.96e-2	5.50e-2	4.57e-1	-6.00e-2	-9.11e-2	—	—
4	1.42e-12	—	-1.78e-1	2.90e-1	-6.25e-2	2.69e-2	-6.56e-3	9.14e-1	-1.44e-2	-1.55e-1	—	—
5	7.10e-12	—	-1.55e-1	-3.26e-1	-3.53e-1	1.79e-1	-2.84e-1	—	-4.46e-1	-6.59e-1	—	—
6	5.57e-11	—	4.90e-1	-5.06e-1	-1.44e-1	4.41e-2	6.93e-1	—	2.59e-2	—	—	—
7	2.83e-9	—	-1.78e-1	2.63e-1	5.05e-1	-4.42e-2	—	—	-8.01e-1	—	—	—
Result: The parameters $\alpha_1, q_{11}, q_{12}, g_{11}, g_{12}$ and $g_{44}$ are not influential based on $\epsilon = 1e-9$ .												

and standard deviation identified from the uncertainty analysis of Section 6.3. In the case of the additional parameters  $g_{11}$  and  $g_{12}$ , we assume normal distributions about the nominal values  $\mu_{g_{11}}$ ,  $\mu_{g_{12}}$  provided in Table 7.1,

$$G_{11} \sim \mathcal{N}(\mu_{g_{11}}, (0.05|\mu_{g_{11}}|)^2), \quad G_{12} \sim \mathcal{N}(\mu_{g_{12}}, (0.05|\mu_{g_{12}}|)^2),$$

for the random variables  $G_{11}$  and  $G_{12}$ .

Employing Algorithm 3.3.2, along with the global sensitivity matrix (3.44), we obtain the results in Table 7.2. Here, we assume a threshold  $\epsilon = 1e-9$ . We observe that the higher-order Landau phenomenological parameters are most influential on the model output, thus highlighting the significance of the polarization on the  $90^\circ$  domain wall energy. The shear electrostrictive coefficient  $q_{44}$  is also significant as evidenced by the results of Table 7.2. This illustrates the importance of the shear electromechanical coupling term in the electrostrictive energy (7.6), with respect to the  $90^\circ$  domain wall transition.

A lower threshold, for example taking  $\epsilon = 1e-12$ , yields  $g_{11}$  to be more influential than  $g_{12}$ , which is the first parameter to be eliminated in the algorithm. Thus, the results indicate that  $g_{12}$  is not influential in the sense that its uncertainty is not reflected in uncertainty in the response. This motivates the uncertainty analysis of parameter  $g_{11}$  in Section 7.3, while fixing the parameter  $g_{12}$  at the nominal value provided in Table 7.1, with respect to the model response (7.18).

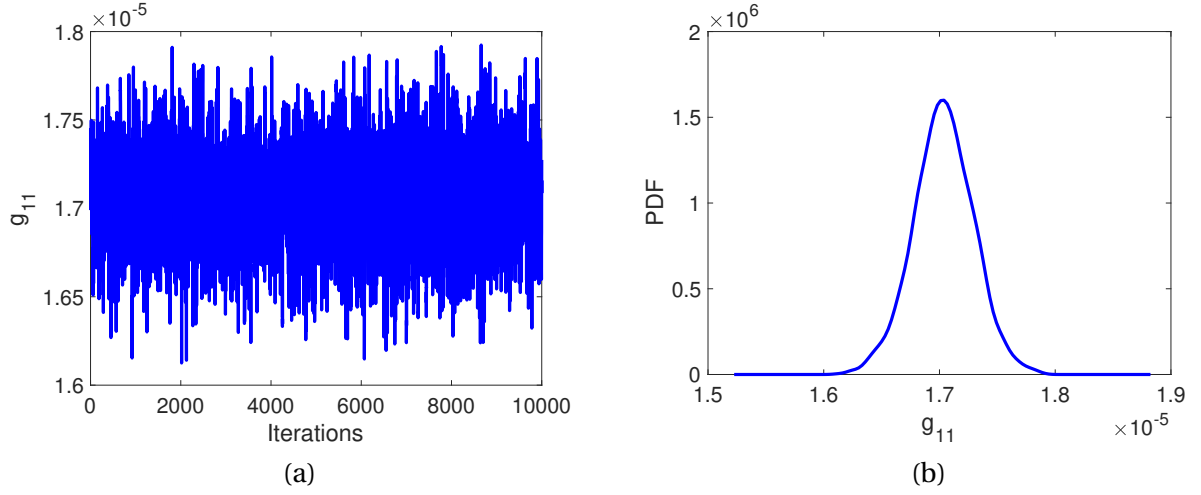


**Figure 7.2** (a) Chain and (b) kernel density estimation for the parameter  $g_{11}$ , obtained from the implementation of the DRAM algorithm [18].

### 7.3 Bayesian Inference

The results of Section 7.2 indicated that the parameter  $g_{11}$  was the most influential gradient exchange parameter with respect to the model response (7.18). Thus we quantify the uncertainty in this parameter while fixing all other parameters in  $\theta_{90}$  at nominal values from Table 7.1.

We employ the delayed rejection adaptive metropolis (DRAM) algorithm introduced in Section 3.4, for the Bayesian uncertainty analysis. Recall that the synthetic observations for the total  $90^\circ$  domain wall energy are obtained by employing the relation

$$E_{90^\circ}^{data}(i) = E_{90^\circ}^* + \varepsilon_i, \quad i = 1, \dots, N,$$

where  $E_{90^\circ}^*$  is the reported total domain wall energy literature value from [56]. Here,  $\varepsilon_i$  denotes random noise  $\varepsilon_i \sim \mathcal{N}(0, \sigma^2)$  where  $\sigma = 0.05 E_{90^\circ}^*$ . We let  $N = 50$ , specifying the number of observations in the synthetic data simulation.

Using a uniform prior distribution for  $g_{11}$ , along with 10,000 accepted value iterations of the algorithm, we obtain the posterior chain and density presented in Figure 7.2. These results yield the mean value for  $g_{11}$  to be  $\mu_{g_{11}} = 1.71 \text{e-}5 \text{ mV} \cdot \text{mm}^3 / \mu\text{C}$ , while the standard deviation is  $\sigma_{g_{11}} = 2.60 \text{e-}7 \text{ mV} \cdot \text{mm}^3 / \mu\text{C}$ . We use the nominal value and standard deviation to construct a normal density for  $g_{11}$ , to be used in the active subspace analysis of Section 7.4.

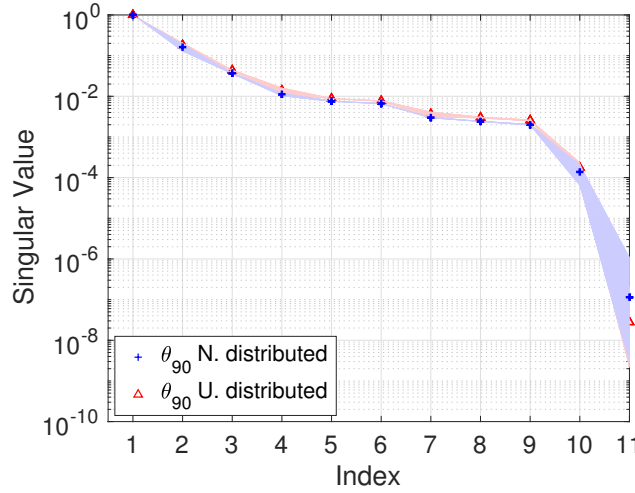


**Figure 7.3** Singular values obtained from the active subspace determination for  $E_{90^\circ}$  assuming normal (3.49) and uniform (3.47) distributions for parameters  $\theta_{90}$ . The shaded area around the singular values corresponds to two standard deviations.

## 7.4 Active Subspace Construction

In this section, we discuss the active subspace analysis for the model  $E_{90^\circ}$ . We first construct the active subspace, employing the methodology introduced in Section 3.4.2. Using several verification techniques, we assess the dimension of the active subspace, and determine active variables, from which we then determine activity scores. We compare the results of the activity scores with the parameter identifiability rankings of Section 7.2, to determine a set of parameters denoting the most sensitive inputs to the model  $E_{90^\circ}(\theta_{90})$ .

To determine the active subspace, we start by employing Algorithm 3.4.1, to construct the gradient matrix  $\mathbf{G}$  (3.58). We use a total of  $M = 10,000$  iterations of the algorithm, assuming uniform and normal distributions of the type (3.47) and (3.49). Upon the construction of the gradient matrix, we take a singular value decomposition  $\mathbf{G} = \mathbf{W}\Sigma\mathbf{V}^T$ , as detailed in Section 3.4.2. This yields the singular values presented in Figure 7.3. It is difficult to identify the active subspace dimension based on the gap-based criteria, as observed from the singular value spectrum. As a result, we proceed with the other dimension selection methods, detailed in Section 3.4.3, to determine the active subspace dimension.

As stated in Section 3.4, active subspaces are often low-dimensional in the sense that the output varies most dominantly in one or two directions in the parameter space. With this in mind, we construct response surfaces considering one-, two-, three- and four-dimensional active subspaces. We plot the one- and two-dimensional response surfaces in Figure 7.4, and present mean relative

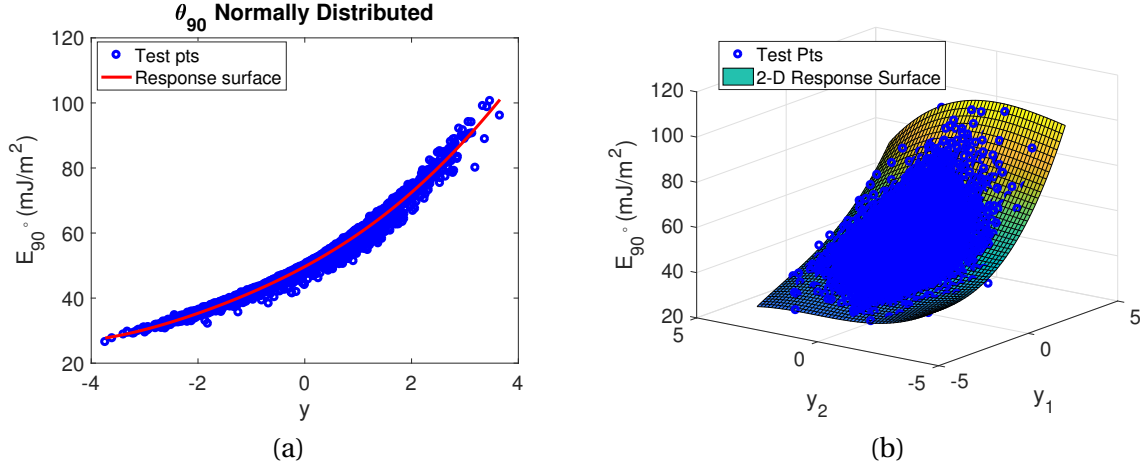


**Figure 7.4** Response surface for  $E_{90^\circ}$  constructed based on a (a) one-dimensional and (b) two-dimensional active subspace.

**Table 7.3** Mean relative errors (MRE) for response surfaces considering 1-, 2-, 3-, and 4-dimensional active subspaces for the model response  $E_{90^\circ}$ .

Dimension	1	2	3	4
MRE	0.0104	0.0075	0.0061	0.0061

errors for all in Table 7.3. As detailed in Section 3.4.3, the dimension of the active subspace is determined when the mean relative errors stop decreasing by more than one order of magnitude. Thus, this criteria indicates a one-dimensional active subspace for the 90° domain wall energy (7.18).

Next, we consider dimension selection based on principal component analysis (PCA). The employment of Algorithm 3.4.3, along with the tolerance  $t^* = 0.95$ , yields a one-dimensional active subspace, consistent with the results of the response surface analysis.

## Activity Scores

In the computation of activity scores to rank the relative parameter influence, we consider one- and two-dimensional active subspace for comparison. Recall that the computation of the activity scores follows the methodology detailed in Section 3.4.4. This yields the activity scores presented in Figure 7.5.

The parameters  $\alpha_1, \alpha_{11}, \alpha_{12}, \alpha_{111}, \alpha_{112}, q_{11}, q_{12}$  and  $g_{11}$  are the most sensitive parameters based on the activity scores. The results indicating the higher-order Landau parameters to be significant are in agreement with the parameter subset selection analysis of Section 6.2. However, here we notice

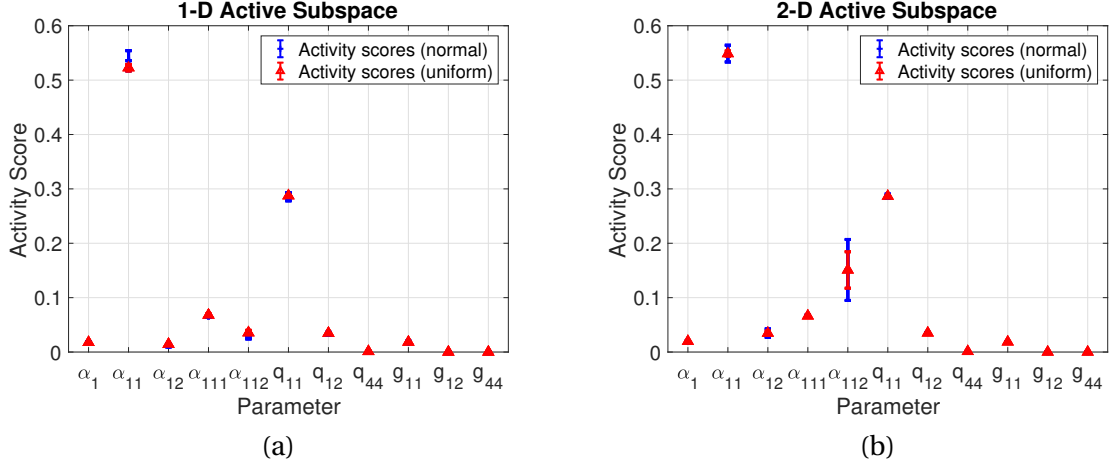


**Figure 7.5** Activity scores for the model response  $E_{90^\circ}$  assuming normal (3.49) and uniform (3.47) parameter distributions, and a (a) one-dimensional and (b) two-dimensional active subspace. The errorbars indicate two standard deviations from the mean.

more significant influence with respect to the electrostrictive coefficients  $q_{11}$  and  $q_{12}$ . We point out, however, that the construction of the activity scores considers the total energy  $E_{90^\circ}$  associated with the  $90^\circ$  domain wall, whereas the vector-valued energy density  $u_{90}(s) - u_0$ , presented in Figure 7.1, was considered in the analysis of Section 7.2. Compared with the energy density, the contributions of the electrostrictive coefficients  $q_{11}$  and  $q_{12}$  is thus more apparent in the model response  $E_{90^\circ}$ . To incorporate the results of both the parameter subset selection analysis results of Section 6.2 and the activity scores given here, we conclude that all electrostrictive coefficients are significant, and we use their respective uncertainties in the uncertainty propagation analysis of Section 7.5.

## 7.5 Uncertainty Propagation

We conclude that the parameters  $\alpha_1, \alpha_{11}, \alpha_{12}, \alpha_{111}, \alpha_{112}, q_{11}, q_{12}, q_{44}$  and  $g_{11}$  are the most sensitive parameters, from the results of the parameter subset selection in Section 7.2 and the activity scores in Section 7.4. Thus, we denote

$$\theta_{90}^{sens} = [\alpha_1, \alpha_{11}, \alpha_{12}, \alpha_{111}, \alpha_{112}, q_{11}, q_{12}, q_{44}, g_{11}]$$

as the most sensitive parameters of in the  $90^\circ$  domain wall energy model  $E_{90^\circ}(\theta_{90})$  (7.18). Throughout this section we randomly sample the sensitive parameters  $\theta_{90}^{sens}$  to propagate their uncertainty on the energy density  $u_{90} - u_0$  while holding all other parameters fixed, and compare with uncertainty propagation when sampling all parameters  $\theta_{90}$ .

To verify that the parameter selection results are independent of possible strong correlation among parameters, we consider two cases for uncertainty propagation. In the first case, we consider the parameter distribution  $\Theta_{90} \sim \mathcal{N}(\mu_{90}, \mathbf{V}_{90})$ , where  $\mu_{90}$  denotes the nominal values given in Table 7.1, and  $\mathbf{V}_{90}$  denotes the diagonal covariance matrix with the squared standard deviations from Table 4.2 in Section 4.1 and the uncertainty analysis in Sections 6.3 and 7.3. We do this with the exception of  $\alpha_{12}$ ,  $\alpha_{111}$  and  $\alpha_{112}$ , for which we take 1/3 of the standard deviations in Table 4.2. Higher standard deviation values for these parameters cause large variations in the solution to the system (7.16)-(7.17), further supporting the parameters' influence. For the parameter  $g_{12}$ , we assume a squared standard deviation  $\sigma_{g_{12}} = 0.05|\mu_{g_{12}}|$ . In the second scenario, we sample the Landau energy parameters strictly from the chains and densities presented in Figures 4.4 and 4.6. This incorporates the correlation among these parameters with respect to the monodomain continuum model analysis of Section 4.3.

For both sampling scenarios, we compare the propagation of sensitive parameters  $\theta_{90}^{sens}$  with the propagation of all parameters  $\theta_{90}$  on the domain wall energy density  $u_{90}(s) - u_0$ . We consider 50%, 90%, 95% and 99% credible intervals when propagating the parameter uncertainties. In Figure 7.6, we plot the mean response along with the credible intervals. In (a) and (b), we consider the parameters to be normally distributed, whereas in (c) and (d), we consider the Landau and electrostrictive parameters sampled from the monodomain chains in Figure 4.4. In the construction of the credible intervals, we used a total of 500 random samples of  $\theta_{90}$  and  $\theta_{90}^{sens}$ . The credible intervals are almost identical, from a qualitative point of view. In addition, the results indicate that sensitive parameters are independent of the choice of distribution.

Next, we subtract the Figure 7.6 “peak values” (at  $s = 0$ ) of the 99% credible intervals associated with the sensitive parameter uncertainty propagation, from the peak values associated with the full parameter uncertainty propagation. This yields the residuals plotted in Figure 7.7, with 20 different simulations of the 99% credible interval construction. Here, we observe the residuals to be small and scattered around zero.

We additionally plot the histogram and kernel density estimation (KDE) of the distributions for  $u_{90}(0) - u_0$ , with respect to the two parameter sampling scenarios detailed earlier, in Figure 7.8. Consistent with the observations of the credible intervals in Figure 7.6, the peak distributions are also almost identical. To quantitatively measure the difference in distributions we use energy statistics.

## Energy Statistics

Energy statistics provide metrics to measure distances between densities, as detailed in Section 3.6. We use them to test the null hypothesis  $H_0 : F_{90} = F_{90}^{sens}$  that the density obtained by propagating all parameters  $\theta_{90}$  is equal to the density obtained by propagating only the sensitive parameters  $\theta_{90}^{sens}$ , while keeping all other parameters fixed.

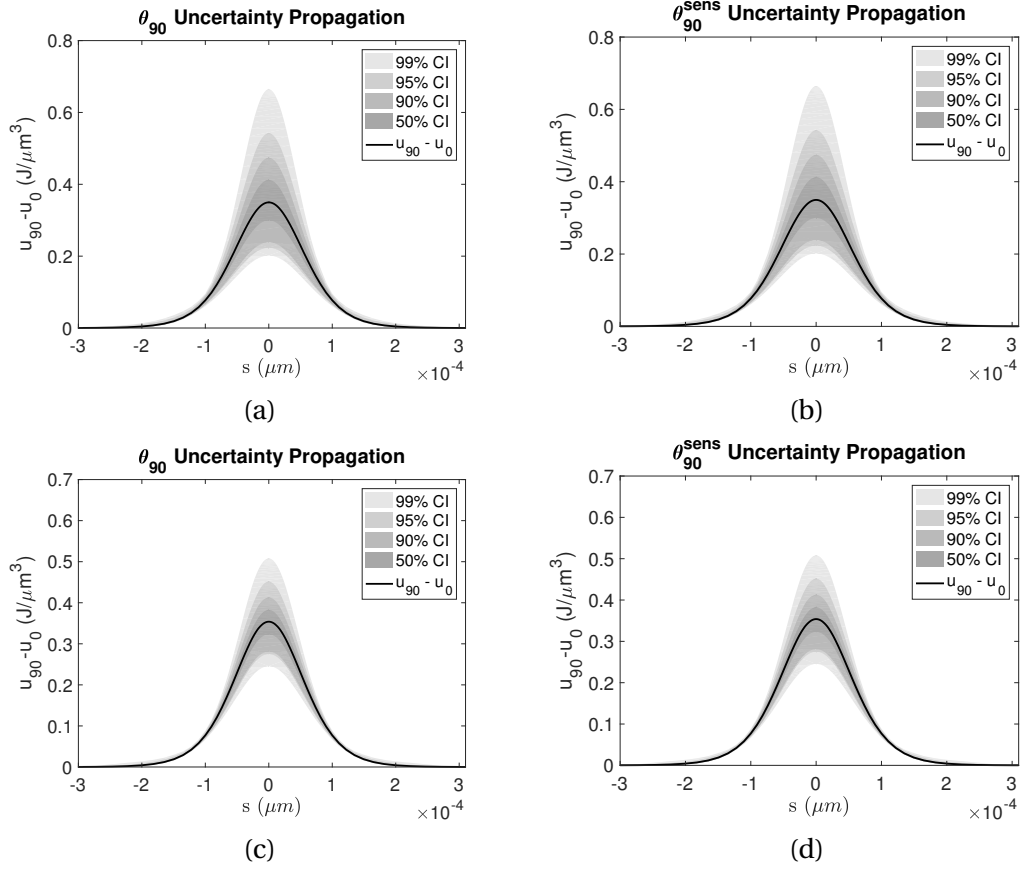


**Figure 7.6** Uncertainty propagation of the (a)  $\theta_{90}$  model inputs and (b)  $\theta_{90}^{sens}$  influential inputs on the energy density  $u_{90}(s) - u_0$ , assuming a normal distribution for the parameters. In (c) and (d) we sample directly from the monodomain chains in [33] for the Landau and electrostrictive parameters.

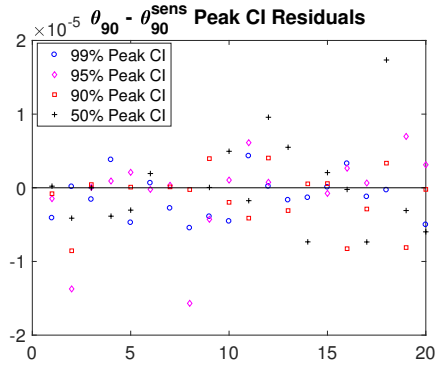


**Figure 7.7** Peak residuals obtained for the different credible intervals (CI) peaks of Figure 7.6.



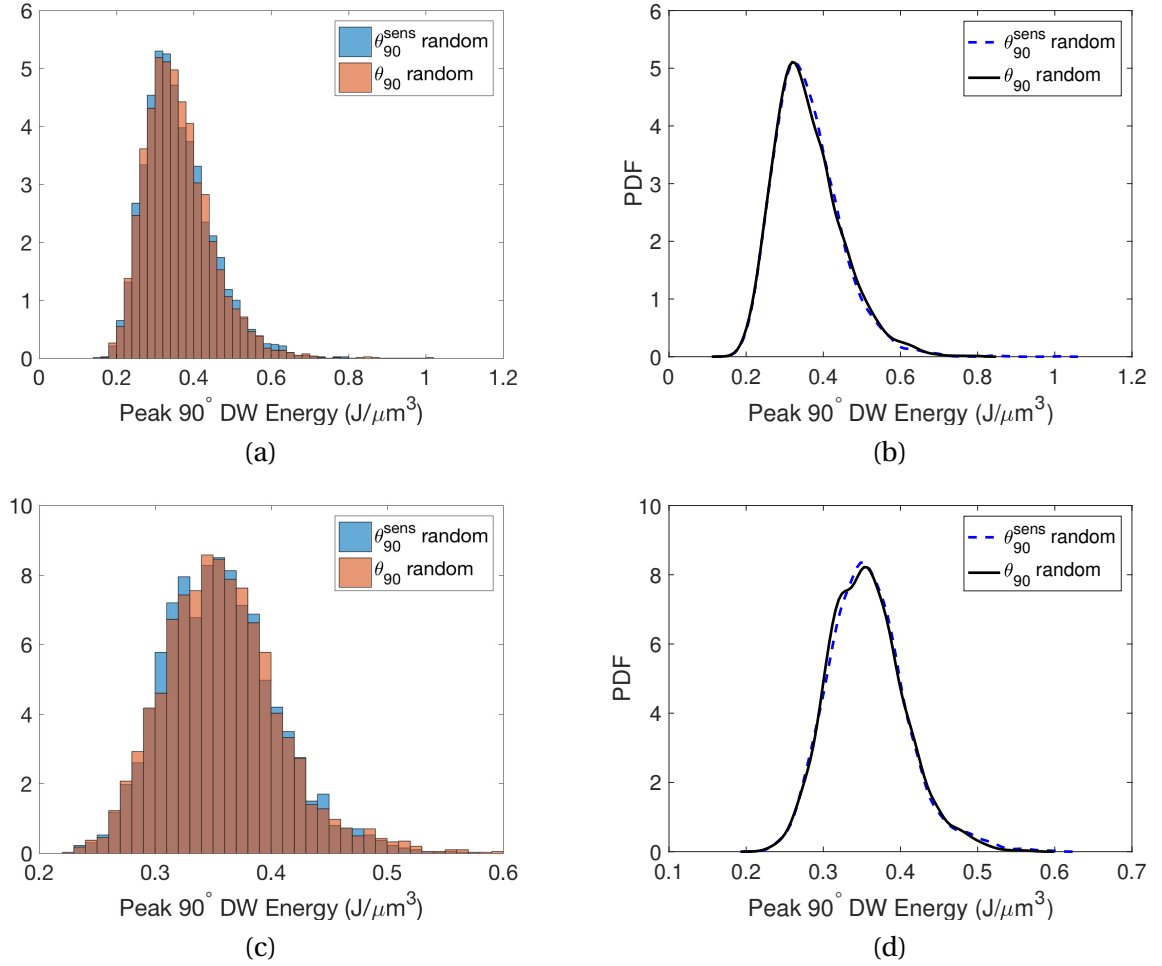


**Figure 7.8** (a) Histogram and (b) probability density of the 90° domain wall energy  $u_{90}(0) - u_0$  distributions with respect to the case where the uncertainties of all parameters  $\theta_{90}$  are propagated against the case where only the uncertainties of parameters  $\theta_{90}^{sens}$  are propagated. In (c) and (d) we sampled directly from the chains obtained in the monodomain analysis reproduced in Chapter 4 and obtained from [33].

The implementation of the energy statistics methodology yields an energy test statistic  $T_{n_1, n_2} = 8.0287\text{e-}4$ , with  $M = 499$  and  $n_1 = n_2 = 4,000$ . In Figure 7.9, we plot the energy statistic replicates, constructed in the manner detailed in Section 3.6. In Table 7.4, we present energy statistic values, corresponding to the confidence levels  $\alpha = 0.05, 0.10$ . The test statistic is clearly lower than the critical values dictated by the confidence levels as observed from Figure 7.9 and Table 7.4. Consequently, we reject the alternate hypothesis that the distributions are not equal.

The energy statistics analysis verifies that the parameters  $\theta_{90}^{sens}$  are the most influential in the domain wall energy model  $E_{90^\circ}(\theta_{90})$  (7.18). For future model calibration, uncertainty propagation

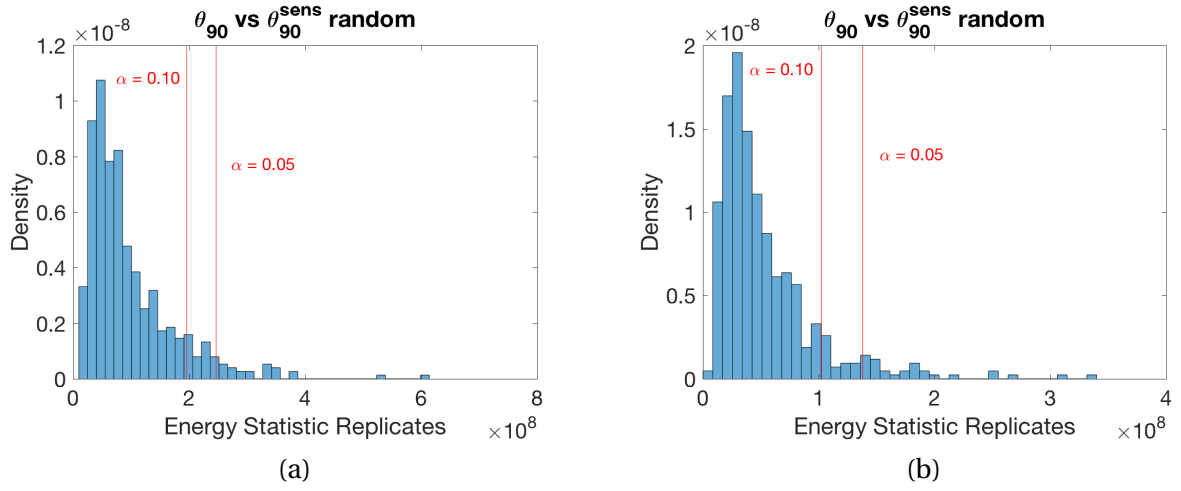


**Figure 7.9** Energy test statistic replicates for the statistical analysis of the  $u_{90}(0) - u_0$  distribution, with  $\theta_{90}$  (a) normally distributed and (b) having Landau energy and electrostrictive parameters sampled from the monodomain chains in [33].

**Table 7.4** Energy test statistic and critical values for  $\alpha = 0.05$ ,  $\alpha = 0.10$ , when sampling the Landau and electrostrictive parameters from a normal distribution (normal) and directly from the monodomain chains (MD) [33].

Density Peak Samples (normal)	Test Statistic	Critical Value ( $\alpha = 0.05$ )	Critical Value ( $\alpha = 0.10$ )
$\theta_{90}$ versus $\theta_{90}^{sens}$ sampled	8.0287e+4	2.4671e+5	1.9612e+5
Density Peak Samples (MD)	Test Statistic	Critical Value ( $\alpha = 0.05$ )	Critical Value ( $\alpha = 0.10$ )
$\theta_{90}$ versus $\theta_{90}^{sens}$ sampled	4.1372e+4	1.4823e+5	1.0102e+5

and model-based control design, we can thus fix the insensitive parameters, whose perturbations will not significantly change model output.

## CHAPTER

# 8

## CONCLUSIONS

The objective of this dissertation was to investigate parameter subset selection techniques and uncertainty quantification of parameters in quantum-informed continuum models for single- and multi-domain ferroelectric materials. Broadly speaking, parameters are considered to be non-influential if the model responses minimally reflect perturbations in the inputs' admissible parameter space. One can typically fix non-influential parameters at nominal values in processes such as Bayesian model calibration, uncertainty propagation, and model-based control design.

Phenomenological models describing domain structure evolution, based on Landau-Ginzburg theory, are sometimes criticized because of the estimates that must be made about the governing unknown parameters [32]. First-principles computational investigations, such as density functional theory (DFT) simulations, are often preferred in determining ferroelectric material evolution properties, due to their accuracy [32, 37]. However, these calculations are not feasible for large-scale computations required in material design [33].

In this investigation, we used parameter subset selection techniques and Bayesian uncertainty analysis methods to determine the relative importance of parameters in models, informed by high-fidelity DFT calculations. We identified which parameters are influential, and isolated the non-influential ones that may be fixed in future model-based material design and model calibration studies.

For single domain ferroelectric material structures, we employed global sensitivity analysis techniques to quantify the relative influence of 5 phenomenological parameters in a 2-D sixth-order

Landau energy, as well as 7 parameters in a electrostrictive energy. The results were verified by comparing with Bayesian inference results and Fisher information-based subset selection criteria. For multi-domain ferroelectric material structures, we employed Fisher information-based parameter subset selection and active subspace analysis to quantify the relative influence of 5 Landau energy phenomenological parameters, 3 electrostrictive energy parameters, and 3 gradient energy parameters in Landau-Ginzburg theory-based continuum model.

In the absence of *a priori* knowledge about parameter distributions, when performing global sensitivity analysis, parameters are typically assumed to be independent and uniformly distributed. Using a general variance-based methodology for correlated parameters, we demonstrate how the incorrect assumption of mutually independent parameters may lead to incorrect interpretations about parameter influence on model outputs. These results are further exemplified by Bayesian inference results provided in Chapter 4 and [33], regarding parameters in the single domain ferroelectric structure analysis. The Fisher information matrix-based parameter subset selection corroborates these conclusions, by employing information stemmed from the local sensitivity matrix. This analysis, furthermore enables the comparison of individual, partial and total effects due to parameter correlation structures, and is consistent with expected results from subsequent Bayesian model calibration. Broadly, the results of the single domain ferroelectric structure analysis indicate a significant contribution from higher-order Landau polarization energy terms, due to strong parameter correlation.

The multi-domain ferroelectric material models consider polarization and strain interactions across  $180^\circ$  and  $90^\circ$  domain walls. This includes polarization gradient energy relations, which model the domain wall transitions in addition to the elastic energy, Landau polarization energy, and electrostrictive energy considered in the single domain continuum model analysis. The implementation of the models requires numerical solutions to boundary value problems composed of sets of differential equations. This increases the computational expense, otherwise required in variance-based global sensitivity analysis. Thus, we employed gradient-based parameter subset selection and active subspace analysis techniques to rank the relative influence of Landau energy, electrostrictive energy and gradient exchange parameters. The results yielded significant importance of higher-order Landau energy parameters, as well as electromechanical coupling coefficients, whereas only one gradient energy parameter was influential in the  $90^\circ$  domain wall energy response. We verified these results by employing uncertainty propagation and measuring distribution distances, using energy statistics. In comparison with the monodomain continuum analysis, we conclude that higher-order Landau energy terms are important for the modeling of micro-scale domain structure evolution of ferroelectric materials.

The incorporation of simultaneous single- and multi domain ferroelectric structure evolution analysis is of significant interest in future work proceedings. This includes data fusion from multiple sources to simultaneously inform parameters based on multiple effects away from and in close

proximity to  $180^\circ$  and  $90^\circ$  domain walls. The complex motion of domain walls and formation of new domains as a result of domain wall interactions motivates a comprehensive investigation involving mono- and polydomain structure evolution. Uncertainty analysis challenges posed by data fusion from several sources may be addressed by the inclusion of maximum entropy approaches, which propose accurate weighting mechanisms, based on the covariance structure between data sets [13]. The investigations in this dissertation have laid the foundations for a complete study in which longitudinal data acquired from several sources, could be used to simultaneously infer Landau-Ginzburg parameters at the polydomain scale, both for lead titanate and other ferroelectric materials.

## BIBLIOGRAPHY

- [1] Bang, Y., Abdel-Khalik, H. S. & Hite, J. M. “Hybrid reduced order modeling applied to nonlinear models”. *International Journal for Numerical Methods in Engineering* **91.9** (2012), pp. 929–949.
- [2] Bilgen, O., De Marqui jr, C., Kochersberger, K. B. & Inman, D. J. “Macro-fiber composite actuators for flow control of a variable camber airfoil”. *Journal of Intelligent Material Systems and Structures* **22.1** (2011), pp. 81–91.
- [3] Brun, R., Kuhni, M., Siegrist, H., Gujer, W. & Reichert, P. “Practical identifiability of asm2d parameters: Systematic selection and tuning of parameter sets”. *Water Research* **36** (2002), pp. 4113–4127.
- [4] Burth, M., Verghese, G. & Velez-Reyes, M. “Subset selection for improved parameter estimation in on-line identification of a synchronous generator”. *IEEE Transactions on Power Systems* **14** (1999), pp. 218–225.
- [5] Cao, W. & Cross, L. “Theory of tetragonal twin structures in ferroelectric perovskites with a first-order phase transition”. *Physical Review B* **44.1** (1991), p. 5.
- [6] Chen, L.-Q. “Phase-field models for microstructure evolution”. *Annual Review of Materials Research* **32.1** (2002), pp. 113–140.
- [7] Chib, S. & Greenberg, E. “Understanding the metropolis-hastings algorithm”. *The American Statistician* **49.4** (1995), pp. 327–335.
- [8] Constantine, P. G. *Active Subspaces: Emerging Ideas for Dimension Reduction in Parameter Studies*. SIAM, Philadelphia, PA, 2015.
- [9] Constantine, P. G. & Diaz, P. “Global sensitivity metrics from active subspaces”. *Reliability Engineering & System Safety* **162** (2017), pp. 1–13.
- [10] Contron-Arias, A., Banks, H. T., Capald, A. & Lloyd, A. L. “A sensitivity matrix based methodology for inverse problem formulation”. *Journal of Inverse and Ill-Posed Problems* **17** (2009), pp. 545–564.
- [11] Falk, F. “Ginzburg-Landau theory of static domain walls in shape-memory alloys”. *Zeitschrift für Physik B Condensed Matter* **51.2** (1983), pp. 177–185.
- [12] Friedman, J., Hastie, T. & Tibshirani, R. *The Elements of Statistical Learning*. Vol. 1. Springer Series in Statistics, New York, NY, 2001.
- [13] Gao, W., Oates, W. S. & Smith, R. C. “A Maximum Entropy Approach for Uncertainty Quantification and Analysis of Multifunctional Materials”. *ASME 2017 Conference on Smart Materials,*

*Adaptive Structures and Intelligent Systems*. American Society of Mechanical Engineers. 2017, V001T08A013–V001T08A013.

- [14] Ginzburg, V. L. “On the theory of superconductivity”. *Il Nuovo Cimento (1955-1965)* **2.6** (1955), pp. 1234–1250.
- [15] Golub, G. & Van Loan, C. *Matrix Computations*. Johns Hopkins Univ Press, Baltimore, MD, 1996.
- [16] Gonze, X., Amadon, B., Anglade, P.-M., Beuken, J.-M., Bottin, F., Boulanger, P., Bruneval, F., Caliste, D., Caracas, R., Côté, M., et al. “ABINIT: First-principles approach to material and nanosystem properties”. *Computer Physics Communications* **180.12** (2009), pp. 2582–2615.
- [17] Gruverman, A., Cross, J. & Oates, W. “Peculiar effect of mechanical stress on polarization stability in micrometer-scale ferroelectric capacitors”. *Applied Physics Letters* **93.24** (2008), p. 242902.
- [18] Haario, H., Laine, M., Mira, A. & Saksman, E. “DRAM: efficient adaptive MCMC”. *Statistics and Computing* **16.4** (2006), pp. 339–354.
- [19] Halko, N., Martinsson, P.-G. & Tropp, J. A. “Finding structure with randomness: Probabilistic algorithms for constructing approximate matrix decompositions”. *SIAM Review* **53.2** (2011), pp. 217–288.
- [20] Hoffman, K. L. & Wood, R. J. “Myriapod-like ambulation of a segmented microrobot”. *Autonomous Robots* **31.1** (2011), p. 103.
- [21] Hong, C.-H., Kim, H.-P., Choi, B.-Y., Han, H.-S., Son, J. S., Ahn, C. W. & Jo, W. “Lead-free piezoceramics—Where to move on?” *Journal of Materiomics* **2.1** (2016), pp. 1–24.
- [22] Jaffe, B., Cook Jr., W. R. & Jaffe, H. *Piezoelectric Ceramics*. Academic Press, New York, NY, 1971.
- [23] Jolliffe, I. *Principal Component Analysis*. Springer, New York, NY, 2002.
- [24] King-Smith, R. & Vanderbilt, D. “First-principles investigation of ferroelectricity in perovskite compounds”. *Physical Review B* **49.9** (1994), p. 5828.
- [25] Koruza, J., Bell, A. J., Frömling, T., Webber, K. G., Wang, K. & Rödel, J. “Requirements for the transfer of lead-free piezoceramics into application”. *Journal of Materiomics* **4.1** (2018), pp. 13–26.
- [26] Kumar, V., Hays, M., Fernandez, E., Oates, W. & Alvi, F. “Flow sensitive actuators for micro-air vehicles”. *Smart Materials and Structures* **20.10** (2011), p. 105033.
- [27] Leon, L., Smith, R. C., Oates, W. S. & Miles, P. “Analysis of a multi-axial quantum-informed ferroelectric continuum model: Part 2-sensitivity analysis”. *Journal of Intelligent Material Systems and Structures* (2018), p. 1045389X18781024.

- [28] Lewis, A., Smith, R. & Williams, B. “Gradient free active subspace construction using Morris screening elementary effects”. *Computers & Mathematics with Applications* **72.6** (2016), pp. 1603–1615.
- [29] Li, G., Rabitz, H., Yelvington, P., Oluwole, O., Bacon, F., Kolb, C. & Schoendorf, J. “Global sensitivity analysis for systems with independent and/or correlated inputs”. *J. Phys. Chem. A* **114** (2010), pp. 6022–6032.
- [30] Malvern, L. E. *Introduction to the Mechanics of a Continuous Medium*. Prentice-Hall, Englewood Cliffs, NJ, 1969.
- [31] McMeeking, R. M. & Landis, C. M. “Electrostatic forces and stored energy for deformable dielectric materials”. *Journal of Applied Mechanics* **72.4** (2005), pp. 581–590.
- [32] Meyer, B & Vanderbilt, D. “Ab initio study of ferroelectric domain walls in PbTiO<sub>3</sub>”. *Physical Review B* **65.10** (2002), p. 104111.
- [33] Miles, P., Leon, L., Smith, R. C. & Oates, W. S. “Analysis of a multi-axial quantum informed ferroelectric continuum model: Part I—Uncertainty quantification”. *Journal of Intelligent Material Systems and Structures* (2017), p. 1045389X18781023.
- [34] Miles, P. R. “Uncertainty Analysis of Multifunctional Constitutive Relations and Adaptive Structures”. PhD thesis. The Florida State University, 2017.
- [35] Morris, M. “Factorial sampling plans for preliminary computational experiments”. *Technometrics* **33.2** (1991), pp. 161–174.
- [36] Murali, P., Ledermann, N., Paborowski, J., Barzegar, A., Gentil, S., Belgacem, B., Petitgrand, S., Bosseboeuf, A. & Setter, N. “Piezoelectric micromachined ultrasonic transducers based on PZT thin films”. *IEEE transactions on ultrasonics, ferroelectrics, and frequency control* **52.12** (2005), pp. 2276–2288.
- [37] Oates, W. “A quantum informed continuum model for ferroelectric materials”. *Smart Materials and Structures* **23.10** (2014), p. 104009.
- [38] Owen, A. “Better estimation of small Sobol’ indices”. *ACM Trans. Model Comput. Simul.* **23.11** (2013).
- [39] Payne, M. C., Teter, M. P., Allan, D. C., Arias, T. & Joannopoulos, a. J. “Iterative minimization techniques for ab initio total-energy calculations: molecular dynamics and conjugate gradients”. *Reviews of Modern Physics* **64.4** (1992), p. 1045.
- [40] Pérez-Arancibia, N. O., Ma, K. Y., Galloway, K. C., Greenberg, J. D. & Wood, R. J. “First controlled vertical flight of a biologically inspired microrobot”. *Bioinspiration & Biomimetics* **6.3** (2011), p. 036009.
- [41] Prenter, P. M. *Splines and Variational Methods*. Dover Publications, Mineola, NY, 2008.



- [42] Quaizer, T. & Monnigmann, M. “Systematic identifiability testing for unambiguous mechanistic modeling application to jak-stat, map kinase, and nf- $\kappa$ b signaling pathway models”. *BMC Systems Biology* **3** (2009).
- [43] Resta, R. “Macroscopic polarization in crystalline dielectrics: the geometric phase approach”. *Reviews of modern physics* **66.3** (1994), p. 899.
- [44] Russi, T. M. “Uncertainty quantification with experimental data and complex system models”. PhD thesis. UC Berkeley, 2010.
- [45] Saltelli, A. “Making best use of model evaluations to compute sensitivity indices”. *Computer Physics Communications* **145** (2002), pp. 280–297.
- [46] Saltelli, A., Annoni, P., Azzini, I., Campolongo, F., Ratto, M. & Tarantola, S. “Variance based sensitivity analysis of model output: design and estimator for the total sensitivity index”. *Computer Physics Communications* **181.2** (2010), pp. 259–270.
- [47] Scott, J. F. *Ferroelectric Memories*. Springer-Verlag, New York, NY, 2000.
- [48] Sholl, D. & Steckel, J. A. *Density Functional Theory: A Practical Introduction*. John Wiley & Sons, Hoboken, NJ, 2011.
- [49] Shu, Y. & Bhattacharya, K. “Domain patterns and macroscopic behaviour of ferroelectric materials”. *Philosophical Magazine B* **81.12** (2001), pp. 2021–2054.
- [50] Smith, R. C. *Smart Material Systems: Model Development*. SIAM, Philadelphia, PA, 2005.
- [51] Smith, R. C. *Uncertainty Quantification: Theory, Implementation and Applications*. SIAM, Philadelphia, PA, 2014.
- [52] Smith, R. C. & Hu, Z. “Homogenized energy model for characterizing polarization and strains in hysteretic ferroelectric materials: Material properties and uniaxial model development”. *Journal of Intelligent Material Systems and Structures* **23.16** (2012), pp. 1833–1867.
- [53] Sobol’, I. “Sensitivity analysis for nonlinear mathematical models”. *Mathematical Modeling & Computational Experiment* **1** (1993), pp. 407–414.
- [54] Sobol, I., Tarantola, S., Gatelli, D., Kucherenko, S. & Mauntz, W. “Estimating the approximation error when fixing unessential factors in global sensitivity analysis”. *Reliability Engineering and System Safety* **92.7** (2007), pp. 957–960.
- [55] Song, H. J., Choi, Y.-T., Wereley, N. M. & Purekar, A. S. “Energy harvesting devices using macro-fiber composite materials”. *Journal of Intelligent Material Systems and Structures* **21.6** (2010), pp. 647–658.
- [56] Stemmer, S., Streiffer, S., Ernst, F. & Rüuhle, M. “Atomistic structure of 90 domain walls in ferroelectric PbTiO<sub>3</sub> thin films”. *Philosophical Magazine A* **71.3** (1995), pp. 713–724.

- [57] Su, Y. & Landis, C. M. “Continuum thermodynamics of ferroelectric domain evolution: Theory, finite element implementation, and application to domain wall pinning”. *Journal of the Mechanics and Physics of Solids* **55.2** (2007), pp. 280–305.
- [58] Székely, G. J. & Rizzo, M. L. “Energy statistics: A class of statistics based on distances”. *Journal of Statistical Planning and Inference* **143.8** (2013), pp. 1249–1272.
- [59] Tagantsev, A. K., Cross, L. E. & Fousek, J. *Domains in Ferroic Crystals and Thin Films*. Springer, New York, NY, 2010.
- [60] Weirs, V., Kamm, J., Swiler, L. P., Tarantola, S., Ratto, S., Adams, B., Rider, W. & Eldred, M. “Sensitivity analysis techniques applied to a system of hyperbolic conservation laws”. *Reliability Engineering and System Safety* (2010), pp. 7765–7767.
- [61] Wentworth, M, Smith, R. & Banks, H. “Parameter selection and verification techniques based on global sensitivity analysis illustrated for an HIV model”. *SIAM/ASA Journal on Uncertainty Quantification* **4** (2016), pp. 266–297.
- [62] Wood, R. J. “The first takeoff of a biologically inspired at-scale robotic insect”. *IEEE Transactions on Robotics* **24.2** (2008), pp. 341–347.
- [63] Wood, R. J., Finio, B., Karpelson, M., Ma, K., Pérez-Arancibia, N. O., Sreetharan, P. S., Tanaka, H. & Whitney, J. P. “Progress on ‘pico’ air vehicles”. *The International Journal of Robotics Research* **31.11** (2012), pp. 1292–1302.
- [64] Yang, W. & Ayers, P. W. “Density-functional theory”. *Computational Medicinal Chemistry for Drug Discovery*. CRC Press, 2003, pp. 103–132.
- [65] Zhang, W & Bhattacharya, K. “A computational model of ferroelectric domains. Part I: model formulation and domain switching”. *Acta Materialia* **53.1** (2005), pp. 185–198.
- [66] Ziegler, T. “Approximate density functional theory as a practical tool in molecular energetics and dynamics”. *Chemical Reviews* **91.5** (1991), pp. 651–667.

## **APPENDIX**

APPENDIX

A

DELAYED REJECTION ADAPTIVE  
METROPOLIS ALGORITHM

---

**Algorithm A.0.1:** Delayed Rejection Adaptive Metropolis Algorithm (DRAM) using a Normal Likelihood Function [18, 51].

---

- (1) Preset design parameters  $n_s, \sigma_s^2, s_p$  and  $k_0$ , as well as the number of chain iterations  $M$ . Recall that  $n_s$  and  $\sigma_s^2$  are related to the error variance update, whereas  $s_p$  is derived based on the parameter dimension  $p$  and is in practice taken to be  $2.38^2/p$ .
  - (2) Compute  $\theta^0 = \arg \min_{\theta} \sum_{i=1}^N [m_i^{obs} - f_i(\theta)]^2$ .
  - (3) Substitute  $\theta^0$  and set  $SS_{\theta^0} = \sum_{i=1}^N [m_i^{obs} - f_i(\theta^0)]^2$ .
  - (4) Determine initial variance estimate  $s_0^2 = \frac{SS_{\theta^0}}{N-p}$ , where  $p$  is the number of parameters.
  - (5) Construct initial covariance estimate  $V_0 = s_0^2 [\mathbf{S}^T(\theta^0) \mathbf{S}(\theta^0)]^{-1}$ , set  $R = \text{chol}(V)$ . Recall that the sensitivity matrix  $\mathbf{S}$  is defined in (3.44).
  - (5) For  $k = 1, \dots, M$ 
    - a. Sample  $z_k \sim \mathcal{N}(0, I)$ .
    - b. Construct candidate  $\theta^* = \theta^{k-1} + Rz_k$  (i.e.,  $\theta^* \sim \mathcal{N}(\theta^{k-1}, V_{k-1})$ ).
    - c. Sample  $u_{\alpha} \sim \mathcal{U}(0, 1)$ .
    - d. Compute  $SS_{\theta^*} = \sum_{i=1}^N [m_i^{obs} - f_i(\theta^*)]^2$ .
    - e. Compute  $\alpha(\theta^* | \theta^{k-1}) = \min\left(1, e^{-[SS_{\theta^*} - SS_{\theta^{k-1}}]/2s_{k-1}^2}\right)$ .
    - f. If  $u_{\alpha} < \alpha$ ,  
Set  $\theta^k = \theta^*$ ,  $SS_{\theta^k} = SS_{\theta^*}$   
else  
Enter Delayed Rejection Algorithm A.0.2.  
endif
    - g. Update  $s_k^2 \sim \text{Inv-gamma}(a_{val}, b_{val})$ , where  
 $a_{val} = 0.5(n_s + n)$ ,  $b_{val} = 0.5(n_s \sigma_s^2 + SS_{\theta^k})$ .
    - h. if  $\text{mod}(k, k_0) = 1$   
Update  $V_k = s_p \text{cov}(\theta^0, \theta^1, \theta^2, \dots, \theta^k)$ ,  $R_k = \text{chol}(V_k)$ .  
else  
 $V_k = V_{k-1}$ .  
endif
-

---

**Algorithm A.0.2:** Delayed Rejection Component of DRAM using a Normal Likelihood Function [18, 51].

---

(1) Preset the design parameter  $\gamma_2 = 1$ . We use  $\gamma_2 = 1/5$ .

(2) Sample  $z_{k_2} \sim \mathcal{N}(0, I)$ .

(3) Construct second-stage candidate

$$\theta^{*2} = \theta^{k-1} + \gamma_2 R_{k-1}^T z_{k_2}, \quad (\text{i.e., } \theta^{*2} \sim \mathcal{N}(\theta^{k-1}, \gamma_2^2 V_{k-1})).$$

(4) Sample  $u_{\alpha_2} \sim \mathcal{U}(0, 1)$ .

(5) Compute  $SS_{\theta^{*2}} = \sum_{i=1}^N [m_i^{obs} - f_i(\theta^{*2})]^2$ .

(6) Compute

$$\alpha_2(\theta^{*2} | \theta^{k-1}, \theta^*) = \min \left( 1, \frac{\pi(\theta^{*2} | m^{obs}) J(\theta^* | \theta^{*2}) [1 - \alpha(\theta^* | \theta^{*2})]}{\pi(\theta^{k-1} | m^{obs}) J(\theta^* | \theta^{k-1}) [1 - \alpha(\theta^* | \theta^{k-1})]} \right),$$

where  $J$  is the proposal distribution in 6b. of Algorithm A.0.1. In general,

$$J(\theta^i | \theta^j) = \frac{1}{\sqrt{(2\pi)^p |V|}} \exp \left( -\frac{1}{2} [(\theta^i - \theta^j) V^{-1} (\theta^i - \theta^j)^T] \right).$$

(7) If  $u_{\alpha_2} < \alpha_2$ ,

Set  $\theta^k = \theta^{*2}$ ,  $SS_{\theta^k} = SS_{\theta^{*2}}$ .

else

Set  $\theta^k = \theta^{k-1}$ ,  $SS_{\theta^k} = SS_{\theta^{k-1}}$ .

endif

---